

# 可扩展离子阱系统中的高保真度量 子计算

(申请清华大学理学博士学位论文)

培 养 单 位： 交叉信息研究院

学 科： 物理

研 究 生： 张 帅 宁

指 导 教 师： 金 奇 奂 教 授

二〇二〇年五月



# **High Fidelity Quantum Computing in Scalable Trapped Ion System**

Dissertation Submitted to

**Tsinghua University**

in partial fulfillment of the requirement

for the degree of

**Doctor of Philosophy**

in

**Physics**

by

**Zhang Shuaining**

Dissertation Supervisor: Professor Kihwan Kim

**May, 2020**



# 关于学位论文使用授权的说明

本人完全了解清华大学有关保留、使用学位论文的规定，即：

清华大学拥有在著作权法规定范围内学位论文的使用权，其中包括：(1) 已获学位的研究生必须按学校规定提交学位论文，学校可以采用影印、缩印或其他复制手段保存研究生上交的学位论文；(2) 为教学和科研目的，学校可以将公开的学位论文作为资料在图书馆、资料室等场所供校内师生阅读，或在校园网上供校内师生浏览部分内容；(3) 根据《中华人民共和国学位条例暂行实施办法》，向国家图书馆报送可以公开的学位论文。

本人保证遵守上述规定。

(保密的论文在解密后应遵守此规定)

作者签名：\_\_\_\_\_

导师签名：\_\_\_\_\_

日 期：\_\_\_\_\_

日 期：\_\_\_\_\_

## 摘要

离子阱系统作为量子计算机的有希望和领先的候选者，最近在量子计算和量子模拟中显示出强大的能力。在本文中，我们展示了一个可扩展和独立控制多达五个离子的捕获离子系统作为一个简单通用的量子模拟器。为了测试其功能和稳定性，我们提出并实施了一种可扩展的方案，通过调制激光场耦合到多个运动模式来实现多个  $^{171}\text{Yb}^+$  离子量子比特的全局纠缠门。为了证明这些全局门的有效性和灵活性，我们使用单个全局操作生成了四个量子比特的 Greenberger-Horne-Zeilinger 态。制备好的 GHZ 态的保真度会受到系统缺陷的限制。随后，我分析了系统误差模型并实现了概率误差消除方法以改善期望值的估计。我将该方法应用于每个不完美的基本量子运算，并确定了误差减轻的量子计算的性能。我观察到单比特和两比特门的有效门保真度比物理门的保真度分别提高了两个和一个数量级。

**关键词：**离子阱，量子计算，全局量子门，量子误差减轻

## Abstract

The trapped ion systems, as a promising and leading candidate for quantum computers, have shown powerful capabilities in quantum computation and quantum simulation recently. In this thesis, we present the construction of a scalable trapped-ion system with full controllability for up to five ions as a small and general quantum simulator. In order to test its capability and stability, we propose and implement a scalable scheme to realize the global entangling gates on multiple  $^{171}\text{Yb}^+$  ion-qubits by coupling the laser field to multiple motional modes. To prove the power and flexibility of the global entangling gate, we use a single global operation to generate a Greenberger–Horne–Zeilinger state with up to four qubits. The state fidelities of the prepared GHZ states are limited by system imperfection. Then, I analyze the system error-model and implement the probabilistic error-cancellation method to improve the estimation of expectation value. I apply the method to every imperfect elementary quantum-operation and benchmark the performance of error-mitigated quantum-computation. I observe significant improvements on effective gate fidelities of single- and two-qubit gates by two and one orders of magnitude to those of physical gates, respectively.

**Key Words:** Trapped ion; Quantum Computation; Global Quantum Gate; Quantum Error Mitigation

## Contents

Chapter 1 Introduction .....	1
1.1 Quantum computing with high fidelity .....	1
1.2 Quantum error mitigation .....	2
1.3 Thesis structure .....	4
Chapter 2 Trapped $^{171}\text{Yb}^+$ ion system .....	5
2.1 The Paul trap .....	5
2.1.1 Principle of trapping ions .....	5
2.1.2 Blade trap .....	6
2.1.3 Bifilar helical resonator .....	9
2.2 $^{171}\text{Yb}^+$ ion .....	10
2.2.1 Energy structure .....	10
2.2.2 Ionization of $^{171}\text{Yb}$ atom .....	11
2.2.3 Doppler cooling and repumping .....	12
2.2.4 Detection .....	13
Chapter 3 Quantum manipulation .....	15
3.1 Laser-ion interaction .....	15
3.2 Microwave operations .....	16
3.3 Raman laser operations .....	17
3.3.1 Carrier, blue sideband and red sideband transitions.....	17
3.3.2 Spin-dependent force .....	18
3.3.3 Mølmer-Sørensen gate .....	19
3.4 State initialization.....	25
3.4.1 Optical pumping .....	25
3.4.2 Sideband cooling .....	25
Chapter 4 Blade ion trap system setup.....	27
4.1 System design through fiber connection.....	27
4.2 Blade trap assembling .....	28
4.2.1 Electrode connection .....	28
4.2.2 3D structure assembling.....	30
4.2.3 Vacuum system .....	32



4.3	Photonic crystal fiber cable.....	34
4.3.1	Hydrogen loading.....	34
4.3.2	Connectorization.....	34
4.3.3	Curing.....	35
4.4	Individual addressing system.....	37
4.4.1	EOD approach.....	38
4.4.2	Multi-channel AOM approach.....	41
<b>Chapter 5 Global quantum entanglement.....</b>		<b>47</b>
5.1	Overview of global gate.....	47
5.2	Single-mode approach.....	48
5.2.1	Scheme.....	48
5.2.2	Three-qubit GHZ state test.....	50
5.3	Multi-mode approach.....	53
5.3.1	Scheme.....	53
5.3.2	Three- and four-qubit GHZ state results.....	54
5.4	Discussion.....	58
<b>Chapter 6 Quantum error mitigation.....</b>		<b>61</b>
6.1	Paradigm of error-mitigated quantum computation.....	61
6.2	Experimental realization.....	63
6.3	Characterization of noisy quantum gates.....	64
6.3.1	PTM representation.....	64
6.3.2	Maximum-likelihood gate set tomography.....	65
6.3.3	PTMs for single- and two-qubit gate set.....	66
6.4	Decomposition of noise operations.....	71
6.5	Benchmarking of the quantum error mitigation protocol.....	73
6.5.1	Single-qubit gate randomized benchmarking.....	73
6.5.2	Two-qubit gate randomized benchmarking.....	75
6.6	Analysis on residual errors.....	76
6.7	Discussion.....	78
<b>Chapter 7 Error-mitigated Hubbard model simulation.....</b>		<b>80</b>
7.1	Overview of Hubbard model.....	80
7.2	Simulation of two fermionic modes.....	81
7.3	Simulation of three fermionic modes.....	83

## Contents

---

Chapter 8 Conclusion and Outlook.....	87
List of Figures .....	89
List of Equations .....	92
Bibliography .....	95
Acknowledgements .....	101
声 明 .....	102
Resume, Publications and Research Achievements.....	103

## Nomenclature

RF	radio-frequency
DC	direct-current
UHV	ultrahigh vacuum
Yb	ytterbium
PMT	photomultiplier tube
RWA	rotating wave approximation
NA	numerical aperture
EMCCD	electron-multiplying charge-coupled device
CW	continuous wavelength
PBS	polarizing beam splitter
BS	beam splitter
UV	ultraviolet
PM	polarization maintained
AOM	acousto-optic modulator
EOM	electro-optic modulator
EOD	electro optic deflector
PD	Photodetector
TTL	transistor-transistor logic
DOE	diffractive optical element
FPGA	field-programmable gate array
COM	center-of-mass
GHZ	Greenberger-Horne-Zeilinger
POVM	positive operatorvalued measure
SPAM	state preparation and measurement
PTM	Pauli transfer matrice
GST	gate set tomography

# Chapter 1 Introduction

## 1.1 Quantum computing with high fidelity

Quantum computers<sup>[1]</sup>, as a new and powerful tool for complex computing tasks, can extend classical computational reach in diverse research fields, including quantum chemistry, material science, and even machine learning. The basic unit of a quantum computer is a quantum bit (qubit). Different from bits of a classic computer, qubit states can not only exist alone but also coexist in the form of superposition states, which is called quantum parallelism. This feature can exponentially accelerate quantum computing process and store a large amount of information. However, the observation of computing results and the extraction of the stored information would compromise the advantages due to the probabilistic quantum measurement. After each measurement, quantum superposition states would collapse to a single outcome, which leads to repeated measurements to obtain sufficient samples for the extraction of computing results or stored information. In order to maximize the power of quantum computers, exploring schemes like quantum Fourier transformation to construct quantum information with less samples is a very important task.

Based on recent development in quantum technology, quantum systems capable of coherently operating tens to hundreds of qubits may be realized within a few years<sup>[2]</sup>. Such a quantum system may not pose a threat to widely used cryptographic technologies like the RAS encryption algorithm, which is inconsistent with people's original expectations. However, this progress will open a new field to go beyond the computing power of the most powerful supercomputer at present. As well-known IT companies such as Google, IBM, Microsoft, Intel, Honeywell, and start-up companies such as IonQ and Rigetti joined the development of quantum computers, competition in the field of quantum computing is accelerating. Nevertheless, quantum systems containing tens to hundreds of qubits can be a starting point of a long journey to develop fully functional quantum computers in the future. We are still exploring the possibility of efficiently solving problems that classical computers cannot solve, by using quantum computer without complete quantum error correction capabilities.

Nowadays, various quantum applications have been pursued with currently available devices mainly through quantum-classical hybrid schemes<sup>[3-4]</sup>. The schemes com-

bine the advantages of classical and quantum computation, where quantum processors are used to estimate expectation values of physical observables on certain states for classical feedback. The hybrid schemes can be applied to estimate the ground state energies of molecules<sup>[4-6]</sup>, to simulate quantum models in materials<sup>[7]</sup> and high-energy physics<sup>[8]</sup> and to find approximate solutions of optimization problems<sup>[9]</sup>. Although it is anticipated that around a hundred well-behaved qubits are required for such schemes to outperform current classical counterparts in quantum chemistry<sup>[10-12]</sup>, the advantages are only possible with accurate quantum processors. However, when running target quantum circuits on noisy quantum devices, output results are inevitably deviated because of errors originated from both environmental fluctuations and operational imperfections. As the number of qubit and the depth of the circuit increase, the infidelity of output results would be tremendous due to the accumulation of error. It will lose all the advantages of quantum computing because of untrustworthy. Therefore, techniques for improving the accuracy of noisy quantum processors are of great importance.

Apart from physically improving the devices, the deviations of output results of running quantum circuits can be suppressed on the algorithmic level. For example, quantum error correction<sup>[13-14]</sup> provides a mean of fault-tolerant quantum computation. However, quantum error correcting codes require complex coding schemes, a large number of physical qubits and low error rates, which are still far from being affordable for near-term quantum technologies<sup>[2,15]</sup>. Consequently, it has not yet been demonstrated that quantum fault tolerance protocols can increase the fidelity of computation operations in any physical implementation. Alternatively, for the quantum algorithms estimating expectation values, the reliability of computation result can be improved by recently proposed error mitigation schemes<sup>[16-20]</sup> without challenging requirements for quantum error corrections, which provides a comprehensive way to mitigate errors in expectation estimation tasks<sup>[17-18,21]</sup>.

## 1.2 Quantum error mitigation

There are two categories of the quantum error mitigation schemes, i.e. the zero-noise extrapolation<sup>[16-17]</sup> and the probabilistic error cancellation<sup>[17-18]</sup>. The first method extrapolates the results to the zero-noise limit from experiments of varying noise levels, which has been applied to the variational optimization of certain Hamiltonians<sup>[19-20]</sup>. It is theoretically simple and experimentally easy to implement, and the reliability highly

depends on the presumed error model of a noisy quantum device. On the contrary, the probabilistic error cancellation scheme provides a systematic and self-consistent way to characterize and rectify the impact of errors on the output of noisy quantum computation. It begins with characterizing imperfect operations on the quantum device by tomography technique and then cancels errors by sampling random quantum circuits, according to a quasi-probability distribution derived from reconstructing ideal quantum operations with characterized imperfect ones.

The current stage of quantum computer research is called the "Noisy Intermediate-Scale Quantum" (NISQ) stage<sup>[2]</sup>, which will become the cornerstone of a fault-tolerant quantum computer. It is expected that building fully functional quantum computers that are not affected by errors still has a long way to go. At present, various physical platforms, including trapped ion systems, superconducting circuits, quantum dots, and optical sub-systems, have made great progress. The unified standard to evaluate the development mainly contains three parts: the coherence time of qubits, the error rate of logic gates, and the number of entangled qubits. Recent research about the three aspects shows that ion trap systems are still in a leading position in the development of quantum computing systems<sup>[22-24]</sup>.

In this thesis, we present the construction of a trapped-ion system with full controllability and investigation of the universal validity of the probabilistic error cancellation method in a general quantum computational context. We apply the method to every imperfect elementary quantum operation and benchmark the performance of error-mitigated quantum computation<sup>[25]</sup>. We observe significant improvements on effective gate fidelities of single- and two-qubit gates by two and one orders of magnitude to those of physical gates, respectively. Here, the effective gate fidelities are obtained by fitting the corresponding expectation values estimated with error mitigation, which are not actual physical gate fidelities. The cost of the error mitigation increases with the circuit depth, therefore, techniques like quantum error correction are still needed for large-scale fault-tolerant quantum computation. With technologies to tackle the cross-talk error, the probabilistic error cancellation method of quantum error mitigation can be straightforwardly applied to systems with more qubits for realizing high-fidelity quantum computation, which can open up the possibility of implementing high-fidelity computations on a near-term noisy quantum device.

### 1.3 Thesis structure

In chapter 2, I will introduce the basic principle of trapped ion system and talk about our five-segment blade trap, including the geometric structure, electrode control, and the bifilar helical resonator. The detailed trap-assembling process will be discussed in the chapter 4. The knowledge about  $^{171}\text{Yb}^+$  will also be introduced here.

In chapter 3, I mainly focus on the quantum manipulation for trapped ion system, including laser-ion interaction, microwave operation, Raman laser operation and state initialization. The spin-dependent force will also be introduced, which is the key part to realize our entanglement gate in chapter 5 and chapter 6.

In chapter 4, I will talk about the blade trap system setup in detail, including the trap-assembling procedure, the technique of making photonic crystal fiber cable, and building the individual addressing system with EOD or multi-channel AOM approach.

In chapter 5, I will introduce our research about global entangling gates on arbitrary ion qubits. The single-mode and multi-mode approaches are both discussed with the pulse scheme and the experimental realization. The GHZ state preparation result through global gate is shown there.

In chapter 6, I will discuss the quantum error mitigation technique and show our improved effective single- and two-qubit fidelity through randomized benchmarking method. The gate set tomography technique and maximum likelihood estimation scheme will be also introduced.

Chapter 7 is the conclusion and outlook.

## Chapter 2 Trapped $^{171}\text{Yb}^+$ ion system

### 2.1 The Paul trap

#### 2.1.1 Principle of trapping ions

According to Earnshaw's theorem<sup>[26]</sup>, charged particles cannot be trapped in a stable equilibrium by electrostatic field. One general option is through radio frequency(RF) oscillating electric field and a static electric field(DC) to confine charged particles, which is called the Paul trap<sup>[27-28]</sup>. In general, we can define three independent directions X, Y, Z in space. I mainly focus on the research of a linear ion-chain along the Z direction. So we need a dynamic confinement on the X-Y plane and a static potential confinement in the Z direction. The total potential form can be written as<sup>[29]</sup>

$$U(x, y, z, t) = \frac{V_{RF}}{2} \cos(\omega_{RF}t) \frac{x^2 - y^2}{R^2} + \frac{V_{DC}}{2} \frac{2z^2 - x^2 - y^2}{R^2}, \quad (2-1)$$

where  $V_{RF}$  and  $\omega_{RF}$  is the amplitude and frequency of the RF oscillating electric field,  $V_{DC}$  is the amplitude of the DC electric field, and  $R$  is the distance between the potential center (ion chain position) and the electrodes.

From equation (2-1), we may easily see the motion of the trapped ion in the X and Y directions are analogous and the frequency of motion in the two directions are same. We can rewrite the equation to the standard form of the Mathieu equation in the X direction:

$$\frac{d^2x}{d^2\tau} + [a_x - q_x \cos(2\tau)]x = 0, \quad (2-2)$$

where  $\tau = \frac{\omega_{RF}t}{2}$ ,  $a_x = \frac{4eV_{DC}}{m\omega_{RF}^2 R^2}$ , and  $q_x = \frac{2eV_{RF}}{m\omega_{RF}^2 R^2}$ . Here,  $m$  and  $e$  are the mass and charge of the ion. The exact solution of the Mathieu equation has plenty terms, but we have the lowest-order approximation in the case ( $|a_x|, q_x^2 \ll 1$  ( $q_x^2 \ll 1$  is also the requirement of a stable trap<sup>[29]</sup>), which is good enough for us to understand the ion's motional trajectory :

$$x(t) = x_0 \cos(\omega_x t) \left[ 1 + \frac{q_x}{2} \cos(\omega_{RF} t) \right], \quad (2-3)$$

where  $\omega_x = \sqrt{a_x + q_x^2/2}$ . We can easily see it can be approximated as a simple harmonic oscillator with a trap frequency  $\omega_x$ . The rest part is the micro-motion term, which should



be as small as possible and can be compensated by adding some finite DC potential fields (we will talk about it later).

From the calculation above, we know the trap frequencies of X and Y directions are same, which is not convenient for our setup and sideband cooling (we will talk about it later). We need another one DC potential field to split the motional modes to two independent directions and make them not to be degenerate any more, which is

$$U_{sp}(x, y) = \frac{V_{sp}}{2} \left( 1 + \frac{x^2 - y^2}{R^2} \right), \quad (2-4)$$

where  $V_{sp}$  is the amplitude of the additional DC electric field. By combining equations (2-1) and (2-4), and using the similar method, we can get two different trap frequencies as  $\omega_x = \sqrt{a'_x + q_x^2}/2$  and  $\omega_y = \sqrt{a'_y + q_y^2}/2$ , where  $q_y = -q_x$ ,  $a'_x = \frac{4e(V_{sp}-V_{DC})}{m\omega_{RF}^2 R^2}$  and  $a'_y = \frac{4e(V_{sp}+V_{DC})}{m\omega_{RF}^2 R^2}$ .

### 2.1.2 Blade trap

In order to apply all the electric fields for trapping ions stably, the 3D structure of electrodes should be designed properly. The four-rod trap system was used previously, as shown in fig. 2.1. The opposite two RF electrodes are connected with a same RF field, together with the needle voltages DC1 and DC2 to achieve the ion trapping and the confinement in Z-direction. The ion position can also be shifted by changing DC1 and DC2. The other opposite two DC(ground) electrodes are connected with same DC field for splitting the motional modes in the X-Y plane(DC3). It needs another two electrodes for micro-motion compensation(DC4 and DC5). This design is proved a great setup for single-ion simulation experiment, but cannot confine a multi-ion chain stably based on our experience. We suspect the rough electrodes surface may introduce some RF noise on the DC electrodes, which results in unstable trapping potential.

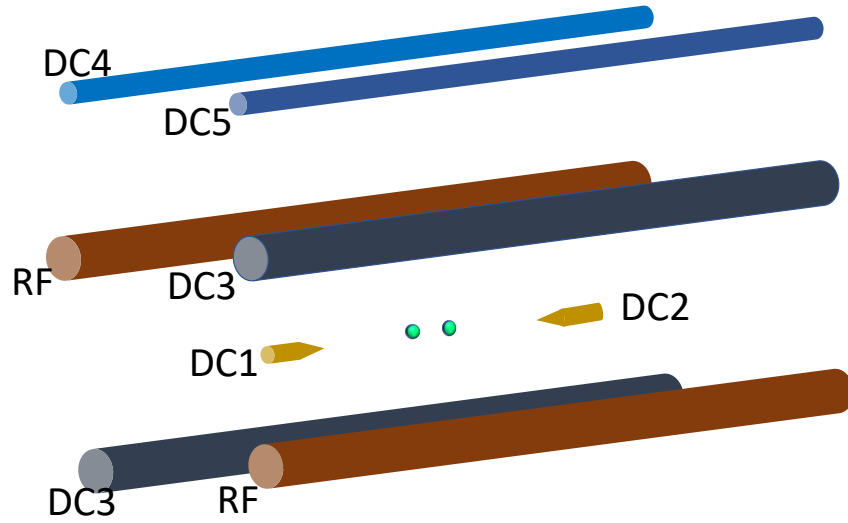


Figure 2.1 The general four-rod trap design and the electrodes connection

Now, we change the setup to five-segment blade trap system for several advantages compared with the four-rod trap. The micro-motion electrodes can be removed due to the sufficient freedoms from the segments design. And the distance between the ion and the electrodes can be much smaller due to the thinner blade shape, which benefits to achieve higher trap frequency with lower RF power. In addition, by designing the pattern of the DC field on each segment, we can achieve a uniform spacing with multi-ion condition. For now, we simplify the electrodes connection, as shown in fig. 2.2. The RF1 and RF2 fields together with DC1 and DC2 fields can realize the ion trapping. The ion position can also be controlled by adjusting DC1 and DC2 voltages. The DC3 and DC4 fields are used to split the motional modes in the X-Y plane. Here, It may be noticed that we separate the RF electrodes with RF1 and RF2 and add two different DC voltages on the two opposite DC(ground) electrodes(DC3 and DC4). So we can just add another one DC offset on RF2 electrode to get sufficient freedom for micro-motion compensation by controlling DC3, DC4 and DC5.

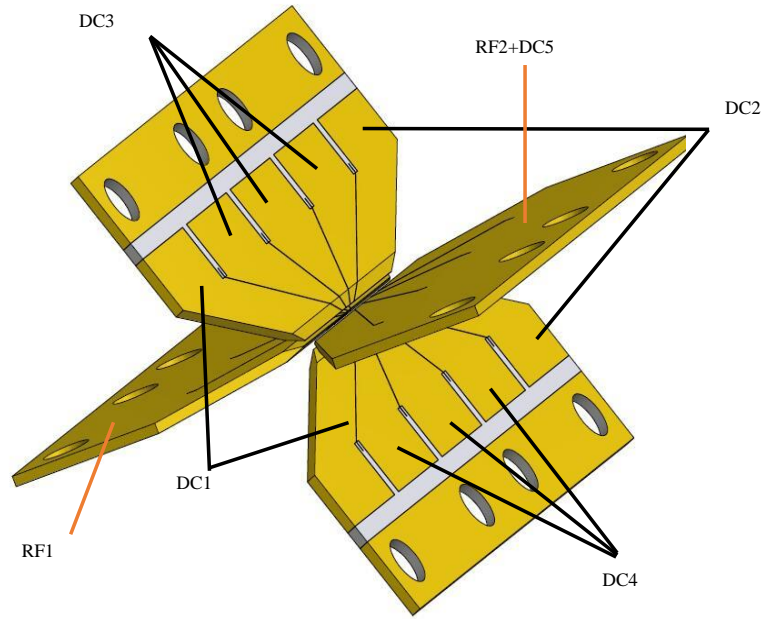


Figure 2.2 The blade trap design and the electrodes connection

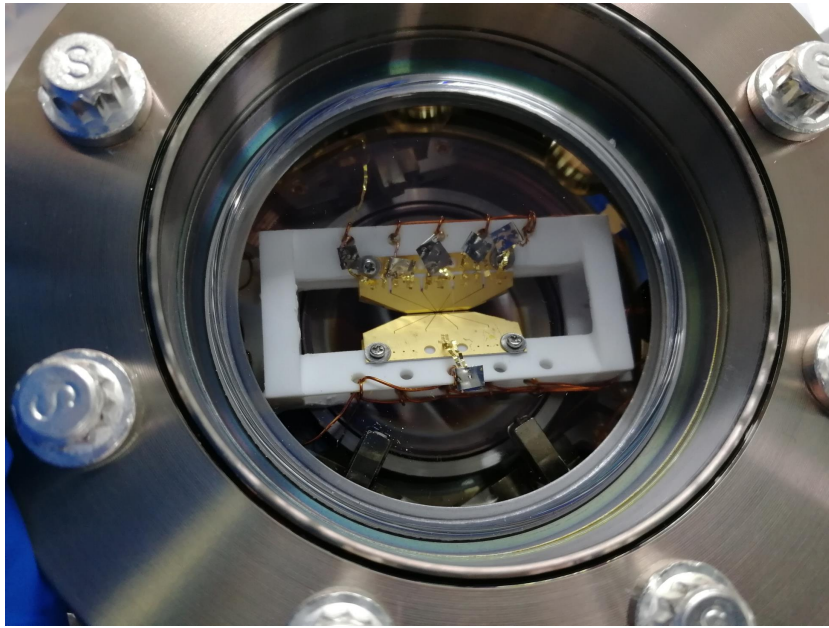


Figure 2.3 The assembled blade trap picture

The assembled blade trap picture is shown in fig. 2.3. The parameters in our blade trap setup are as follows:  $V_{RF}(RF1, RF2) \approx 600V$ ,  $V_{DC}(DC1, DC2) \approx 12V$ ,  $V_{split}(DC3, DC4) \approx 7V$ ,  $V_{micro-motion}(DC5) \approx 0.5V$ , and  $\omega_{RF} = 33\text{MHz}$ . Under these conditions, the trap frequency is  $\omega_x = 2\pi \times 2.2\text{MHz}$  and  $\omega_y = 2\pi \times 1.8\text{MHz}$ . With the UHV condition to minimize the background molecular impact<sup>[30]</sup>, we can stably trap

multiple ions, as shown in Fig. 2.4.

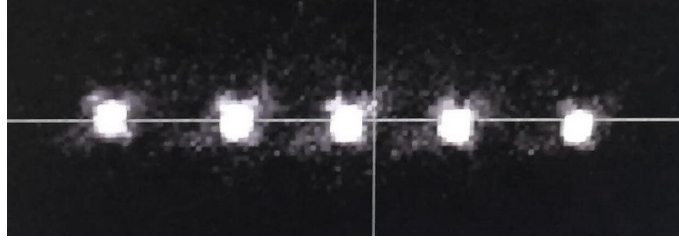


Figure 2.4 Ions figure.

### 2.1.3 Bifilar helical resonator

The RF oscillating electric field is one of the most important parts for trapping ions and should be "clean" and stable. The blade electrodes can be treated as a capacitor, which means it has high voltage but low current when applying RF field. Due to miss of impedance matching, the direct connection with signal generator does not work. So we introduce a device called helical resonator to solve this problem<sup>[31]</sup>, which can be treated as a special filter and amplifier. The quality factor  $Q$  is used to indicate its performance as  $Q = \frac{\omega_{RF}}{\delta\omega_{RF}}$ , where  $\delta\omega_{RF}$  is the full width half maximum. In order to obtain a higher  $Q$  factor, we can carefully design the structure and shield size, reduce the resistance inside by a stable connection and clean the shield.

The helical resonator mainly contains three parts: the small coil for input; the big inner coil for output and a shield. The original design just has one big inner coil, and the output is connected to the both RF electrodes, which results in insufficient degree of freedom for micromotion compensation without additional DC electrodes. We put two independent big inner coils side by side into the shield as a bifilar helical resonator and add a small DC offset to only one blade electrode(see fig. 2.2) for micromotion compensation through the corresponding big inner coil. The two big inner coils are connected by a 10nF capacitor for phase synchronization. We also add two capacitors(0.2pF and 20pF) in series between one big inner coil and ground to pick up 1% voltage as a feedback to stabilize the RF electric field to get a stable trap frequency, as shown in fig. 2.5. The measured  $Q$  factor is about 200.

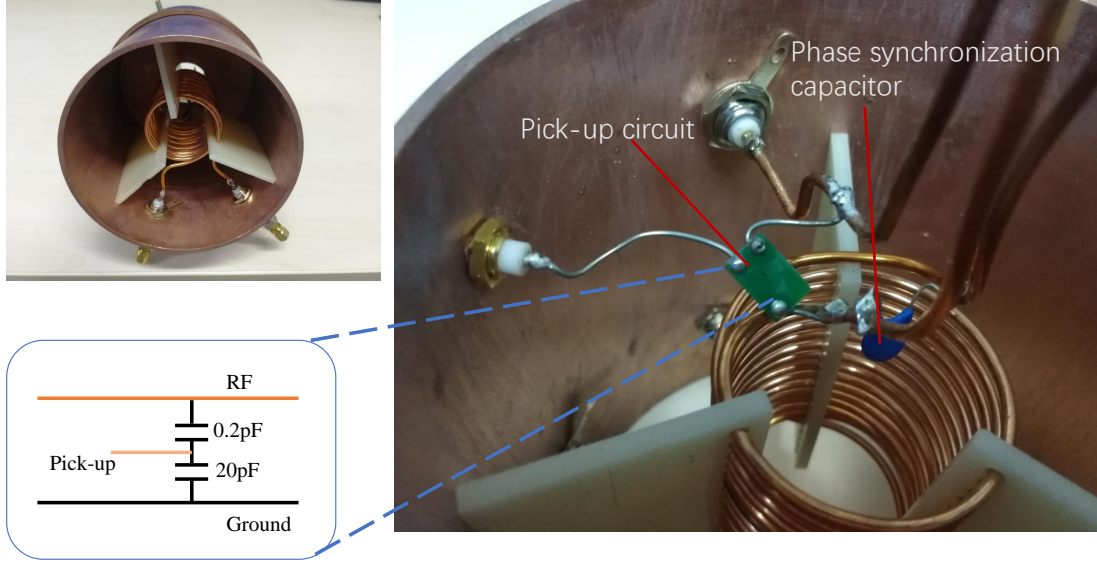
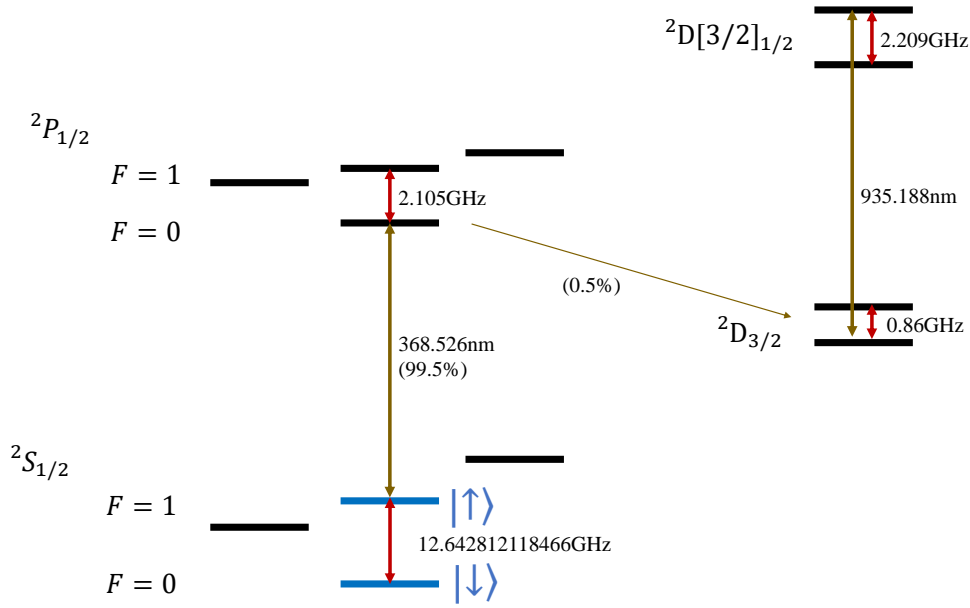


Figure 2.5 The stabilization of the RF power

## 2.2 $^{171}\text{Yb}^+$ ion

### 2.2.1 Energy structure

We choose  $^{171}\text{Yb}^+$  ion to encode a qubit, which has been studied and developed a lot for quantum simulation and computation by Maryland university<sup>[32-36]</sup>.  $^{171}\text{Yb}^+$  ion is a hydrogen-like ion, which has a simple and "clean" energy structure. The simplified energy structure of  $^{171}\text{Yb}^+$  is shown in fig. 2.6<sup>[37]</sup>. The strong dipole transition  $^2S_{1/2} \leftrightarrow ^2P_{1/2}$  can be used for Doppler cooling, optical pumping and state detection. By applying magnetic field, the hyperfine structure will not be degenerated and split into Zeeman levels. A pair of clock states in the ground-state manifold  $^2S_{1/2}$ , i.e.  $|F = 0, m_F = 0\rangle$  and  $|F = 1, m_F = 0\rangle$ , are denoted as the computational basis  $\{|0\rangle, |1\rangle\}$  of a qubit, which has an extremely long relaxation time ( $T_1$ ), is insensitive to magnetic field fluctuations, and can reach 10 minutes coherence time<sup>[22]</sup>.

Figure 2.6 Energy structure of  $^{171}\text{Yb}^+$ 

### 2.2.2 Ionization of $^{171}\text{Yb}$ atom

The  $^{171}\text{Yb}$  atom is ionized based on the two-photon step<sup>[38-39]</sup>. We use an atom oven to emit atom beam by heating it up with certain current. The emitting direction is right to the trap center. The  $398.911\text{nm}$  laser can excite the  $^{171}\text{Yb}$  from  $1S_0$  to  $1P_1$  level and the  $369.526\text{nm}$  laser can make it emit an electron and become an ion. The two beams are overlapped in the trap center. Once the atom is ionized, the RF field can capture the ion immediately. Through the Doppler cooling scheme,  $^{171}\text{Yb}^+$  ion can stably rest in the potential center. The optical system around the trap is shown in fig. 2.8. In practice, we combine the  $399\text{nm}$  and  $370\text{nm}$  lasers as one beam for easier alignment. To cover more ions and make the most of the laser power, we use a diffractive optical element (DOE) bought from HOLO/OR as a beam shaper to change the round beam shape to a rectangle shape with  $180\mu\text{m} \times 60\mu\text{m}$  on the ion position. The typical power of  $399\text{nm}$  and  $370\text{nm}$  laser are around  $1\text{mW}$  and  $0.6\text{mW}$ .

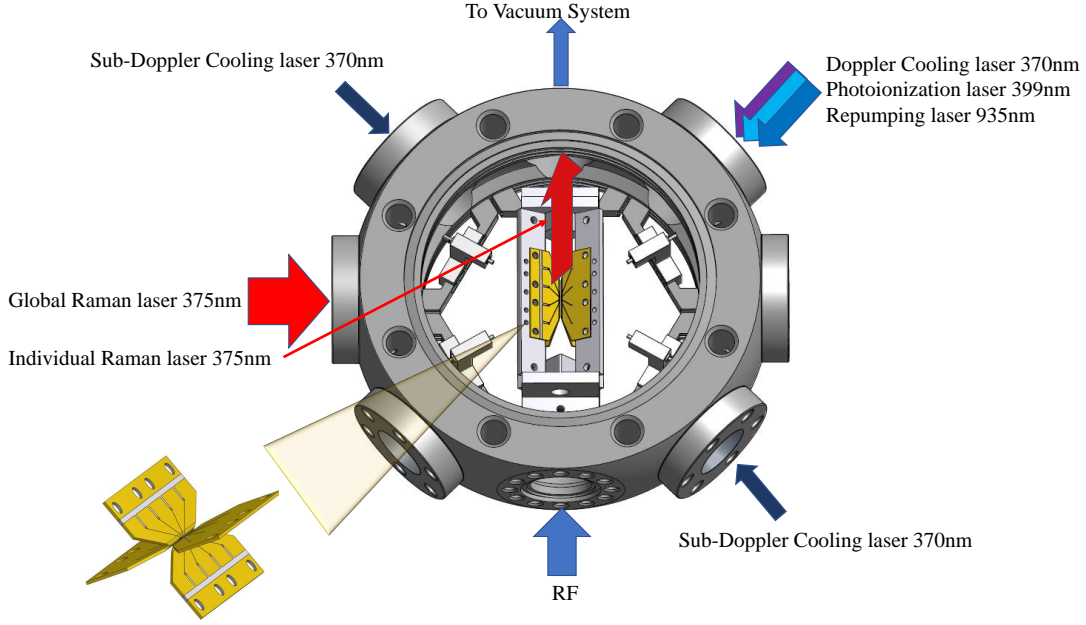


Figure 2.7 Optical system setup

### 2.2.3 Doppler cooling and repumping

We use the strong dipole transition  $^2S_{1/2} \leftrightarrow ^2P_{1/2}$  to cool down the ions. The basic idea of Doppler cooling is that the ion absorbs a photon and excites from  $^2S_{1/2}$  state to  $^2P_{1/2}$  state, then emits a photon through spontaneous decay. The emitted photon is in all directions with equal probability, which results in the momentum loss of the ion motion on average<sup>[40]</sup>.

The typical Doppler cooling scheme is shown in fig. 2.8. In experiment, we shine a 370nm laser for the basic cooling cycle, which is red-detuned from the resonance of transition  $^2S_{1/2} |F = 1\rangle \leftrightarrow ^2P_{1/2} |F = 0\rangle$ . However, when the ion is in state  $^2P_{1/2} |F = 1\rangle$ , it may decay to  $^2S_{1/2} |F = 0\rangle$  through spontaneous emission due to the other allowed transition  $^2S_{1/2} |F = 1\rangle \leftrightarrow ^2P_{1/2} |F = 1\rangle$ , which needs an additional sideband of 370nm laser to close the cycle of Doppler cooling. Since the transition  $^2S_{1/2} |F = 0\rangle \leftrightarrow ^2P_{1/2} |F = 0\rangle$  is forbidden, the alternative option is using the transition  $^2S_{1/2} |F = 0\rangle \leftrightarrow ^2P_{1/2} |F = 1\rangle$  by adding a 14.74GHz sideband of 370nm to close the cooling cycle. The shape and power of Doppler cooling laser is  $180\mu\text{m} \times 60\mu\text{m}$  and about  $10\mu\text{W}$ .

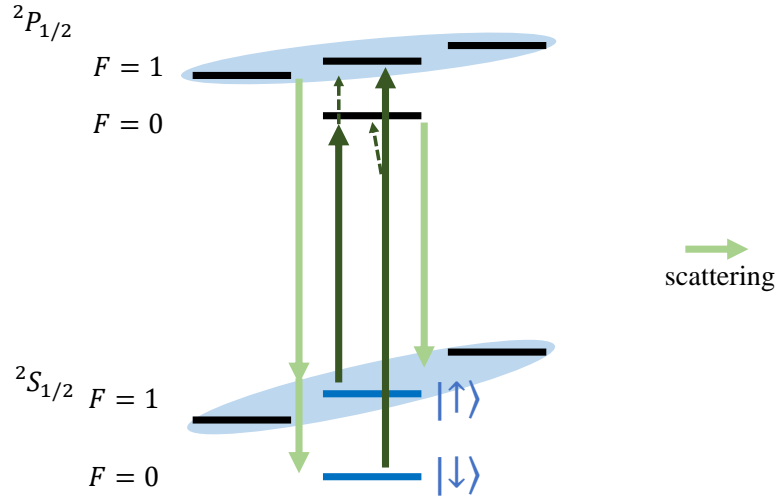


Figure 2.8 Doppler cooling scheme. The solid line means resonant stimulating and spontaneous emission. The dash line means off-resonant stimulating.

There is still 0.5% leakage from the state  $^2P_{1/2}$  to  $^2D_{3/2}$ . We need a repumping laser 935nm with 3.1GHz sideband to repump the state from  $^2D_{3/2}$  to  $^2D[3/2]_{1/2}$ . The state  $^2D[3/2]_{1/2}$  can quickly decay to  $^2S_{1/2}$  state through spontaneous emission(see fig.2.6).

Sometimes, the ion could be in the dark state  $^2F_{7/2}$  through the background collision. The 638nm laser or the 355nm(375nm) Raman pulse laser can help to bring it back to the cycle of Doppler cooling. Now, we find the 760nm laser also works well<sup>[41]</sup>.

#### 2.2.4 Detection

We manifold the ground state  $^2S_{1/2}$ , i.e.  $|F=0, m_F=0\rangle$  and  $|F=1, m_F=0\rangle$  as a qubit state. These two states can be distinguished by photon fluorescence through the transition  $^2S_{1/2} \leftrightarrow ^2P_{1/2}$ . The detection scheme is shown in fig. 2.9<sup>[42]</sup>. In experiment, we shine a 370nm laser, which is resonant with the transition  $^2S_{1/2} |F=1, m_F=0\rangle \leftrightarrow ^2P_{1/2} |F=0, m_F=0\rangle$ . We can collect photon fluorescence if the ion is in state  $^2S_{1/2} |F=1, m_F=0\rangle$ , which is called "bright" state. Correspondingly, the other state is called "dark" state for no fluorescence due to the 14.7GHz detuning. The typical shape and power of detection laser is  $180\mu\text{m} \times 60\mu\text{m}$  and  $3\mu\text{W}$ .



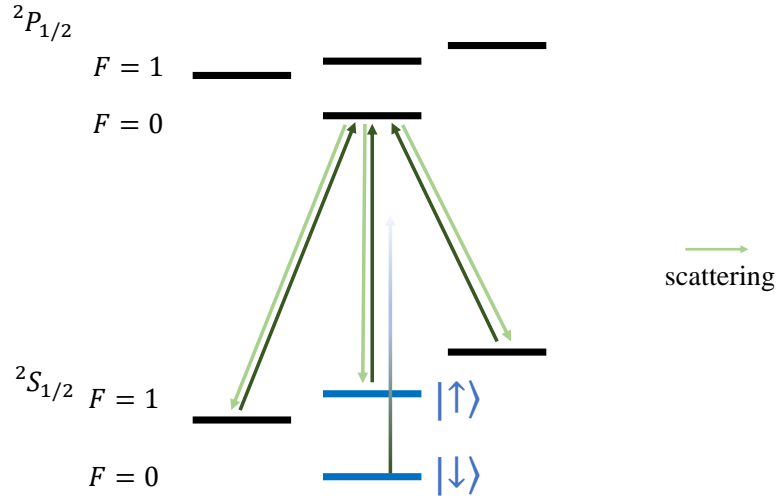


Figure 2.9 Detection scheme.

Typically, for single-ion detection, we use a single-channel photomultiplier tube (PMT), taking the advantages of its high sensitivity and low noise. Our general detection time is  $300\mu\text{s}$  by using a CVI objective lens ( $\text{NA}=0.2$ ). Now we change it to High NA objective lens ( $\text{NA}=0.6$ ), which can collect about 7% scattering photons<sup>[43-44]</sup>, and the detection time can be reduced to  $60\mu\text{s}$ . The typical detection fidelity is 99.6%.

For multi-ion detection, we first use Andor EMCCD, taking advantages of its low detection crosstalk between the photon fluorescence from each ion. Due to the limitation of its data-taking procedure and some programming problems, the typical detection time is  $800\mu\text{s}$  and the average detection fidelity is about 96%. So we try to reduce the detection time by using the multi-channel PMT (32-channel). However, we found the quantum efficiency of multi-channel PMT we bought is four times lower than that of the single-channel PMT, and the detection time can only be reduced to  $200\mu\text{s}$ . In addition, the detection crosstalk is a little larger than that of EMCCD. Now, we try to replace it by fiber array solution, combining the advantages of short detection time, high detection fidelity and low crosstalk.

## Chapter 3 Quantum manipulation

### 3.1 Laser-ion interaction

The clock states of  $^{171}\text{Yb}^+$  ion, which are insensitive to magnetic fields, can be denoted as the computational qubit. We define them as spin  $|\downarrow\rangle$  and  $|\uparrow\rangle$  state. The Hamiltonian of a two level system can be written as

$$H_e = \hbar \frac{\omega_0}{2} \sigma_z, \quad (3-1)$$

where  $\omega_0$  is the energy level difference of spin  $|\downarrow\rangle$  and  $|\uparrow\rangle$ . In addition, the ions are trapped with the RF oscillating field, and its motion can be approximated as a harmonic oscillator. We can write down the motional Hamiltonian as

$$H_m = \hbar \omega_m (a^\dagger a + \frac{1}{2}), \quad (3-2)$$

where  $a^\dagger$  and  $a$  are the creation and annihilation operators, and  $\omega_m$  is the frequency of motional mode. In principle, we have three motional modes in X, Y and Z directions. Here, we take just one mode as example, and the situations of the other modes are similar.

The general laser-ion interaction Hamiltonian can be written as

$$H_i = e\vec{r} \cdot \vec{E} \cos(kx - \omega t + \phi),$$

where  $\omega$  is the frequency of laser, and  $k$  is the effective wave vector, which is chosen along the  $x$  direction for simplification. We can transform it to a coupling Hamiltonian as

$$H_i = \frac{\hbar \Omega}{2} (\sigma_+ + \sigma_-) (e^{i(kx - \omega t + \phi)} + e^{-i(kx - \omega t + \phi)}), \quad (3-3)$$

where  $\sigma_+ = |\uparrow\rangle\langle\downarrow|$ ,  $\sigma_- = |\downarrow\rangle\langle\uparrow|$  and the Rabi frequency  $\Omega = |e\vec{r} \cdot \vec{E}|/\hbar$ .

It is not straightforward to have an intuitive picture with the total Hamiltonian  $H_e + H_m + H_i$ . We can transform it into the interaction picture by defining the disengaged Hamiltonian  $H_0 = H_e + H_m$ . With the time evolution  $U_0 = \exp(-iH_0 t/\hbar)$ , the interaction

Hamiltonian can be written as<sup>[29]</sup>

$$\begin{aligned}
 H_I &= U_0^\dagger H_i U_0 \\
 &= \frac{\hbar\Omega}{2} e^{iH_0 t/\hbar} (\sigma_+ + \sigma_-) (e^{i(kx-\omega t+\phi)} + e^{-i(kx-\omega t+\phi)}) e^{-iH_0 t/\hbar} \\
 &= \frac{\hbar\Omega}{2} e^{i\omega_0 \sigma_z t/2} (\sigma_+ + \sigma_-) e^{-i\omega_0 \sigma_z t/2} H_I^m \\
 &= \frac{\hbar\Omega}{2} (\sigma_+ e^{i\omega_0 t} + \sigma_- e^{-i\omega_0 t}) H_I^m,
 \end{aligned} \tag{3-4}$$

where  $H_I^m = e^{iH_m t/\hbar} (e^{i(kx-\omega t+\phi)} + e^{-i(kx-\omega t+\phi)}) e^{-iH_m t/\hbar}$  is the motional part and not straightforward to calculate. Here, we can consider that in the Heisenberg picture, the operator  $x$  follow the evolution<sup>[29]</sup>  $x(t) = x_0 [aw^*(t) + a^\dagger w(t)]$ , where  $x_0 = \sqrt{\frac{\hbar}{2mv}}$  is wave packet widening of the ground state and  $w(t)$  is the corresponding solution according to the driven field. So we can cleverly write down the motional part of interaction picture as

$$H_I^m = e^{i[\eta(a^\dagger e^{i\omega_m t} + ae^{-i\omega_m t}) - \omega t + \phi]} + e^{-i[\eta(a^\dagger e^{i\omega_m t} + ae^{-i\omega_m t}) - \omega t + \phi]}, \tag{3-5}$$

where  $\eta = kx_0$  is called Lamb-Dick parameter.

Using rotating-wave approximation, we can get the simplified interaction Hamiltonian as<sup>[29]</sup>

$$H_I = \frac{\hbar\Omega}{2} (\sigma_+ e^{i[\eta(a^\dagger e^{i\omega_m t} + ae^{-i\omega_m t}) - \delta t + \phi]}) + H.c., \tag{3-6}$$

where  $\delta = \omega - \omega_0$  is the laser detuning from the ion energy gap. We can control the laser intensity, frequency and phase to manipulate the ion with flexible freedoms.

## 3.2 Microwave operations

Microwave operation is one of the most robust and handy implementations of quantum gates, but its Lamb-Dick parameter  $\eta \ll 1$ , close to zero. From equation (3-6), the part  $\eta(a^\dagger e^{i\omega_m t} + ae^{-i\omega_m t}) \approx 0$ , and we get the interaction Hamiltonian of microwave as

$$H_M = \frac{\hbar\Omega}{2} (\sigma_+ e^{i(\phi-\delta t)} + \sigma_- e^{-i(\phi-\delta t)}). \tag{3-7}$$

It is obvious that the microwave cannot drive any transition related to phonon number change.

In experiment, the frequency of microwave is very close to the qubit energy gap.

With  $\delta = 0$ , the rotation of the qubit state on the Bloch sphere can be defined as

$$\begin{aligned} R_\phi(\theta) &= e^{-iH_M t/\hbar} \\ &= e^{-i\frac{\theta}{2}(\sigma_+ e^{i\phi} + \sigma_- e^{-i\phi})}, \end{aligned} \quad (3-8)$$

where  $\theta = \Omega t$  is the rotation angle and  $\phi$  determines the rotation axis. We cannot directly apply the rotation on Z axis. One method is to apply three rotations as

$$R_z(\theta) = R_{-\pi/2}(\pi/2)R_0(\theta)R_{\pi/2}(\pi/2).$$

The other way is using off-resonant coupling. By setting  $\Omega \ll \delta$ , we can also achieve the rotation on Z axis. But the speed is lower than the previous one, which is proportional to  $\Omega/\delta$ .

### 3.3 Raman laser operations

#### 3.3.1 Carrier, blue sideband and red sideband transitions

Except for the microwave, the stimulated Raman transition is another way to implement quantum gates. We use the 375nm pulse laser (mira) to achieve the two-photon transition through the energy levels  $^2S_{1/2}$  and  $^2P_{1/2}$ . The Lamb-Dick parameter is much larger than that of microwave as  $\eta \approx 0.1$  for the single-qubit case. In the Lamb-Dick regime, we can apply Taylor expansion to equation (3-6) and keep the lowest order in  $\eta$ . The interaction Hamiltonian of Raman laser can be approximated as

$$H_L = \frac{\hbar\Omega}{2}\sigma_+[1 + i\eta(a^\dagger e^{i\omega_m t} + a e^{-i\omega_m t})] + H.c.. \quad (3-9)$$

By setting the detuning  $\delta$ , we can get three resonances as carrier transition, blue sideband transition and red sideband transition

$$\begin{aligned} H_{car} &= \frac{\hbar\Omega}{2}(\sigma_+ e^{i\phi} + \sigma_- e^{-i\phi}), \delta = 0 \\ H_{bsb} &= i\frac{\hbar\Omega}{2}\eta(\sigma_+ a^\dagger e^{i\phi} - \sigma_- a e^{-i\phi}), \delta = \omega_m \\ H_{rsb} &= i\frac{\hbar\Omega}{2}\eta(\sigma_+ a e^{i\phi} - \sigma_- a^\dagger e^{-i\phi}), \delta = -\omega_m, \end{aligned} \quad (3-10)$$

Here, the phase  $\phi$  is the relative phase between the two Raman beams.

The carrier transition can drive the transition  $|\downarrow, n\rangle \leftrightarrow |\uparrow, n\rangle$  with Rabi frequency  $\Omega$ . The blue sideband transition can drive the transition  $|\downarrow, n\rangle \leftrightarrow |\uparrow, n+1\rangle$  with Rabi frequency  $\sqrt{n+1}\eta\Omega$ . And the red sideband transition can drive the transition  $|\downarrow, n\rangle \leftrightarrow$

$|\uparrow, n-1\rangle$  with Rabi frequency  $\sqrt{n}\eta\Omega$ , as shown in fig. 3.1. Since  $\eta \approx 0.1$ , the Rabi frequencies of first order blue and red sideband transitions are about ten times slower than that of the carrier transition.

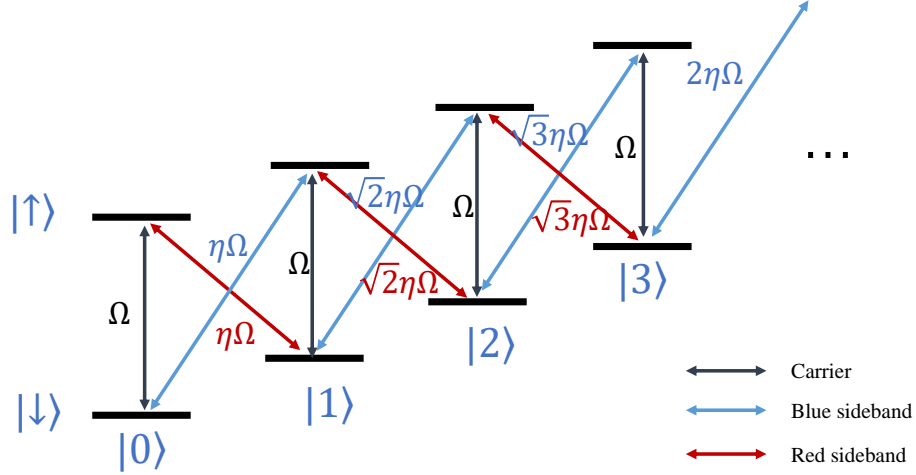


Figure 3.1 The three resonances with Raman laser.

### 3.3.2 Spin-dependent force

The effective laser field for carrier, blue sideband and red sideband transitions only contains a single frequency. By combining the blue and red sidebands with or without detuning, we can achieve the spin-dependent force operation<sup>[45]</sup>. In general, with  $\phi = 0$ , the Hamiltonian is

$$\begin{aligned}
 H_{sdf} &= H_{bsb} + H_{rsb} \\
 &= i\frac{\hbar\Omega}{2}\eta(\sigma_+ a^\dagger e^{-i\Delta t} - \sigma_- a e^{i\Delta t}) + i\frac{\hbar\Omega}{2}\eta(\sigma_+ a e^{-i\Delta t} - \sigma_- a^\dagger e^{i\Delta t}) \\
 &= \frac{\hbar\Omega}{2}\eta\sigma_y(a^\dagger e^{-i\Delta t} + a e^{i\Delta t}),
 \end{aligned} \tag{3-11}$$

where  $\Delta = \omega - \omega_m$  is the laser detuning from the ion's motional mode, and  $H_{sdf}$  is the spin-dependent force in  $\sigma_y$  basis. To have an intuitive picture, let's first consider the motional part with  $\Delta = 0$  as

$$H_{fm} = \frac{\hbar\Omega}{2}\eta(a^\dagger + a). \tag{3-12}$$

It's easy to derive the time evolution, which results in the displacement operator as

$$D(\alpha) = e^{\alpha a^\dagger - \alpha^* a}, \quad (3-13)$$

where  $\alpha = -i\eta\Omega t/2$ . Adding the spin part, the motion will entangle with the spin state. In general, our initial state is spin down state, which can be decomposed with the eigenstates of  $\sigma_y$  as  $|\downarrow\rangle = \frac{1}{\sqrt{2}}(|+_y\rangle + |-_y\rangle)$ . These two parts will be "pushed" out in the phase space, as shown in fig. 3.2a.

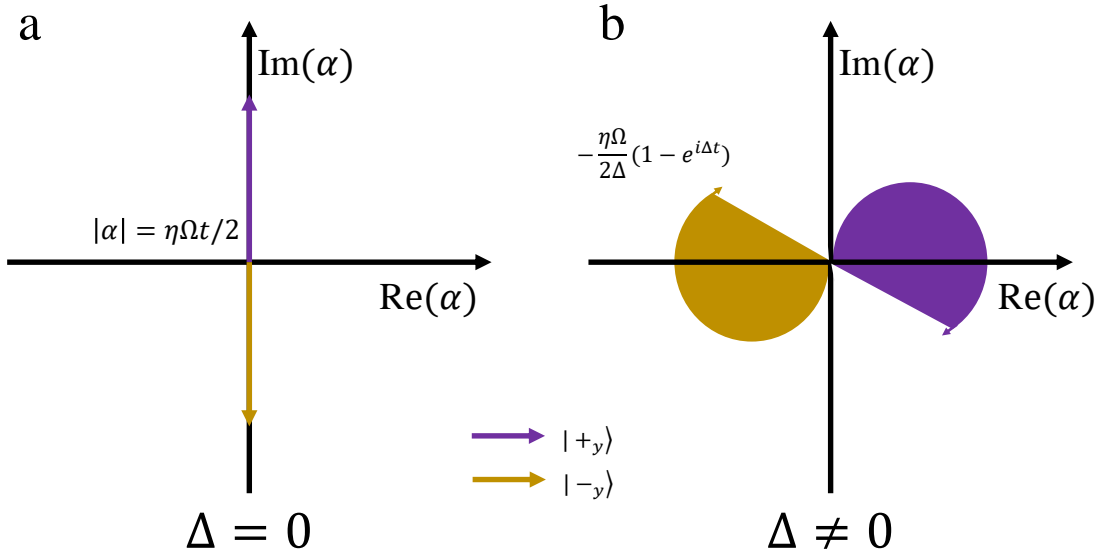


Figure 3.2 The motional trajectory in phase space with and without detuning.

If  $\Delta \neq 0$ , the two parts will go back to the original point through a circle in the phase space after time  $T = 1/\Delta$ , as shown in fig. 3.2b. The radius of the circle is  $\eta\Omega/(2\Delta)$ <sup>[46]</sup>. The enclosed area will accumulate a geometric phase with time (we will talk about it later). If we keep applying the spin dependent force, the number of turns of the trajectory will also contribute to the phase accumulation.

### 3.3.3 Mølmer-Sørensen gate

The two-qubit entangling gate is always the research interest during last several decades. Two popular approaches are the Cirac-Zoller (CZ) gate<sup>[47-48]</sup> and Mølmer-Sørensen (MS) gate<sup>[49]</sup>. The CZ gate directly uses the phonon state as intermediary, which really entangles the internal qubit and motional Fock state and depends on a good phonon state initialization to achieve a high entanglement fidelity. On the contrary, the MS gate

just uses the phonon as a "bus", which does not entangle any phonon state. The procedure is based on the geometric phase accumulation when coupling the qubit state with motional mode. After the gate time, the qubit and phonon states are decoupled. This method does not rely on a good phonon state preparation and is more robust to the phonon heating effect.

Here, let's first introduce the essential knowledge about the geometric phase. Geometric phase is caused by a phenomenon called "global change without local changes"<sup>[50]</sup>, which is based on a closed trajectory. In 1984, Berry's research<sup>[51]</sup> about cyclic evolution of system under adiabatic conditions shows the nonintegrable character of the geometric phase.

Considering a quantum system, the Hamiltonian  $\mathcal{H}$  changes with a varying parameter  $P(x_1, x_2, \dots)$ . Form time  $t = 0$  to  $t = T$ ,  $P$  has a closed trajectory, namely  $P(0) = P(T)$ . The state evolution can be described by the Schrödinger equation

$$H[p(t)] |\phi(t)\rangle = i\hbar \frac{\partial}{\partial t} |\phi(t)\rangle. \quad (3-14)$$

Assuming the system has a basis of discrete eigenstates  $|n[P(t)]\rangle$ , which satisfies

$$H[p(t)] |n[P(t)]\rangle = E_n[P(t)] |n[P(t)]\rangle, \quad (3-15)$$

where  $E_n[P(t)]$  is the eigenenergy. If the initial state of the system is  $|n[P(0)]\rangle$ , and adiabatically evolves from  $P(0)$  to  $P(T)$  in the parameter space, the eigenstates and energies will also continuously and slowly change and go back to the original place, as shown in fig. 3.3.

The state of the system can be written as

$$|\phi(t)\rangle = e^{i\theta_n} e^{ig_n} |n[P(t)]\rangle, \quad (3-16)$$

where  $\theta_n = -\frac{1}{\hbar} \int_0^t E_n[P(t')] dt'$  is the dynamical phase factor and  $g_n$  is the geometric phase factor. We can substitute it into Schrödinger equation (3-14) as

$$\frac{\partial}{\partial t} |n[P(t)]\rangle + i \frac{d}{dt} g_n(t) |n[P(t)]\rangle = 0. \quad (3-17)$$

Through inner product with  $\langle n[P(t)]|$ , we can get

$$\frac{d}{dt} g_n(t) = i \langle n[P]| \nabla_p |n[P]\rangle \frac{dP}{dt} \quad (3-18)$$

After the integration, the geometric phase can be written as <sup>[50]</sup>

$$g_n(C) = i \oint_C \langle n[P] | \nabla_P | n[P] \rangle dP, \quad (3-19)$$

which depends on the closed trajectory of  $P(t)$  in the parameter space and is nonintegrable.

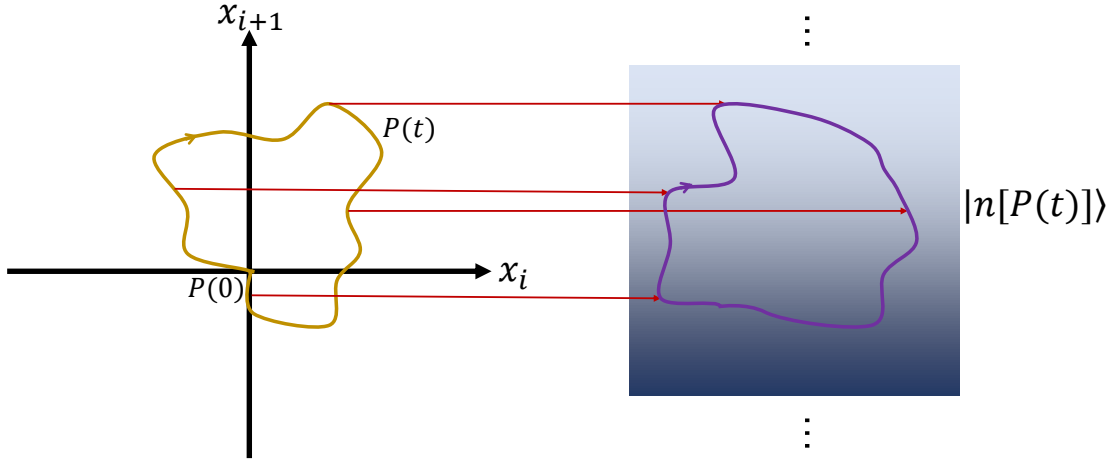


Figure 3.3 Schematic diagram for parameterized time evolution.

In 1987, Aharonov and Anandan<sup>[52]</sup> proposed a cyclic evolution that is not limited by adiabatic conditions. This is an extension of Berry's phase, which means that we don't need a parameter space to describe the cyclic evolution Hamiltonian, but only the projected Hilbert space that the system tracks to draw a closed curve. This generalization of Berry's phase is called Aharonov-Anandan phase.

Considering a Hilbert space HS, in which the time-dependent Hamiltonian is not cyclic, which means  $H(T) \neq H(0)$ , but the final state is similar to the initial state except a different phase

$$|\phi(T)\rangle = e^{i\Phi} |\phi(0)\rangle, \quad (3-20)$$

as shown in fig. 3.4.



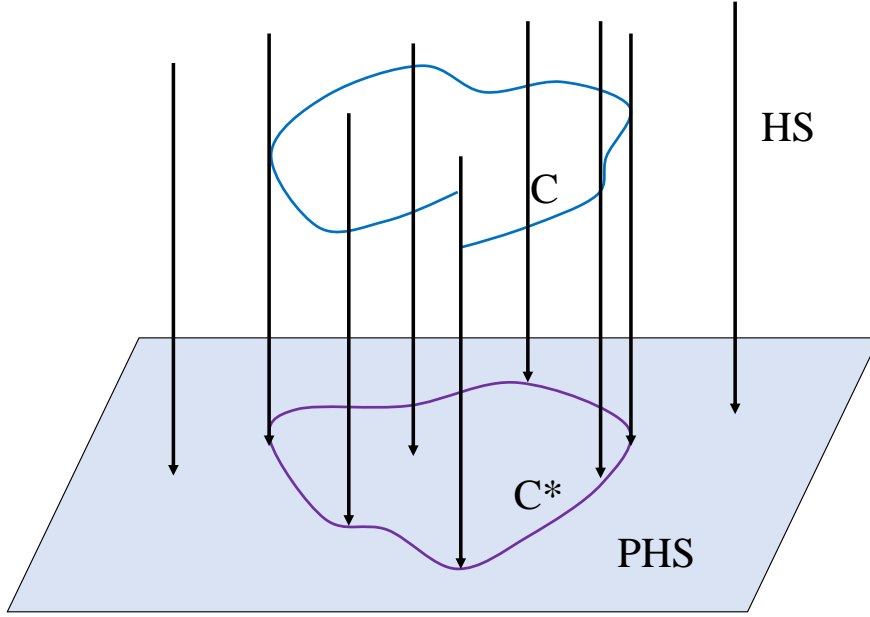


Figure 3.4 The cyclic evolution in the projective and normal Hilbert space.

The trajectory of  $P(t)$  in parameter space is not closed. But we can find a projective Hilbert space PHS, in which trajectory  $P^*(t)$  is closed and the corresponding state vector  $|\chi(t)\rangle$  satisfies

$$|\chi(T)\rangle = |\chi(0)\rangle. \quad (3-21)$$

The relation of state vector between the normal Hilbert space and the projective Hilbert space is

$$|\phi(t)\rangle = e^{i\alpha(t)} |\chi(t)\rangle, \quad (3-22)$$

where  $\alpha(T) - \alpha(0) = \phi$ . We can substitute it into Schrödinger equation (3-14), and obtain the equations for  $\alpha(t)$  and  $\chi(t)$ <sup>[50]</sup>

$$i\hbar \frac{d}{dt} |\chi(t)\rangle = (H + \hbar\dot{\alpha}) |\chi(t)\rangle \quad (3-23)$$

$$\hbar \frac{d}{dt} \alpha(t) = i \langle \chi | \frac{\partial}{\partial t} | \chi \rangle - \langle \chi | H | \chi \rangle. \quad (3-24)$$

After the integration for equation, we can get the phase

$$\Phi = \int_0^T \frac{d}{dt} \alpha(t) dt = \theta + \beta, \quad (3-25)$$

which contains two parts: The dynamical phase is

$$\theta = -\frac{1}{\hbar} \int_0^T \langle \chi | H | \chi \rangle dt = -\frac{1}{\hbar} \int_0^T \langle \phi | H | \phi \rangle dt. \quad (3-26)$$

And the geometric phase is<sup>[50]</sup>

$$\beta = i \oint_{C^*} \langle \chi | \frac{\partial}{\partial t} | \chi \rangle dt. \quad (3-27)$$

The Aharonov-Anandan phase does not need the requirement for cyclicity of time evolution of the system and is suitable for any initial state instead of the eigenstates of the Hamiltonian.

The Mølmer-Sørensen gate can be treated as the application of Aharonov-Anandan phase in trapped ion systems. We use Raman laser field to drive the internal state and motional modes, which is the dynamical way, rather than adiabatic way. When we implement the MS gate, the Hamiltonian of Raman laser is not a cycle with time and the trajectory of laser parameter like amplitude, frequency and phase is not closed. But we can project Hamiltonian to the phase space as the closed projective Hilbert space.

For simplicity, let's consider the two-qubit MS gate. In general, the two ions have two motional modes in each X, Y, and Z axis, we can take the X modes as example. The MS gate is implemented by applying the detuned blue and red sidebands to the both ions. The total Hamiltonian can be written as<sup>[46,53]</sup>

$$\begin{aligned} H_{sdf} &= \sum_{j=1}^2 \sum_{k=1}^2 i \frac{\hbar \Omega}{2} \eta_{j,k} (\sigma_{j,+} a_k^\dagger e^{-i\delta t} - \sigma_{j,-} a_k e^{i\delta t}) + H.c. \\ &= \sum_{j=1}^2 \sum_{k=1}^2 \frac{\hbar \Omega}{2} \eta_{j,k} \sigma_{j,y} (a_k^\dagger e^{-i\delta t} + a_k e^{i\delta t}), \end{aligned} \quad (3-28)$$

where  $j$  is the index of ions,  $k$  is the index of modes and  $\delta = \omega - \omega_0$  is the laser detuning from the ion energy gap.

It is similar with the case for single-qubit spin-dependent force with detuning. Here, we have two parts of spin terms  $\sigma_{1,y} + \sigma_{2,y}$  and two parts of motional terms  $(a_1^\dagger e^{-i\delta t} + a_1 e^{i\delta t}) + (a_2^\dagger e^{-i\delta t} + a_2 e^{i\delta t})$ . If we set the detuning in the middle of the two modes as  $\delta = \frac{\omega_{m1} + \omega_{m2}}{2}$ , these two modes will accumulate the geometric phase together with the same speed  $T = 1/(\omega - \omega_{m1})$ . It should be noticed that the sign of the geometric phase is controlled by the rotation direction of the trajectory. The two parts of spin terms can

also speed up the phase accumulation. Considering there are four basis states in the  $\sigma_y\sigma_y$  axis as  $|+_y+_y\rangle$ ,  $|-_y-_y\rangle$ ,  $|+_y-_y\rangle$ , and  $|-_y+_y\rangle$ , we can draw the four trajectories in phase space, as shown in fig. 3.5.

According to the area and direction of trajectories, we can write down the time evolution of the four basis states as

$$\begin{aligned}
 |+_y+_y\rangle &\longrightarrow e^{i\phi} |+_y+_y\rangle \\
 |+_y-_y\rangle &\longrightarrow e^{-i\phi} |+_y-_y\rangle \\
 |-_y+_y\rangle &\longrightarrow e^{-i\phi} |-_y+_y\rangle \\
 |-_y-_y\rangle &\longrightarrow e^{i\phi} |-_y-_y\rangle,
 \end{aligned} \tag{3-29}$$

where phase  $\phi = 2A$  and  $A$  is the area of the closed trajectory. We can adjust the laser intensity to control the Rabi frequency  $\Omega$  and change the gate time to obtain different geometric phase. Typically, if  $\phi = \pi/4$ , we call it the maximum entanglement. In general, the initial state of the system is spin down or spin up in  $Z$  basis. It is easy to change the state evolution in  $Y$  basis to  $Z$  basis. By setting  $\phi = \pi/4$ , we can get the GHZ state for the two-qubit case

$$\begin{aligned}
 |\downarrow\downarrow\rangle &\longrightarrow 1/\sqrt{2}(|\downarrow\downarrow\rangle + i|\uparrow\uparrow\rangle) \\
 |\downarrow\uparrow\rangle &\longrightarrow 1/\sqrt{2}(|\downarrow\uparrow\rangle + i|\uparrow\downarrow\rangle).
 \end{aligned} \tag{3-30}$$

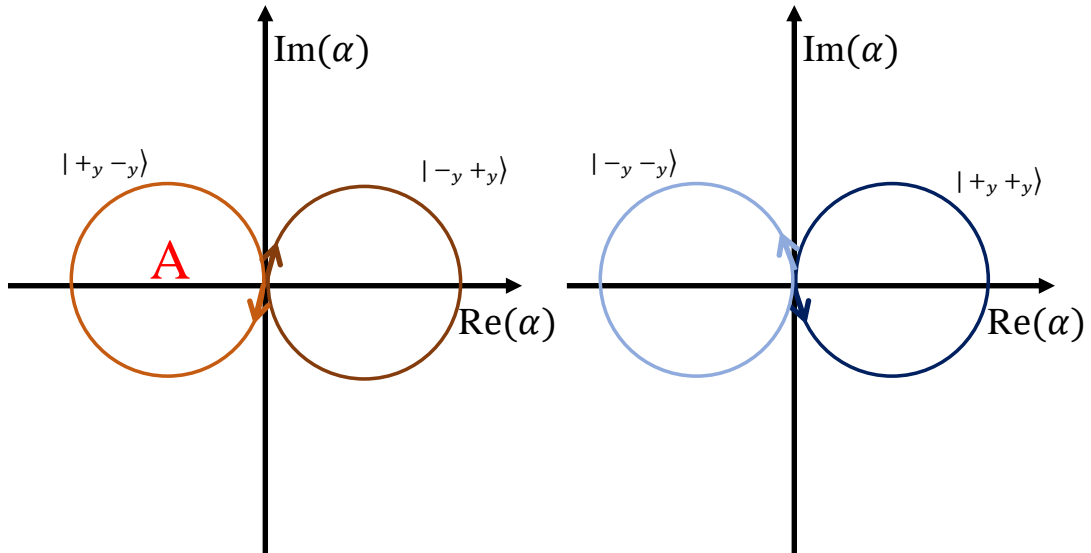


Figure 3.5 The trajectories of the four basis states in phase space.

## 3.4 State initialization

### 3.4.1 Optical pumping

We use the strong dipole transition  ${}^2S_{1/2} \leftrightarrow {}^2P_{1/2}$  for optical pumping to pump the ion qubit to the internal ground state  ${}^2S_{1/2} |F=0, m_F=0\rangle$ . The scheme is shown in fig. 3.6. In experiment, we shine a 370nm laser with a 2.105GHz sideband, which can cover the transition  ${}^2S_{1/2} |F=1\rangle \leftrightarrow {}^2P_{1/2} |F=0\rangle$  and  ${}^2S_{1/2} |F=1\rangle \leftrightarrow {}^2P_{1/2} |F=1\rangle$ . The state  ${}^2P_{1/2} |F=1\rangle$  can decay to  ${}^2S_{1/2} |F=0, m_F=0\rangle$  through spontaneous emission. Due to the far detuning,  ${}^2S_{1/2} |F=0, m_F=0\rangle$  state will not be excited. Since the state can also decay to  ${}^2D_{3/2}$  state, the 935nm repumping lase is also applied to bring it back to the optical pumping process. The typical shape and power of optical pumping laser is  $180\mu\text{m} \times 60\mu\text{m}$  and  $5\mu\text{W}$  with a 99.8% "dark" state fidelity.

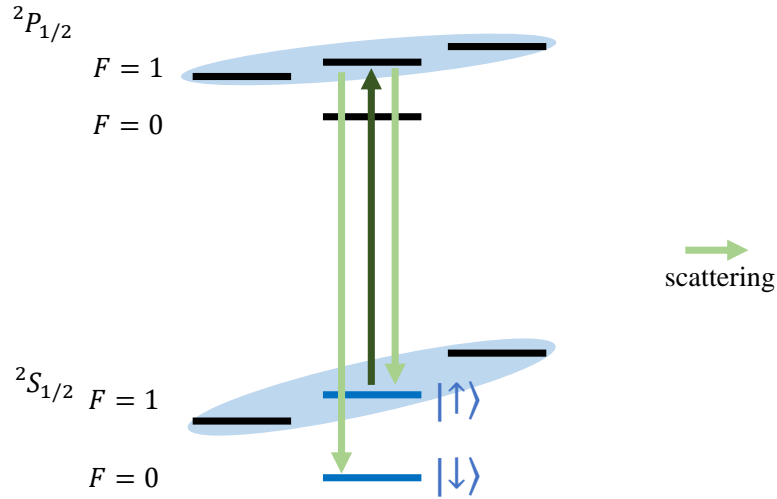


Figure 3.6 Optical pumping scheme.

### 3.4.2 Sideband cooling

The optical pumping can pump the internal state to ground, and the motional state should be also cooled down to the vacuum state for full quantum state initialization. After Doppler cooling, the motion of the ion is in a thermal state. If we apply carrier transition, the Rabi oscillation will quickly decay after several periods. Here, the sideband cooling technique is introduced. The basic idea is to apply red sideband transition and optical pumping alternately to create a "phonon slope". The distribution of phonon can slip to

the vacuum state along the designed path, as shown in fig. 3.7.

In experiment, we first use Doppler cooling limit to estimate the average phonon number. Then we estimate the average Rabi frequency of red sideband transition by the phonon distribution. We apply the sideband cooling procedure 100 times and can reach the average phonon number 0.012.

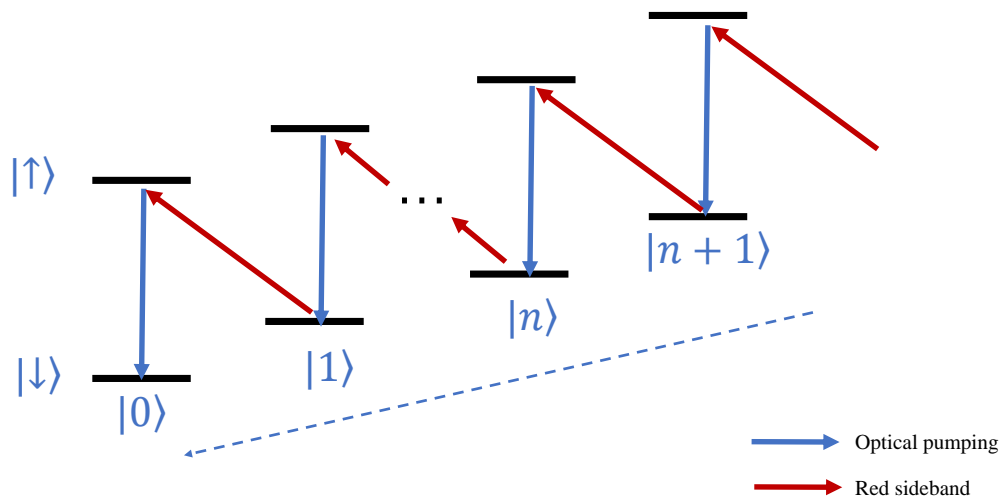


Figure 3.7 Sideband cooling scheme.

## Chapter 4 Blade ion trap system setup

### 4.1 System design through fiber connection

The ion trap system can be mainly divided into five components: blade trap system, CW laser system, pulse laser(microwave) system, detection system and control system. The blade trap system contains the atom oven for loading ions, RF electric field for trapping ions, DC field for confining ions, compensating micromotion, and splitting motional modes, and magnetic field for splitting the Zeeman levels. The CW laser system is used for system alignment, which contains the (topica) laser, the strong beam, the Doppler cooling and repumping beam, optical pumping beam and detection beam. The pulse laser system is used for quantum manipulation, which contains the (mira) laser, the two Raman beams(global beam and individual beams). The detection system is for quantum measurement, which contains single(multi)- channel PMT or camera and imaging system. The control system controls the laser and detection system, which contains computer for experiment design, and FPGA board for generating time sequence.

Our original design is using fiber(array) to connect the laser and detection system to the blade trap system. We combine the four 370nm laser beam to one beam through BS and PBS with half power loss, which is coupled to one fiber. The two Raman beams can be coupled into two fibers(array), separately. The fluorescence of each ion can also be collected independently by fiber array. This separated design has lots of advantages: It is convenient to optimize and scale up the whole system; the fiber can optimize the shape of laser beam and reduce the phase fluctuation; the fiber array can reduce the detection crosstalk to improve measurement fidelity.

Due to the limitation of our system, we actually make some compromises, as shown in fig. 4.1. The system we build is our first multi-qubit blade trap system and we do not have much experience to align the fiber array stably. So for the detection system, we still build it in free space. We find the stability of the mira laser is not good enough to match each individual beam to the fiber array well with conditions for experiment. In order to reduce the laser fluctuation and optimize the beam shape, we just add a fiber before the individual system setup. Due to the limitation of laser power and the fact that the global beam is much less sensitive to the laser shaking, the global beam is still directly aligned from the mira laser.

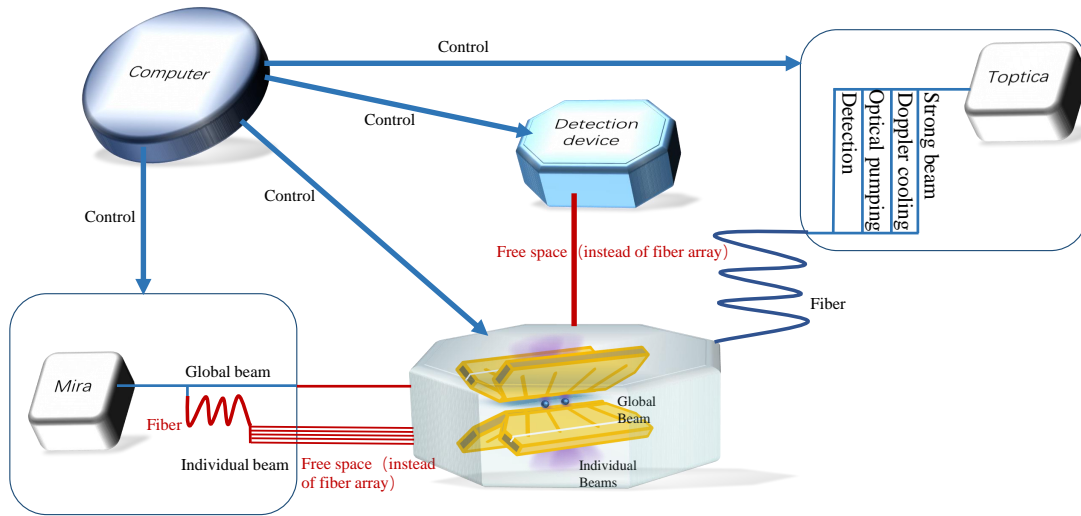


Figure 4.1 Blade trap system design.

Note that the maximum power of the CW laser is 10mW, we can use the normal fiber from thorlabs to couple CW laser beam. However, the average power of Raman laser can reach 500mW, and the peak power would be even higher. The normal fiber would be damaged immediately when coupling into so strong power. We use a special photonic crystal fiber, which can bear such high laser power level and has a single-mode output for full wavelength. But the fiber cable is not commercial, which needs a special process. The procedure of making fiber cable will be discussed later.

## 4.2 Blade trap assembling

### 4.2.1 Electrode connection

The blade material is alumina ceramics. We design five segments of independent electrodes. We send our design drawing to Delong laser Ltd. for laser cutting, and discuss a lot of times for the thickness of the top edge, which we want as thin as possible. But it is easier to be broken when it is thinner. We have two versions, one is  $30\mu m$ , and the other one is  $60\mu m$ . We use microscope to compare the flatness of the surface and decide to use the  $60\mu m$  version. Then we cooperate with Dayu electronic Ltd. for the gold coating. For the DC blade, we need to draw the coating pattern to separate each segment electrode. The RF blade is all-coated by gold. They first coat 10nm titanium, then coat 3um gold. We want the gold layer as thick as possible, but 3um is the maximum of electroplate method.

After we receive the coated blade, we also use the microscope to check the flatness of gold layer and the completion of laser cutting. Everywhere we designed should be all coated by gold. If there is alumina exposed, it may be charged when we apply the RF electric field or the strong Raman beam, which will keep shifting the position of ion and affect its stability. The designed blade picture and the real blade are shown in fig. 4.2.

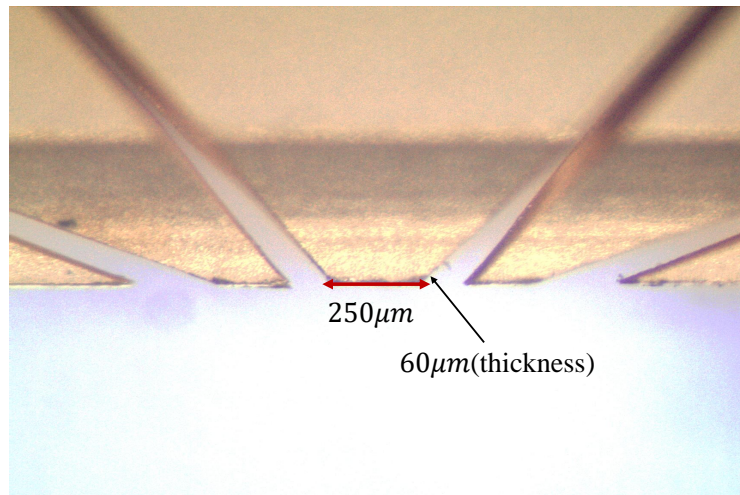


Figure 4.2 The five-segment blade picture.

We bought a machine from West Bond Inc., which can attach a gold ribbon to the surface of the blade. The gold ribbon and the blade should be both heated to around  $200^{\circ}\text{C}$  and the operating parameter should be tested first, including the pressure and time. Otherwise, the attachment may be not stable enough or easy to break off. We decide to attach two ribbons on each electrode for insurance.

The other side of gold ribbon is connected to a wire through a spot welder machine. We use a piece of stainless steel to wrap the gold ribbon and the wire, then use a pulse current around  $3\text{A}$  to heat it up. Then, the gold ribbon and the wire are attached to the stainless steel piece. The parameter of current should be also tested first.

The strong RF electric field on the blade will affect the ground blade, on which we will also add DC voltage for splitting the motional modes or compensating micromotion. The filter system should be added on the DC electrodes. Before, we put the filter system outside of the trap. We observe that when we load more and more ions, the stability of the ion chain becomes worse and worse. We suspect that the filter outside does not work



well and there is still RF noise on the DC electrodes. So in the latest version of blade trap, we decide to put the capacitor inside the trap, just on the surface of the blade. We first cut two short gold ribbons and attach one on each surface of capacitor. Then the other sides of the two ribbons are attached the DC electrode and the ground, separately, as shown in fig 4.3.

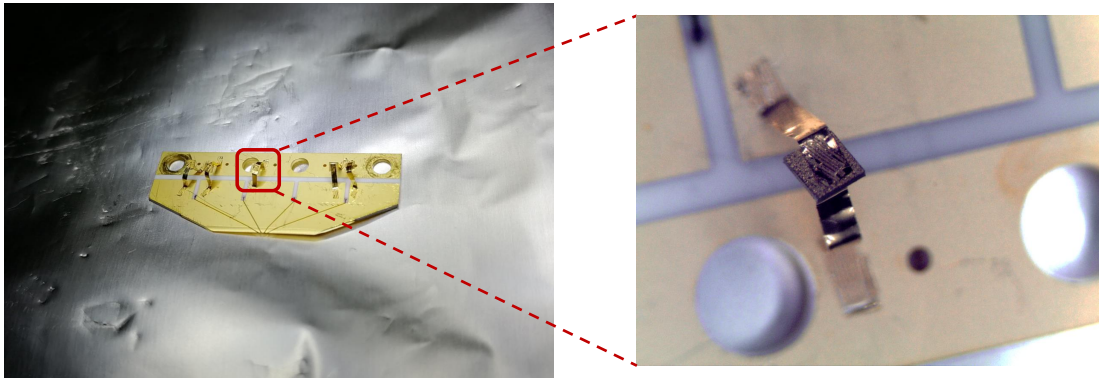


Figure 4.3 The attached capacitor picture.

#### 4.2.2 3D structure assembling

The potential shape of RF electric field is very sensitive to the 3D structure of the four blades, which should be symmetry and uniform. The design of 3D structure has some considerations. After assembling the blades, the blades can not block the laser path and affect the fluorescence collecting. Since we are using high NA(0.6) objective lens, the angle facing to the detection system should be carefully designed. And in order to have the capability to rotate the principle axis of X, Y motional modes, the shape of the center cannot be a square. We decide to make it a rectangle with  $400\mu\text{m} \times 200\mu\text{m}$ .

We draw the structure in Autodesk inventor software to make sure it meets all the requirements, and design a holder to fix the blades. In the first version, the holder has two parts. One is a piece of alumina to hold the blade without electrical connection and decide the distance between the ion and the blade. The other one is a piece of stainless steel to decide the angle of the blade in the 3D structure. When assembling them together, we find it usually deviates from the design due to the limitation of manufacture precision.

In the latest version, we combine the two holders as one alumina holder.

During assembling, we actually first roughly fix the blades on the holder. Before carefully optimizing the 3D structure, we do the spot welder connection. For one reason, we add several additional holes to twine and hole the wire. It is safer and more convenient to do spot welder connection when we have fixed the wire. Otherwise, the twining may drag the gold wire and destroy all of the process. For the other reason, optimizing the 3D structure is the most important part during assembling, which we want to leave to the last step in case that the structure changes after other assembling process. The blade trap picture with electric connection is shown in fig. 4.4.

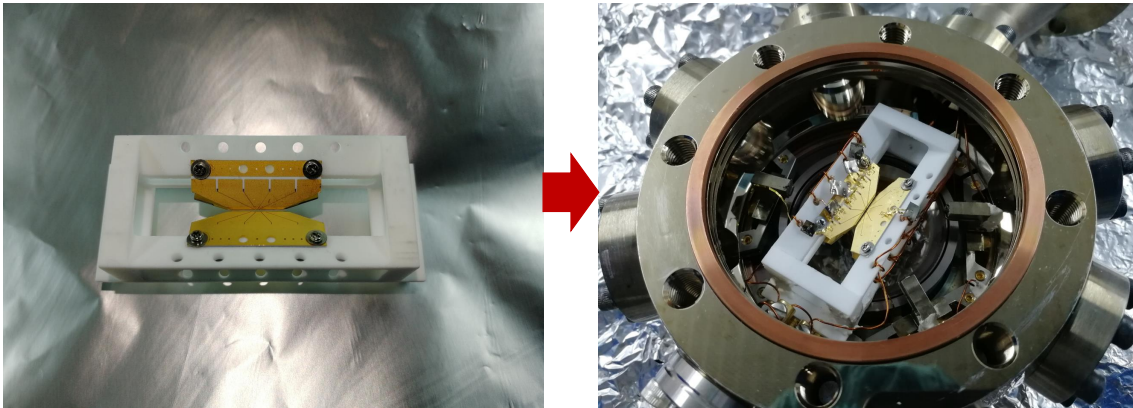


Figure 4.4 The assembled trap picture.

The blades are attached to the holder with screws. In order to adjust the distance between blades and the whole structure, the screw hole in the holder is a little larger than the diameter of the screws. The four blades should be as uniform as possible in the Z direction, and each segment on the blade should match with that on the other blade face to face as exactly as possible. It needs patience and takes long time to make it perfect. We use microscope to check the quality of the 3D structure and measure the rectangle size of the center, as shown in fig. 4.5 and fig. 4.6. The two figures are obtained with the same microscope magnification. From the measurement in fig. 4.5,  $D1 \approx 168\text{pixels}$  and we know the corresponding real length is about  $250\mu\text{m}$ , so each pixel means  $1.49\mu\text{m}$ . Then, we can get the real 3D structure size through  $D3$  and  $D4$  in fig. 4.6 as  $380\mu\text{m} \times 205\mu\text{m}$ ,

which is quite close to our design.

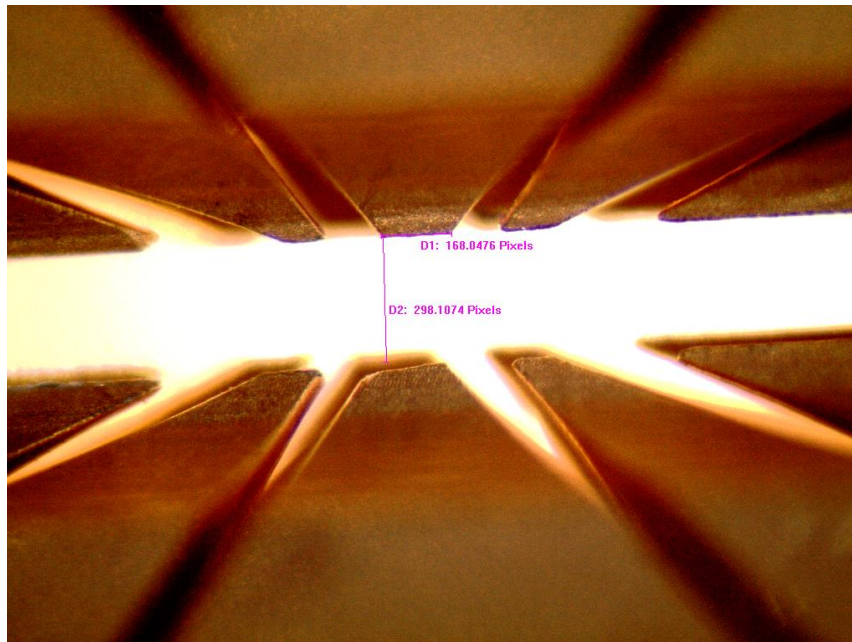


Figure 4.5 The symmetry quality through microscope.



Figure 4.6 The 3D structure of blade trap through microscope.

### 4.2.3 Vacuum system

After finishing assembling the "core" of the trap, we put the structure to the vacuum system. The RF wires and atom oven wires are connected to the two-pin and four-pin feed-

through. The 10 DC wires (we have two DC blades and each blade has five electrodes) are connected to a 19-pin feed-through. The correspondence between each pin and each electrode is recorded carefully.

Before, we use an ion pump and a titanium sublimation pump to maintain the UHV. The ion pump has a great capability of absorbing molecules except for hydrogen, and the titanium sublimation pump makes it up, which makes our system very huge and clumsy. Now we use the new NEG pump to replace them. Although the NEG pump contains an ion pump and a getter pump, it is still very small and light. The whole system is shown in fig. 4.7. Here, we should notice that when opening a new NEG pump for the first time, we should avoid the moist air to damage the ion pump part by purging into dry nitrogen.



Figure 4.7 The blade trap picture with vacuum system.

Typically, all the stainless steel components should be baked with  $300^{\circ}\text{C}$  for several days in advance. After we finish assembling the whole vacuum system, we put it into our baking oven to start pump process. We first open the mechanical pump and turbo-molecular pump, which work well for big molecules. When the vacuum is below  $10^{-6}$  Torr, we start to increase the temperature to  $150^{\circ}\text{C}$  slowly within 24 hours (The maximum temperature the magnet inside the NEG pump can take is  $150^{\circ}\text{C}$ ). At the same time, we open the getter pump with conditioning mode. When the temperature has reached  $150^{\circ}\text{C}$  and the vacuum is still below  $10^{-6}$  Torr, we open the big ion pump. After several days, when the vacuum of big ion pump is below  $10^{-8}$  Torr, we close the big ion pump

and start to decrease the temperature to 100°C within 18 hours. Then we do the degassing of the ion pump inside the NEG pump and change the getter pump to activation mode for several hours. After that, we close the bakeable valve of trap system and close mechanical pump and turbo-molecular pump. Finally, we decrease the temperature to the room temperature to finish the whole pumping process. After that, we can automatically reach a UHV system quickly.

### 4.3 Photonic crystal fiber cable

We bought the photonic crystal fiber from NKT Photonic.Inc, which is just a bare fiber and cannot be directly used in experiment. Surely, we can buy the commercial fiber cable with the same type. But it will get damaged soon when coupling strong pulse laser due to the lack of the hydrogen loading<sup>[54]</sup>, which the company cannot provide. We bought two types of bare fiber: one is LMA-10-UV, which is just a single mode fiber and not polarization-maintained specially. The other one is LMA-PM-10-UV, and PM means polarization-maintained. These two types of fiber both have the 10 $\mu$ m core diameter and the hole array around the core. The procedure of making the special fiber cable contains three steps: hydrogen loading, connectorization and curing.

#### 4.3.1 Hydrogen loading

The bare fiber should be put into the hydrogen(99.95%) at room temperature with high pressure about 10MPa for around two weeks. We first contract the Institute of Semiconductors in Beijing, who has the instrument to finish this procedure. Then, we find the Department of Electronics in Tsinghua University also have the capability to do it, which is more convenient to us. After the hydrogen loading, the fiber should be kept in very low temperature to prevent the diffusion of hydrogen until we finish the whole procedure. Here, we use dry ice to store the hydrogen-loaded fiber. Actually, the order of hydrogen loading and connectorization can be exchanged, and connectorization first may be better for storing the fiber in principle. We did not do it in that way because the size of the hydrogen loading instrument cannot hold the connectorized fiber.

#### 4.3.2 Connectorization

We cooperate with the Lambda company to do the connectorization, which needs machines like fiber splicer, fiber grinder and heating plate. The procedure should be done

as quickly as possible once the fiber is taken out from the dry ice.

The first step is removing the cladding part of the fiber. As we know, the bare fiber has three parts: core, coating and cladding part, and the inner diameter of the connector is matched with the coating diameter. It should be noticed that the coating diameter of the two types of fiber is a little different, which is around  $230\mu\text{m}$  for the LMA-10-UV and about  $280\mu\text{m}$  for the LMA-PM-10-UV. We use two different skinning knives to deal with them.

The second step is to collapse the fiber tip. This procedure will melt the holes around the core, which makes it easy to do the next curing process and can help to prevent the diffusion of hydrogen. We use the fiber fusion splicer to generate a pulse current to heat the tip, which may need to repeat several times to reach the collapsing length(about  $400\mu\text{m}$ ). And the parameter of fiber splicer including the current and time should be tested first and kept optimizing all the time.

The third step is connectorization. The inner diameter of the connector with  $250\mu\text{m}$  and  $300\mu\text{m}$  is chosen for the two different types of fiber. We put the coating part of the fiber into the connector and use high-temperature UV glue to fix it. The UV glue will solidify after we put the connector to the heating plate with  $200^{\circ}\text{C}$  for around 10 minutes. The high temperature is not good for maintaining the hydrogen, but we did not find a better solution for now.

The last step is to grind the fiber cable surface. We use a rough grinding plate first and change it more and more finely, which takes around 20 minutes.

### 4.3.3 Curing

After we finish the connectorization, we should start the curing procedure when the hydrogen is not much diffused out. The curing means that the fiber material and the hydrogen can interact when applying strong UV laser, which will change the property of the fiber and make it have capability to take high power laser<sup>[55-56]</sup>.

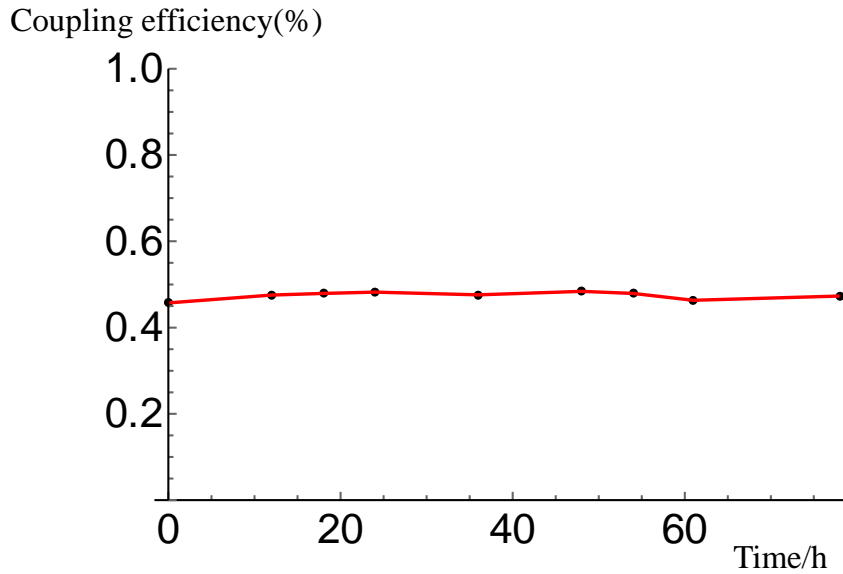


Figure 4.8 The coupling efficiency vs time during curing.

We couple the Paladin pulse laser with around 100mW average power into the fiber for 78 hours, which is long enough to finish the curing procedure. At the beginning, we want to finish the curing as soon as possible and do not pay much attention to improve the coupling efficiency(around 47%). We record the output power and the coupling efficiency change with time, as shown in fig. 4.8. After that, We carefully adjust the input beam diameter and the focal length of the collimator to do the mode matching and can reach the maximum coupling efficiency with 64%. We test the stability of the output power and the capability of the fiber for high input power 200mW, as shown in fig. 4.9. The result shows there is no obvious decay of coupling efficiency for 92 hours and the fiber has been used in our system very well.

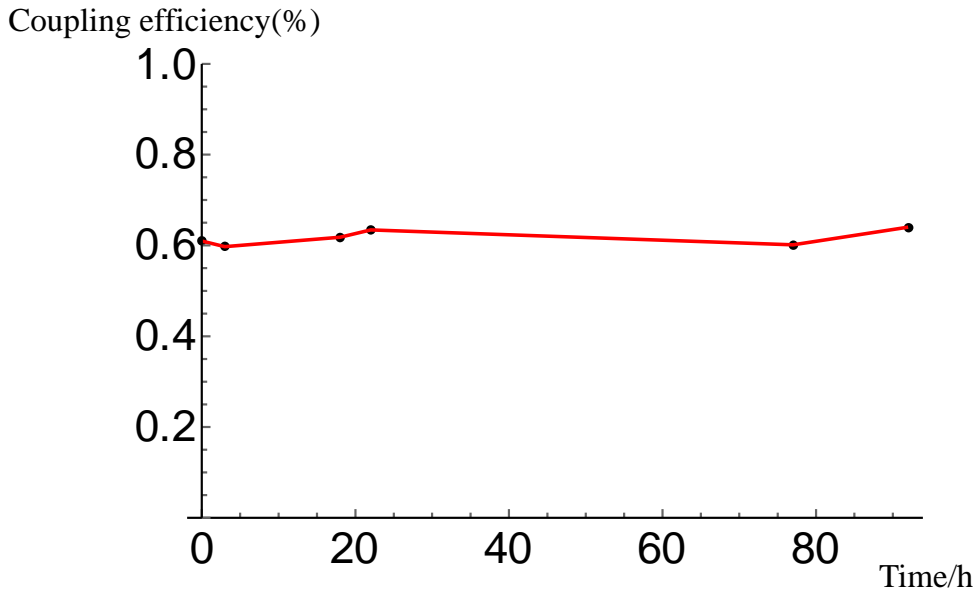


Figure 4.9 High power test result.

There are still some unsolved problems. We find sometimes after the fiber is used for around two months, the coupling efficiency may slowly decay. We can observe the obvious scattering around the connector on the beam input side. We suspect the damage may be caused by the dust in the air, and tried to purge the nitrogen to the collimator. Unfortunately, it does not help much. We are still trying to solve this problem. In addition, we do the connectorization in the factory now. After we finish the hydrogen loading, we send the fiber to the factory in JiangSu with dry ice. Then they send it to us after connectorization. The lifetime of the fiber is even worse than before. We think it is caused by the hydrogen diffusion during the delivery.

#### 4.4 Individual addressing system

For quantum manipulation, we use two photon process through two Raman beams shining the ions simultaneously. We design our individual addressing system by one horizontal global beam through the small viewport and one vertical individual beam through the big viewport in the bottom. The two beams has an angle with 90 degree, and can mainly excite one motional mode(X mode), which makes us ignore the other transverse mode(Y mode) for sideband cooling(See fig. 2.8). Originally, we want to design the individual beam through the horizontal viewport, too. It does not work due to too long distance between the small viewport and the ion.



The two Raman beams are splitted by a PBS from the laser source. The global beam is controlled by an AOM with frequency shift and switch on or off. In order to make sure the global beam can cover the whole ion chain and make the most of the laser power, we use two cylindrical mirrors to make the beam shape become an ellipse instead of a square. The two axis lengths of the ellipse beam on the ion plane are  $10\mu\text{m}$  and  $50\mu\text{m}$ . Considering that our typical separation between two ions is  $5\mu\text{m}$ , the global beam can cover almost 10 ions.

The other beam from the PBS goes into one photonic crystal fiber to stabilize the beam position and optimize the beam shape. We have two approaches for the setup of individual beams. One is using two EOD to control the two individual beams position, from which we can realize the single-qubit operations with arbitrary one ion and two-qubit entangling gate on arbitrary two ions within the ion chain. The other approach is multi-channel AOM approach. We bought a diffractive optical element (DOE) from HOLO/OR as a beam splitter to split one beam to five beams with equal intensity to match the multi-channel AOM.

#### 4.4.1 EOD approach

The EOD is an optical component which can control the output beam's angle through the driven voltage. We first use a simple optical alignment to test the relation between the angle and the driven voltage, as shown in fig. 4.10.

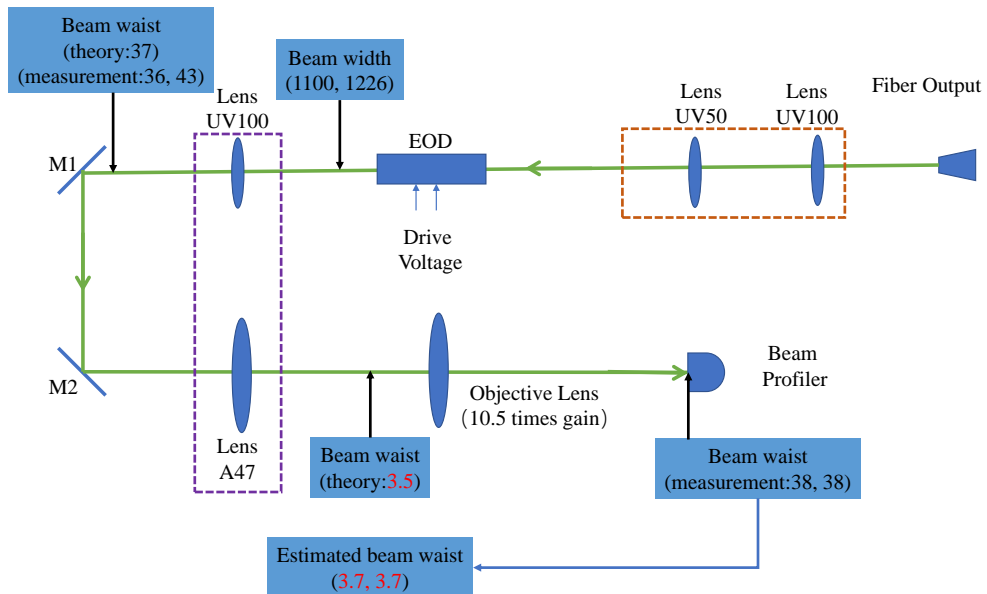


Figure 4.10 The optical path for testing the EOD quality.

The laser beam comes from the photonic crystal fiber. We use one UV100 and UV50 lenses(Thorlabs) to make the beam collimated with beam width around  $1100\mu\text{m}$ . After the beam goes through the EOD, we use two lenses(UV100 and UV47) to focus the beam to  $3.5\mu\text{m}$ . We want to use a beam profiler to directly measure the beam waist and quality. And the manual of beam profiler also claims that it can reach such high precision. However, according to our test, the measurement result of beam profiler cannot be trusted for the beam point smaller than  $15\mu\text{m}$ . And due to the rotation of the photosensitive element inside the device, the measured beam shape always has a "tail" for small beam point, as shown in fig. 4.11. So I add an objective lens to expand the beam waist by around 10.5 times. By measuring the final beam waist( $38\mu\text{m}$ ), we can estimate the beam waist on the focal point as  $3.7\mu\text{m}$ , which is quite close to our calculation.

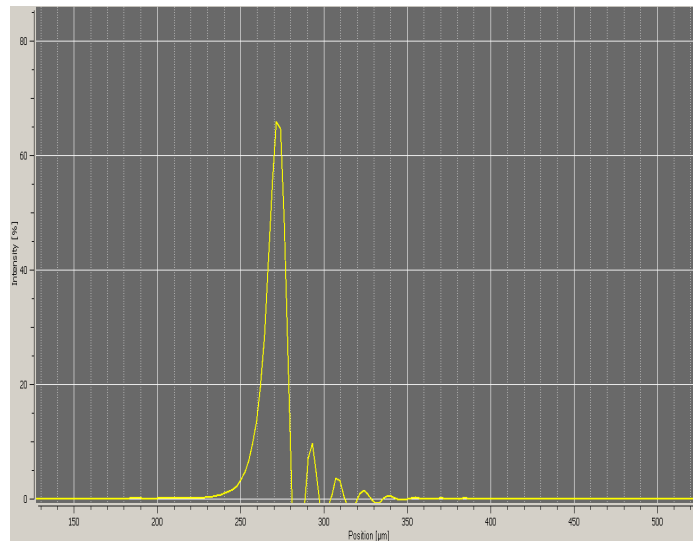


Figure 4.11 The fake beam shape "tail" with beam profiler device.

We measure the beam shift by changing the driven voltage step by step from  $-480\text{V}$  to  $480\text{V}$ , as shown in fig. 4.12, which is an almost perfect linear relation. The offset range  $220\mu\text{m}$  on the vertical axis is the imaging plane on the beam profiler. Considering the 10.5 times gain from the objective lens, we can get that the real offset range on the ion plane is around  $21\mu\text{m}$ , which can cover 5 ions in principle.

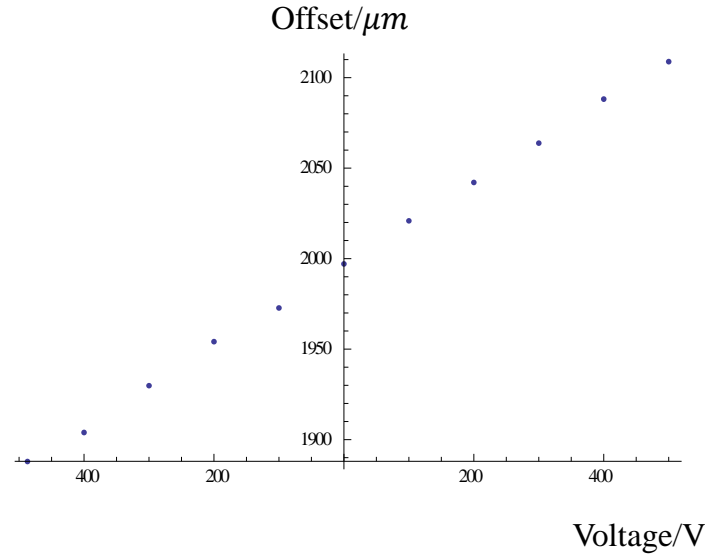


Figure 4.12 The offset on the beam profiler vs the driven voltage on the EOD.

Next, we test the responding speed of EOD by switching on or off the driven voltage. The setup is shown in fig. 4.13. We add a HWP and a PBS to reduce the power from the Paladin laser(3.75W). After the beam goes through EOD, we use a fiber to optimize the beam shape and reduce the beam fluctuation. Finally, we use a PD to measure the signal. By setting a TTL driven voltage and synchronizing it with the PD output, we can observe the signal rising and falling edges on the oscilloscope, as shown in fig. 4.14. The pink line is the TTL driven voltage signal and the green line is the PD signal. We can see the EOD works well when the TTL frequency is lower than 50KHz, and the rising edge time is around  $3\mu\text{s}$ . In our experiment, the typical gate time for single-qubit and two-qubit operation is around  $3\mu\text{s}$  and  $30\mu\text{s}$ , so the responding time of EOD is too long to finish our single-qubit operation and just may be used with two-qubit gate. We noticed there is another technique through shifting the beam position to do individual addressing called MEMS mirror, which has a faster responding speed around several nanosecond. Due to the limitation of technique and precision of the company we try to cooperate with, we haven't tried this solution. Then, we just move to the multi-channel AOM approach.

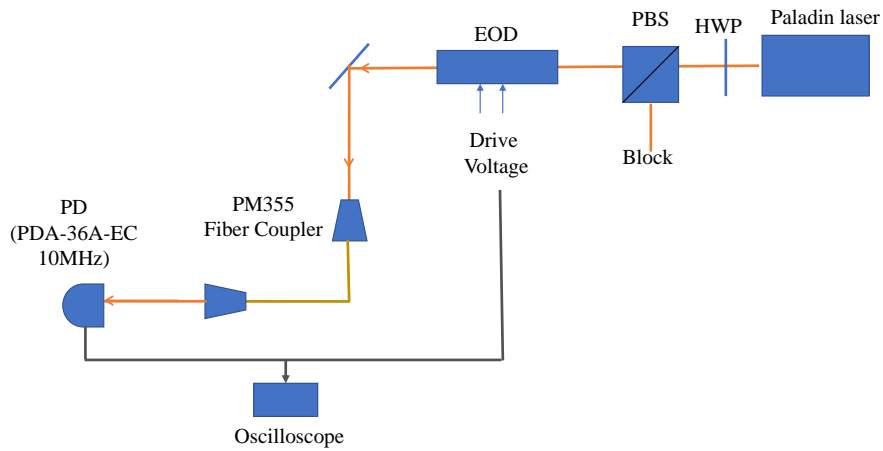


Figure 4.13 The optical path for testing the EOD responding speed.

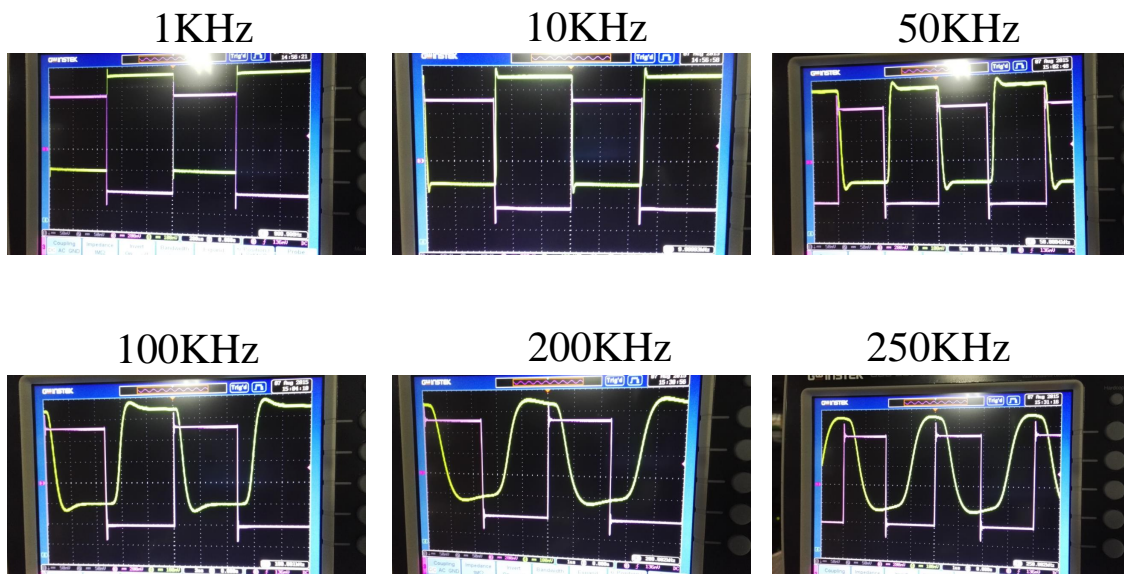


Figure 4.14 The EOD responding speed testing figure with oscilloscope.

#### 4.4.2 Multi-channel AOM approach

The schematic individual beam setup is shown in fig. 4.15. We use the DOE as a beam splitter to separate one beam to five beams. The separation angle is well matched with the five-channel AOM after a collimation lens. The aperture of each channel inside the AOM is around  $250\mu\text{m}$  and the separation between neighboring channels is  $900\mu\text{m}$ .

Each channel can be independently controlled by RF signal with frequency shift and switch on or off. Considering that our typical ions separation is  $5\mu\text{m}$ , the beam would be focused to around  $1.4\mu\text{m}$ . Actually, we cannot directly focus the  $250\mu\text{m}$  to  $5\mu\text{m}$ , because the calculated focal length of the objective lens is too small and the distance between the ion and the closest viewport is not short enough. So we use two-stage telescope system with four lens to expand the beam diameter from  $250\mu\text{m}$  to around  $12\text{mm}$ . Then an objective lens with working distance around  $35\text{mm}$  can easily focus the beam to  $1.4\mu\text{m}$ .

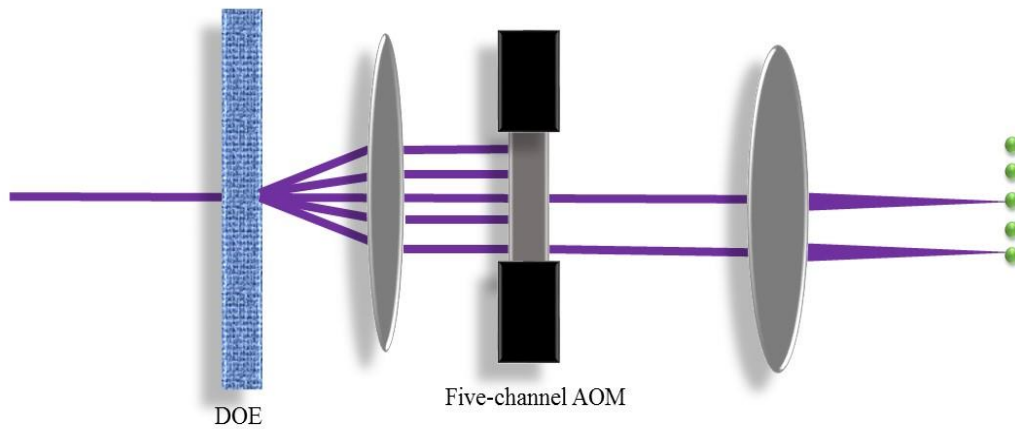


Figure 4.15 The schematic individual beam setup.

The two important parts in the system are the DOE and five-channel AOM. The DOE can determine the separation angle and power distribution through the fixed grating structure. The five-channel AOM can control each beam's intensity, frequency, and phase through RF field, which can be flexibly adjusted. The choice of the DOE type seems more important because it is unadjustable. After careful calculation, we decide to use the type MS-499-U-Y-X, whose separation angle is  $0.33\text{deg}$ .

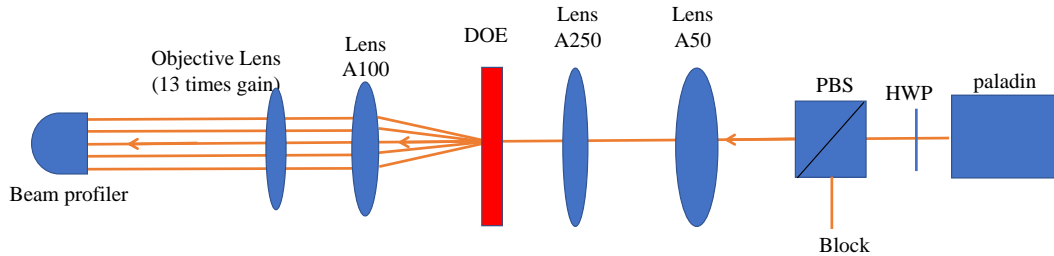


Figure 4.16 Setup for testing DOE.

The five beams should be uniformly spacing with equal intensity. We use the setup as shown in fig. 4.16, to test the output beam intensity and quality. The beam width of Paladin laser is around 0.8mm and we use lens A50 and lens A250 to expand it five times to around 4mm because the DOE works better with larger beam width. After the beam goes through DOE, we use a lens A100 to focus the beam to about  $11\mu\text{m}$ . As we discussed before, the beam profiler doesn't work well with such small beam point. We add another objective lens to expand it 13 times larger in front of beam profiler. The measured image picture is shown in fig. 4.17. The five beams are equally spaced with a little different intensity. Actually, we cannot trust intensity distribution of beam profiler due to its shaking and fluctuation problem. So, we change the setup by adding a pin-hole on the focal point and replace the beam profiler with PD, as shown in fig. 4.18.

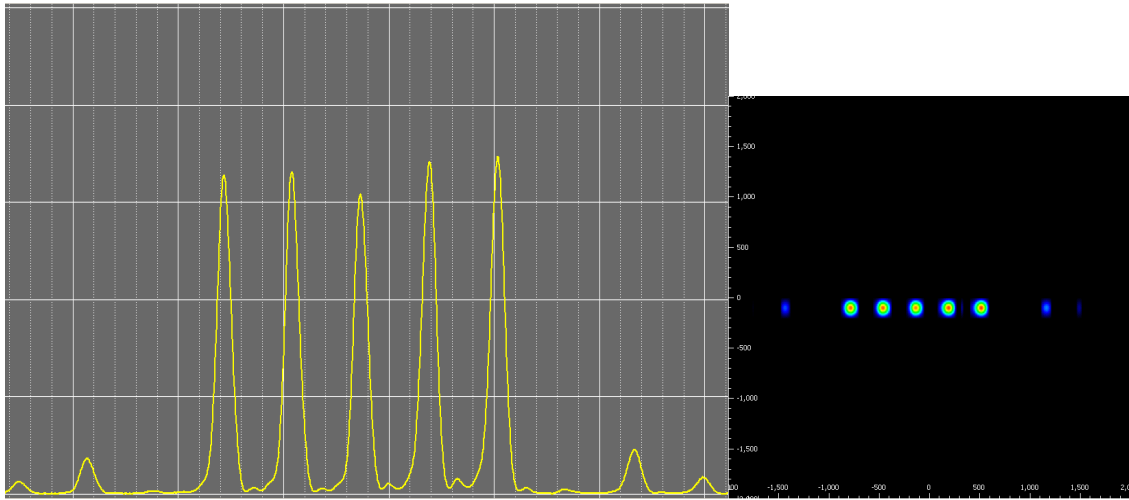


Figure 4.17 The measured image picture of five beams.

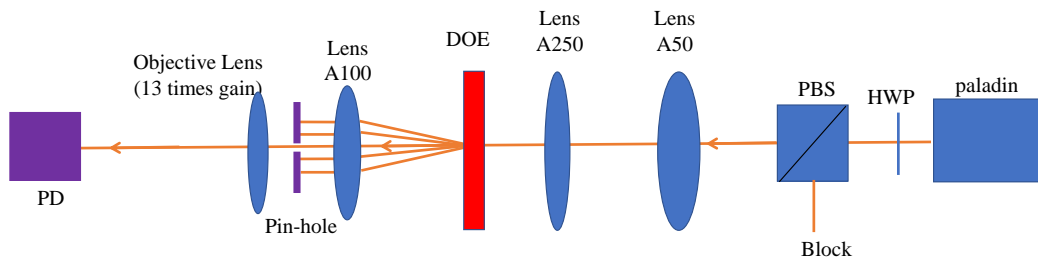


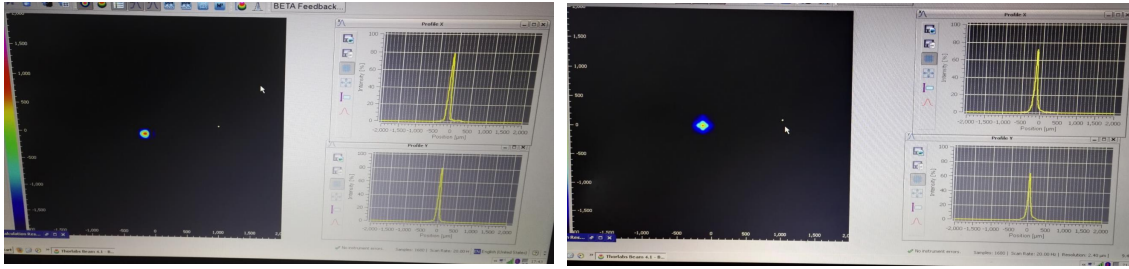
Figure 4.18 The setup to measure the intensity distribution of DOE output.

We use the pin-hole as a spatial filter to measure the beams' intensities one by one. The pin-hole's position is carefully adjusted and is right in the beam waist. We use the PD as a detector, which is very sensitive to the laser power. By shifting the pin-hole's position along the beam chain and recording the voltage of PD, we can get the precise uniformity. Considering the beam waist is around  $11\mu\text{m}$ , we use two types of pin-holes

with diameter  $10\mu\text{m}$  and  $15\mu\text{m}$  to double check it. In order to make sure the output of pin-hole just contains one beam, we can optimize the pin-hole's position to maximize the output power with powermeter and also check the image picture on the beam profiler. The results are shown in fig. 4.19.

10um pin-hole

15um pin-hole



Beam Number	1	2	3	4	5
Voltage/V	1.296	1.426	1.296	1.426	1.296
Relative Intensity	90.8%	100%	90.8%	100%	90.8%

Beam Number	1	2	3	4	5
Voltage/V	1.716	1.856	1.716	1.846	1.700
Relative Intensity	92.5%	100%	92.5%	99.4%	91.5%

Figure 4.19 The intensity distribution through pin-hole measurement.

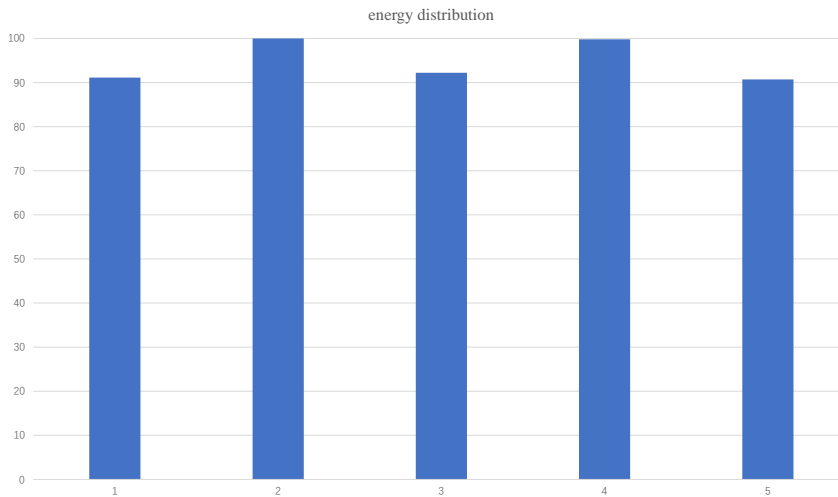


Figure 4.20 The energy distribution histogram.

The two results are consistent with each other. We average them and get the estimated



energy distribution histogram, as shown in fig. 4.20. The measured uniformity with the five beams is less than 10%, which can be compensated by the next five-channel AOM through tuning the intensity of RF field. When building the whole individual beam setup, we also optimize the combination of the lens group with different types and focal length to minimize the imaging aberration. Finally, we use the EMCCD to check the beam image quality precisely, as shown in fig. 4.21. There is still coma aberration around the beam spots. By the way, the individual beams and the fluorescence from ions can be collected through the same EMCCD, which make it easier to align the individual beams to the ions.

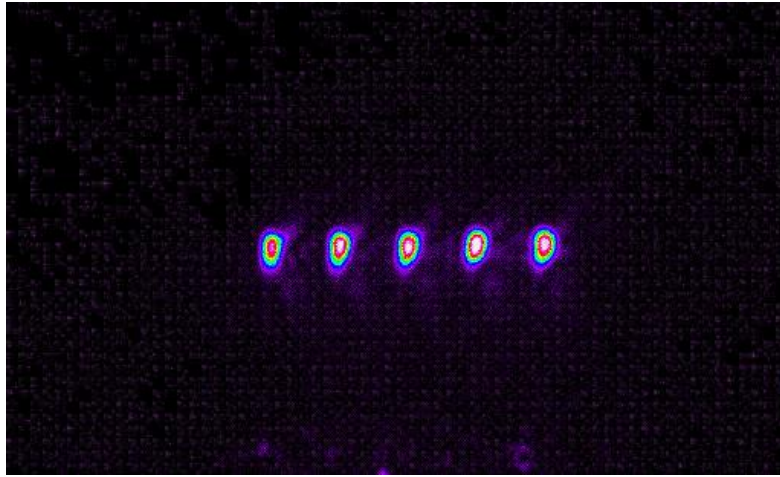


Figure 4.21 The individual beams imaging on the EMCCD.

## Chapter 5 Global quantum entanglement

### 5.1 Overview of global gate

Nowadays, people are exploring various implementations of quantum algorithm, such as the factorization of a large number<sup>[57]</sup>, variational quantum eigensolver<sup>[5,58]</sup>, Shor algorithm<sup>[57,59]</sup> and the simulation of quantum many-body systems<sup>[1,60-61]</sup>. It is confirmed that these universal quantum algorithms can be decomposed into a combination of single-qubit gates and two-qubit entanglement-gates<sup>[62]</sup>, thereby realizing the possibility of building universal quantum computers and simulators. It is worth mentioning that this intuitive and general decomposition may not be efficient<sup>[63-65]</sup>. There is research having shown that global quantum entangling gates can simplify this decomposition and accelerate quantum circuits implementation<sup>[66-69]</sup>. The global quantum gate is an extension of the two-qubit MS gate and still using phonons as a "bus"<sup>[70-72]</sup>.

In ion-trap system, all the ions are fully connected via Coulomb interactions<sup>[73-75]</sup>. According to the direction of motion, phonon modes can be divided into the axial and two transverse modes, which all can be used to generate the qubit entanglement. By adjusting the angle between the laser vector direction and the phonon modes, a certain motion direction can be mainly coupled to ignore the other modes. Even so, as the number of ions increases, the number of motional modes, such as the X transverse motion, still contains the same number of phonon modes to the number of ions. When we apply the laser to manipulate ions, these phonon modes in X direction can all be coupled with qubits in the phase space.

There are two schemes to realize the global entangling gate. One is to mainly use one single phonon mode to minimize the involving of the other modes. Incomplete decoupling of the rest modes will lead to a reduction of gate fidelity. The phonon mode in the axial direction is relatively easier to realize the decoupling due to the relatively larger separation among phonon modes than that of transverse modes. The global entangling gates have been realized by only coupling to the axial center-of-mass (COM) mode<sup>[24,76-77]</sup>, which is difficult to scale up because the mode separation becomes smaller as the number of ions increases<sup>[24,78-79]</sup>. The other way is using all the laser-coupled phonon modes<sup>[78-82]</sup>, which has been implemented in experiment with two qubits<sup>[82-84]</sup>. Here, we studied the N-qubit global gate with this scalable way. Through precisely controlling all the trajectories

of the modes in phase space, the qubits can be decoupled with all the phonon modes and obtain the desired geometric phase after the gate time.

The general implementation of the global entangling gate can be represented in YY interaction as

$$U_G(\chi) = \exp[-i\chi \sum_{j < j'}^N \sigma_{j,y} \sigma_{j',y}], \quad (5-1)$$

where  $\chi$  is the coupling strength of all the two-body terms. In general, by controlling the geometric phase to achieve the global gate as  $U_G[\pi/4]$ , we can prepare the N-qubit GHZ state<sup>[85]</sup>. Next, I will discuss the experimental implementation with single-mode and multi-mode approach.

## 5.2 Single-mode approach

### 5.2.1 Scheme

The single-mode approach is similar with the two-qubit MS gate method, which can be realized through the global detuned blue and red sideband transition on all the qubits. We can write down the Hamiltonian as

$$\begin{aligned} H_{sm} &= \sum_{j=1}^N i \frac{\hbar\Omega}{2} \eta (\sigma_{j,+} a^\dagger e^{-i\Delta t} - \sigma_{j,-} a e^{i\Delta t}) + H.c. \\ &= \sum_{j=1}^N \frac{\hbar\Omega}{2} \eta \sigma_{j,y} (a^\dagger e^{-i\Delta t} + a e^{i\Delta t}), \end{aligned} \quad (5-2)$$

where  $j$  is the ion index, and  $\Delta = \omega - \omega_m$  is the laser detuning from the ions' motional mode. In this case, we don't need the individual addressing system to operate each qubit independently. Here, we have the N spin terms  $\sum_{j=1}^N \sigma_{j,y}$  and just one motional terms  $(a^\dagger e^{-i\delta t} + a e^{i\delta t})$  by ignoring the effect of other modes. After time  $T = 1/\Delta$ , the motional mode and the qubit state will be decoupled and generate the N-qubit entanglement.

In experiment, we build a fully-controlled multi-qubit system by confining a  $^{171}\text{Yb}^+$  ion chain. The global beam and individual beams are shown in fig. 5.1. These two beams have a  $90^\circ$  angle and can mainly drive the modes in x-direction.

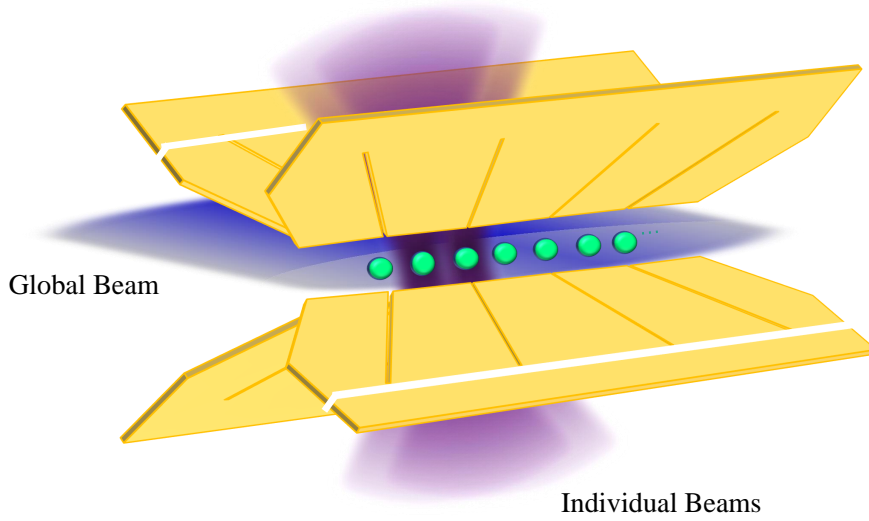


Figure 5.1 The experiment setup.

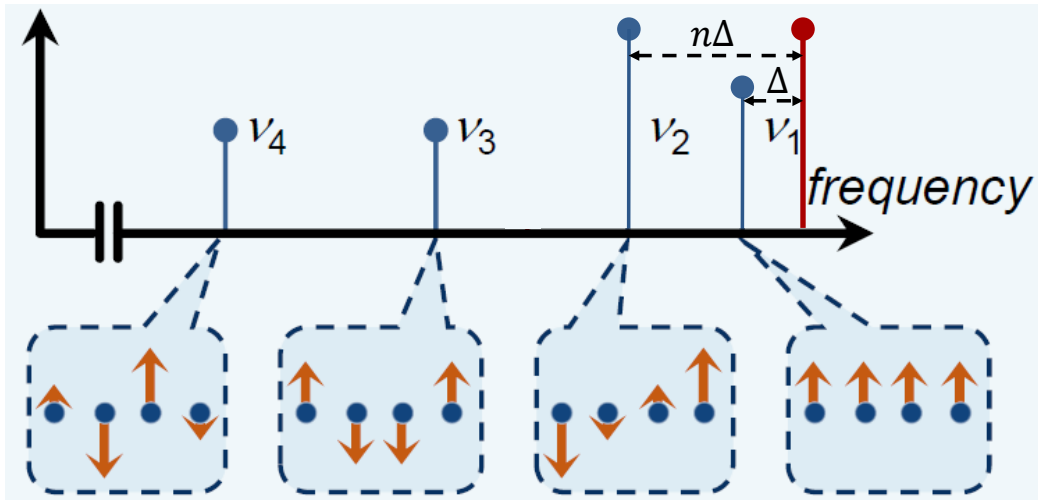


Figure 5.2 The effective Raman laser detuning for single-mode approach.

For the transverse mode in the x-direction, the maximum frequency belongs to the COM mode, which has the uniform Lamb-Dick parameter for all the ions and is used as the motional "bus". In order to minimize the effect of the rest mode, we set the laser detuning a little bit larger than the frequency of COM mode, and the separation between laser detuning and the neighboring mode is  $n$  times larger than that with COM mode,

as shown in fig. 5.2 for four-ion case as example. For the single-mode approach, the neighboring mode next to COM mode affects the gate fidelity most. With the setting above, when trajectory of COM mode in the phase space is closed after one round, the trajectory of the neighboring mode will also be closed after  $n$  rounds, which can realize the decoupling with the spin qubits.

### 5.2.2 Three-qubit GHZ state test

We first test our scheme with three ions. The transverse mode frequencies in  $x$ -direction is  $\{\nu_1, \nu_2, \nu_3\} = 2\pi \times \{2.184, 2.127, 2.004\}$  MHz. We set the detuning a little bit larger than the COM mode as  $2\pi \times 2.198$  MHz. The separation between the detuning and the frequency of the second mode is around 5 times larger than that with COM mode. The total gate time is around  $70\mu\text{s}$ .

The time evolution of three-qubit entangling gate and the parity oscillation are shown in fig. 5.3. In order to create the GHZ state for three-qubit, another global pulse with  $\pi/2$  rotation in  $x$  axis should be applied. We measured the population fidelity(87.79%) and parity fidelity(72.33%), and get the three-qubit GHZ entanglement fidelity with 80.06%.

In addition, we realize the two-qubit entangling gate within the three-ion chain by shining lasers just on the related ions. The result of YY gate between ion 1 and ion 2 is shown in fig. 5.4. The population fidelity is 96.99% and parity fidelity is 91.88%. And two-qubit GHZ entanglement fidelity is 94.44%. We also measure the other subset in the chain. The parity oscillation is shown in fig. 5.5. The entanglement fidelity is 94.89% for ion 1 and ion 3, and 92.13% for ion 2 and ion 3.

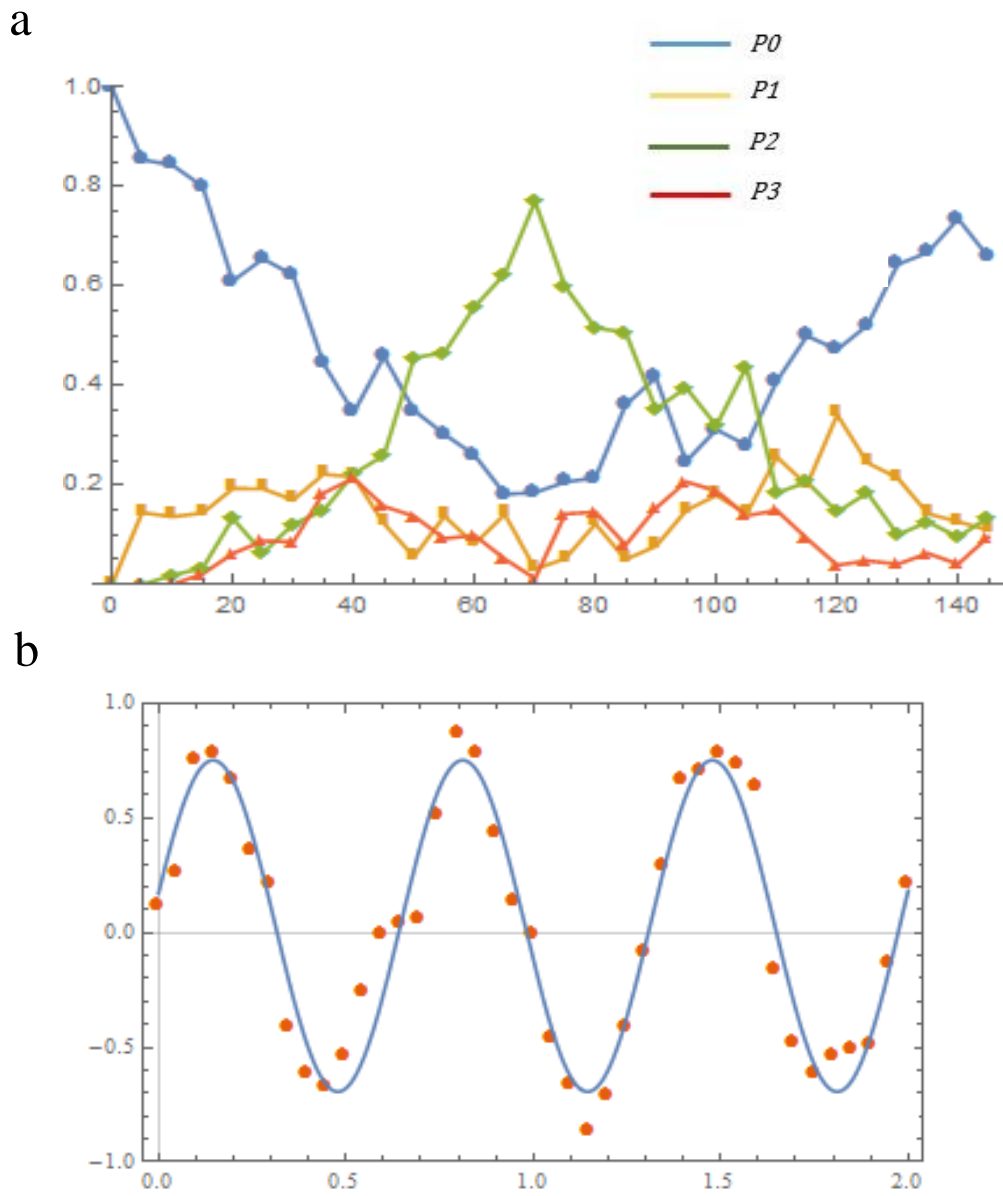


Figure 5.3 The time evolution of three-qubit entangling gate and the parity oscillation.

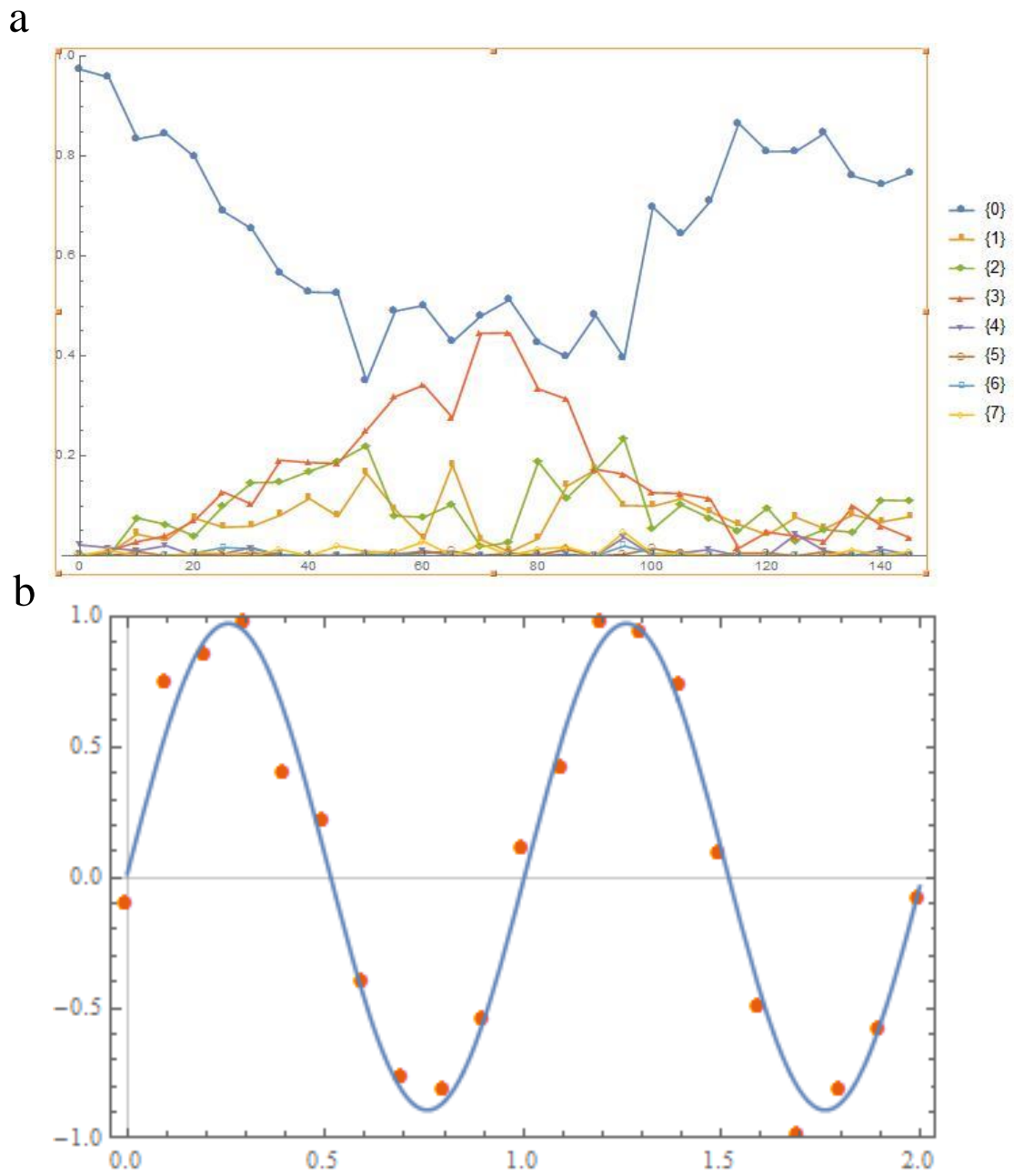


Figure 5.4 The time evolution of two-qubit (ion 1 and ion 2) entangling gate and the parity oscillation within three-ion chain.

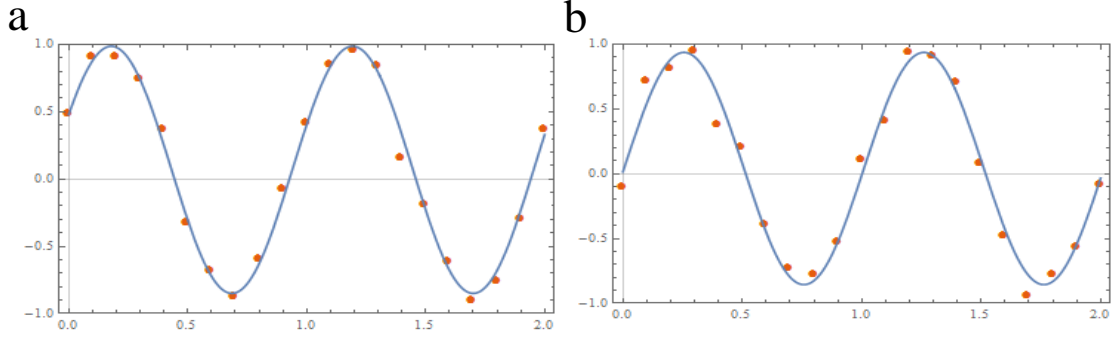


Figure 5.5 The parity oscillation of two qubit entanglement (ion 1 and ion 3)(ion 2 and ion 3).

## 5.3 Multi-mode approach

### 5.3.1 Scheme

The Hamiltonian for the multi-mode approach can be written as

$$\begin{aligned}
 H_{mm} &= \sum_{j=1}^N \sum_{k=1}^N i \frac{\hbar \Omega_j(t)}{2} \eta_{j,k} (\sigma_{j,+} a_k^\dagger e^{-i\delta t} e^{i\phi_j(t)} - \sigma_{j,-} a_k e^{i\delta t} e^{-i\phi_j(t)}) + H.c. \\
 &= \sum_{j=1}^N \sum_{k=1}^N \frac{\hbar \Omega_j(t)}{2} \eta_{j,k} \sigma_{j,y} (a_k^\dagger e^{-i\delta t} e^{i\phi_j(t)} + a_k e^{i\delta t} e^{-i\phi_j(t)}),
 \end{aligned} \tag{5-3}$$

where  $j$  is the ion index,  $k$  is the mode index and  $\delta = \omega - \omega_0$  is the laser detuning from the ion energy gap. The time evolution term can be written as

$$U(t) = \exp\left[\sum_{j,k} \beta_{j,k}(t) \sigma_{j,k} - i \sum_{j < j'} \theta_{j,j'}(t) \sigma_{j,y} \sigma_{j',y}\right], \tag{5-4}$$

where  $\beta_{j,k}(t) = \alpha_{j,k}(t) a_k^\dagger - \alpha_{j,k}^*(t) a_k$ , is the displacement term, and  $\theta_{j,j'}(t)$  is the coupling strength as

$$\begin{aligned}
 \theta_{j,j'}(t) &= - \sum_k \int_0^t dt_1 \int_0^{t_1} dt_2 \frac{\eta_{j,k} \eta_{j',k} \Omega_j(t_2) \Omega_{j'}(t_1)}{2} \\
 &\quad \sin\{(\omega_k - \delta)(t_2 - t_1) - [\phi_j(t_2) - \phi_{j'}(t_1)]\}.
 \end{aligned} \tag{5-5}$$

Our goal is to make all the trajectories of motional modes closed and get the coupling strength we want after the gate time  $T$ , which can be written as

$$\alpha_{j,k}(T) = 0, \tag{5-6}$$



$$\theta_{j,k}(T) = \chi. \quad (5-7)$$

We can control the amplitude and phase of the Raman laser to meet the requirements. In experiment, the total gate time is divided into several segments( $K$ ) with same duration, which gives us  $N \times K$  parameters to control. We decide to use phase modulation to construct an optimization problem. By minimizing the objective function  $\sum_{j,k} |\alpha_{j,k}(T)|^2$  with the coupling strength constraint<sup>[82,86-87]</sup>, we can get the feasible pulse scheme to realize the perfect global gate through classical calculation. The detailed calculation process and the comparison between intensity modulation and phase modulation are discussed in the previous thesis of my colleague(Yao Lu<sup>[88]</sup>)

### 5.3.2 Three- and four-qubit GHZ state results

For three-qubit case, the transverse mode frequencies in x-direction is  $\{\nu_1, \nu_2, \nu_3\} = 2\pi \times \{2.184, 2.127, 2.004\}$  MHz. We set the detuning  $\delta$  between the last two modes to be  $2\pi \times 2.094$  MHz. By fixing the gate time to  $80\mu\text{s}$  and dividing the pulse to 6 segments, we calculate the experimental implementation of a global three-qubit entangling gate, as shown in fig. 5.6.

In experiment, we apply the pulse scheme and prepare the three-qubit GHZ state and measure the population distribution and parity oscillation<sup>[89]</sup>, as shown in fig. 5.7. The state fidelity is  $(95.2 \pm 1.5)\%$ . And by controlling the individual beams on or off, we prepare the two-qubit GHZ state within the three-ion chain with fidelities  $(96.7 \pm 1.8)\%$  for {ion 2, ion 3},  $(97.1 \pm 1.9)\%$  for {ion 1, ion 3}, and  $(96.5 \pm 1.5)\%$  for {ion 2, ion 3}.

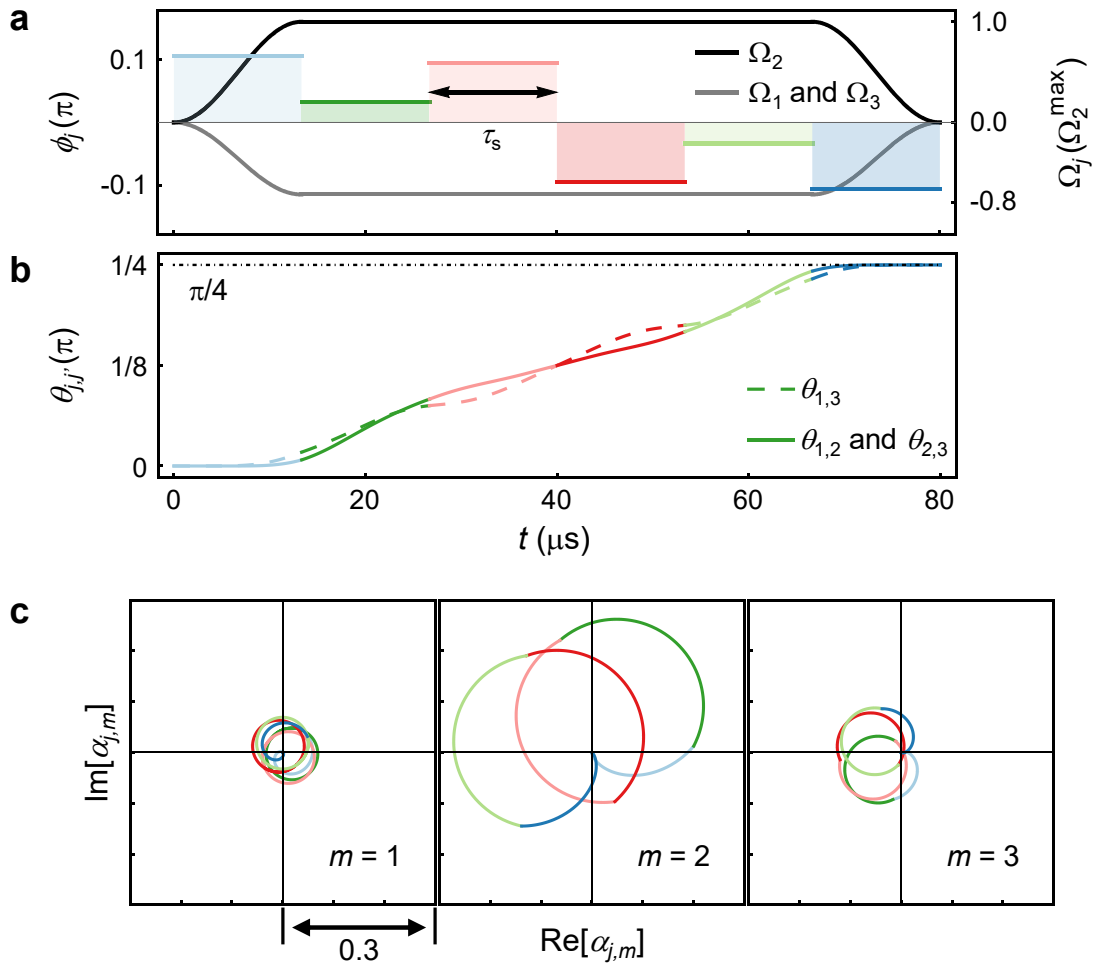


Figure 5.6 Experimental implementation of a global three-qubit entangling gate.

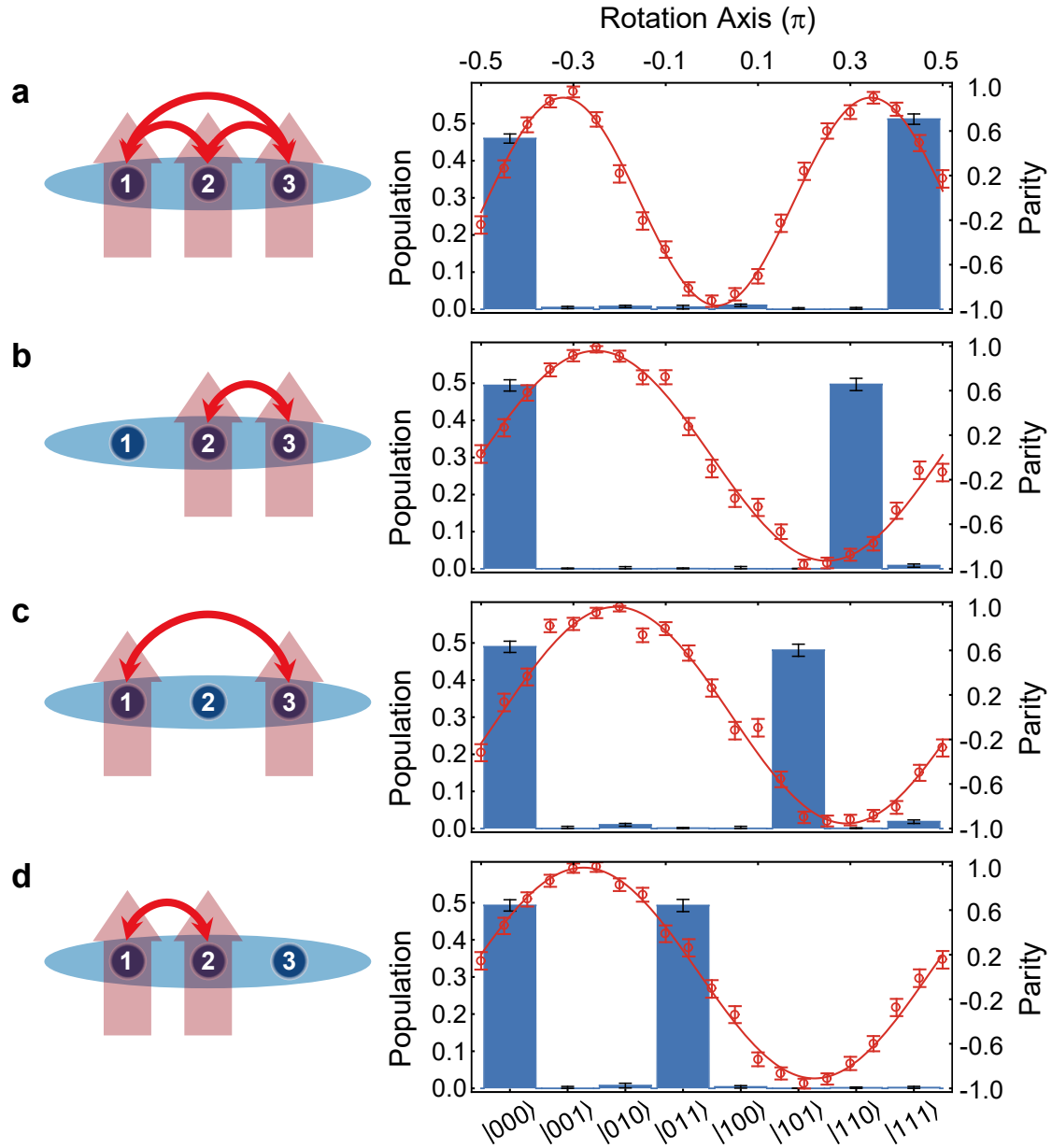


Figure 5.7 The GHZ state of the global entangling gates in three-ion chain.

For four-qubit case, the transverse mode frequencies in x-direction is  $\{v_1, v_2, v_3, v_4\} = 2\pi \times \{2.186, 2.147, 2.091, 2.020\}$  MHz. We set the detuning  $\delta$  between the middle two modes to be  $2\pi \times 2.104$  MHz. By fixing the gate time to  $120\mu\text{s}$  and dividing the pulse to 12 segments, we calculate the experimental implementation of a global three-qubit entangling gate, as shown in fig. 5.8 and fig. 5.9.

In experiment, we apply the pulse scheme and prepare the four-qubit GHZ state, as shown in fig. 5.10. The state fidelity is  $(93.4 \pm 2.0)\%$ . And by controlling the individual beams on or off, we prepare the three and two-qubit GHZ state within the four-ion chain

with fidelities  $(94.2 \pm 1.8)\%$  for {ion 2, ion 3, ion 4}, and  $(95.1 \pm 1.8)\%$  for {ion 1, ion 3}.

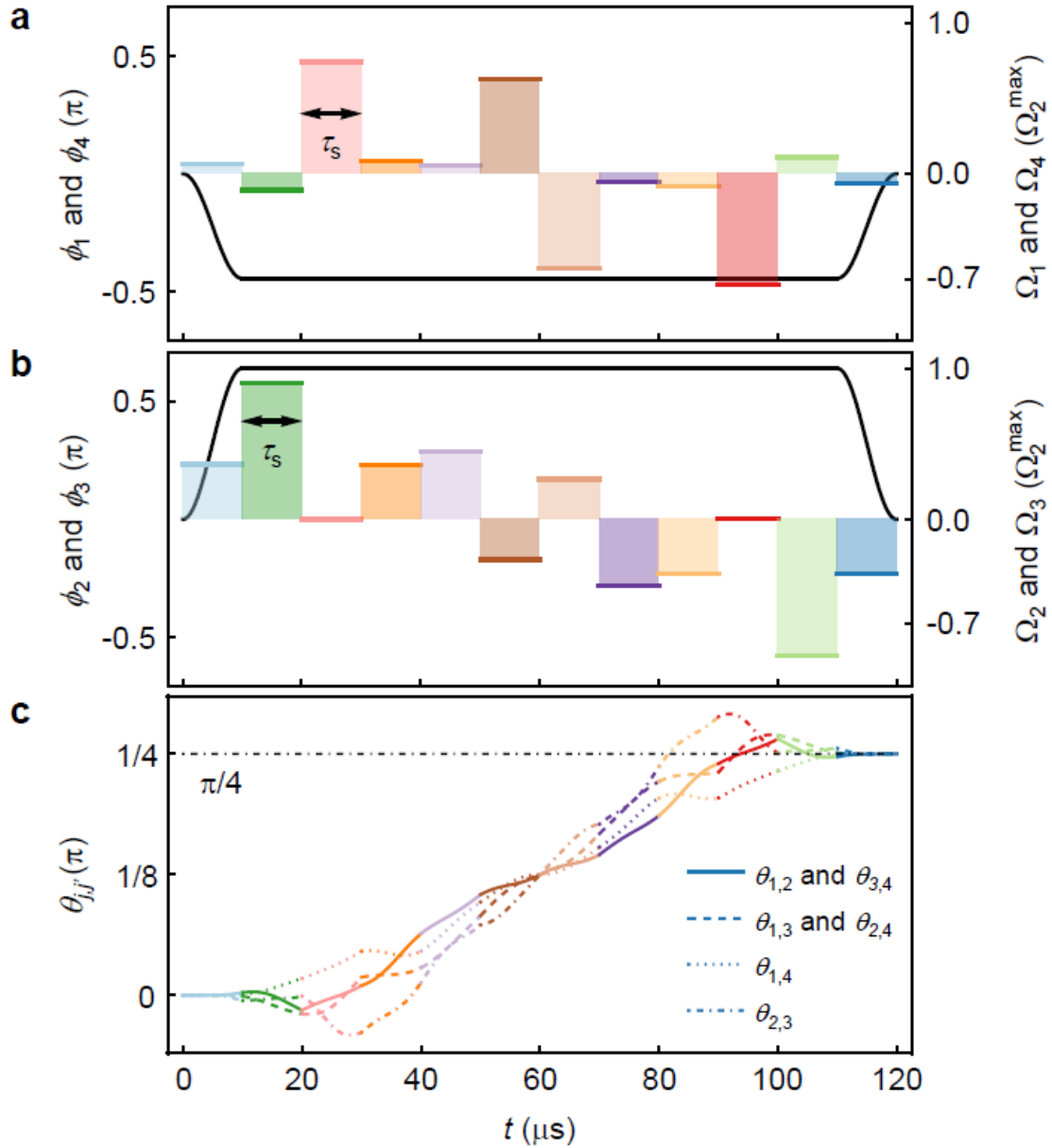


Figure 5.8 Experimental implementation of a global three-qubit entangling gate.

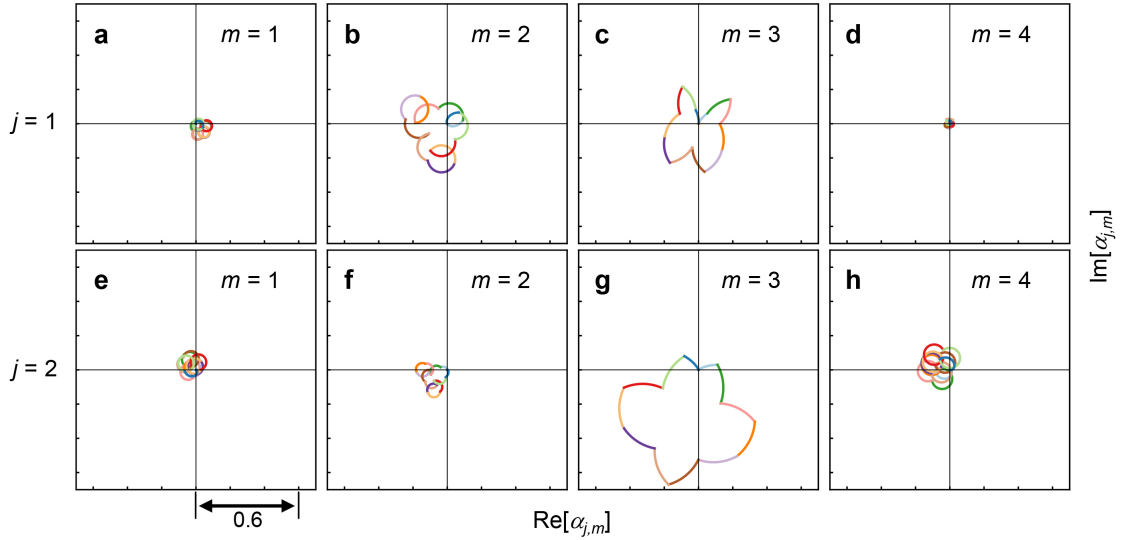


Figure 5.9 The trajectory of motional modes.

## 5.4 Discussion

By numerically calculating the prepared GHZ fidelity, we compared the single-mode and multi-mode approaches, as shown in fig. 5.11. As the number of qubits increases, for the multi-mode approach, the GHZ state fidelity can be always 1 in principle and the gate duration increases near linearly. However, for the single-mode approach, due to the residual coupling between the qubit state and the motional mode, the GHZ state fidelity cannot be 100% and keeps dropping a lot with the increasing number of qubits. One way to achieve a higher fidelity is increasing the gate duration, but the improvement may not be very significant.

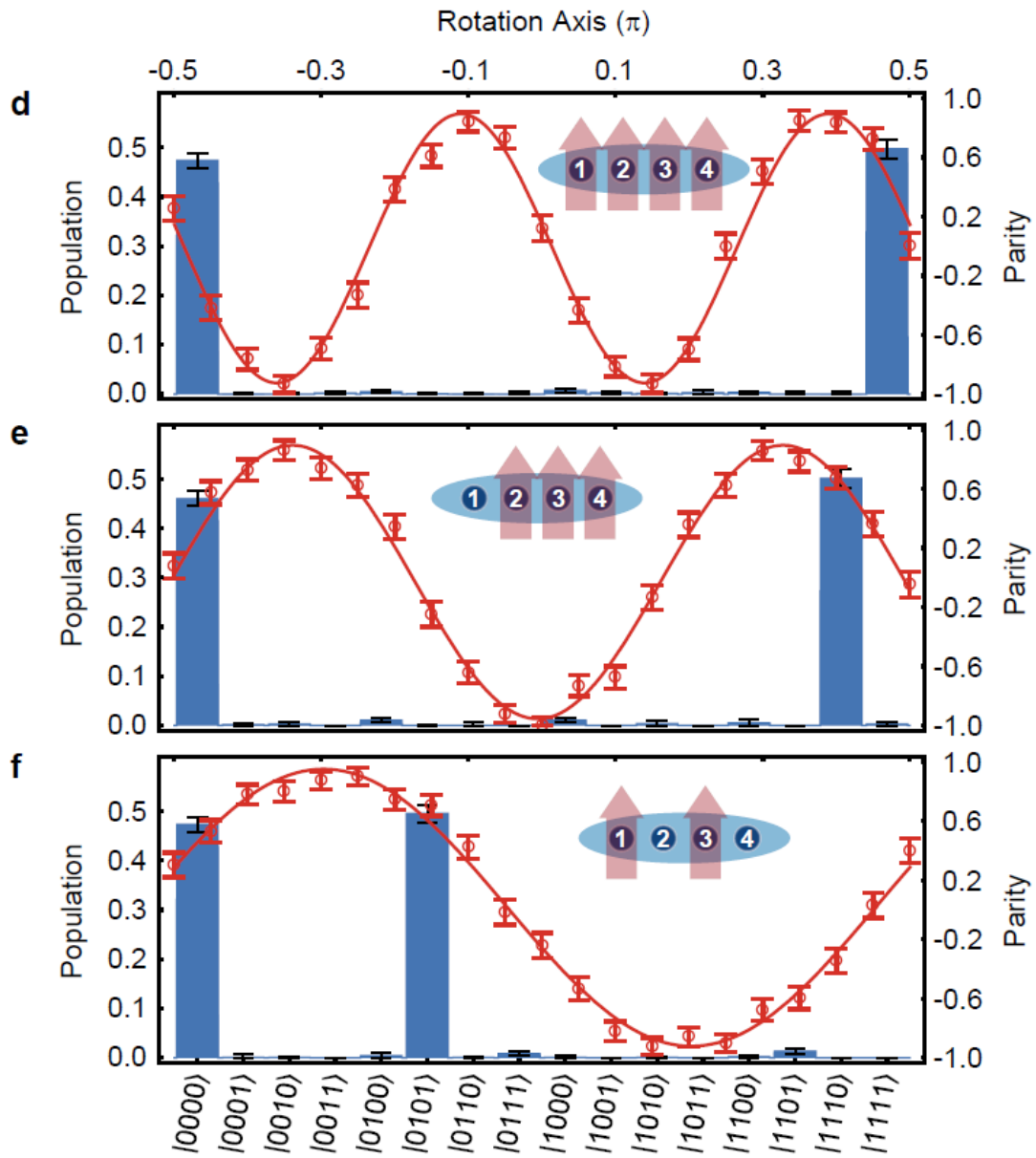


Figure 5.10 The GHZ state of the global entanglement-gates in four-ion chain.

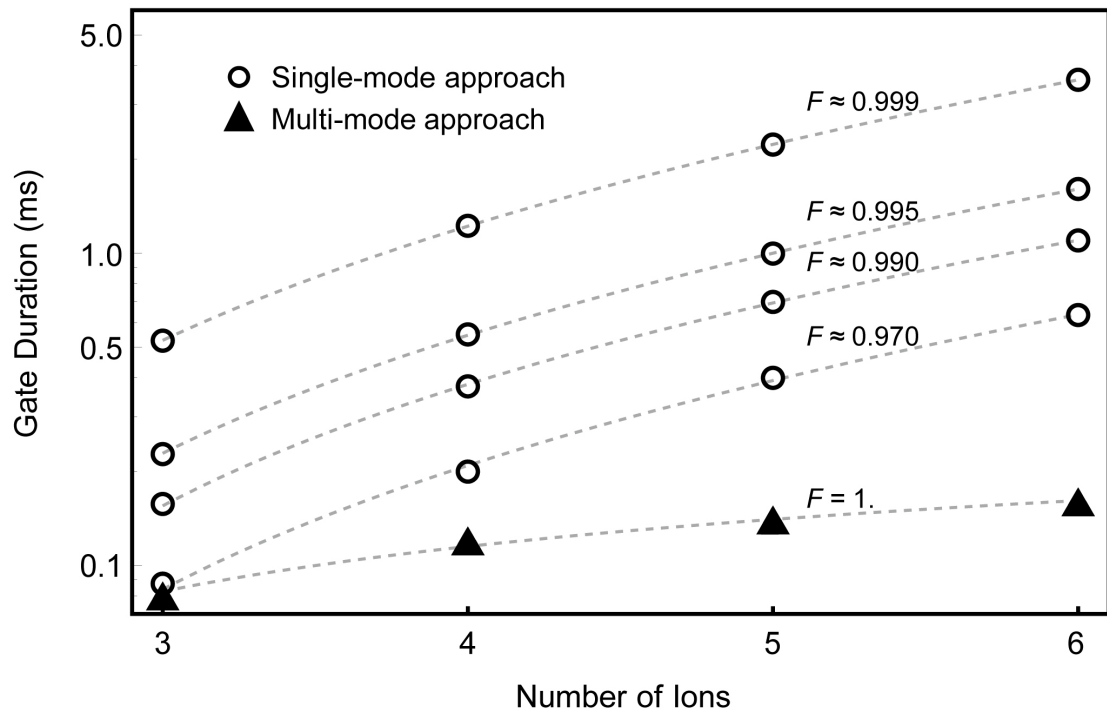


Figure 5.11 Comparison between gate durations of single- and multi-mode approaches.

## Chapter 6 Quantum error mitigation

### 6.1 Paradigm of error-mitigated quantum computation

The paradigm of error-mitigated quantum computation is shown in Fig. 6.1. The noisy quantum device is treated as a multi-qubit black box in Fig. 6.1a, capable of preparing each qubit into an initial state  $\rho_0$ , performing a set of single-qubit and two-qubit gates and two-outcome measurement on each qubit, which is described by a positive operator-valued measure (POVM)  $\mathcal{M} \equiv \{E_0, I - E_0\}$  with  $I$  being the  $2 \times 2$  identity operator. These quantum operations are generally not accurate because of errors from operational imperfections and environmental fluctuations. As proposed in Ref.<sup>[18]</sup>, we perform the gate set tomography<sup>[90-92]</sup> and characterize state preparation and measurement (SPAM) and gates of noisy quantum devices by Gram matrices and Pauli transfer matrices (PTMs), respectively<sup>[92]</sup> as shown in Fig. 6.1b. When we repeatedly execute a quantum circuit with such a noisy device aiming at obtaining the expectation values of observables of interest, the estimation will be deviated from the ideal case due to the imperfection of the quantum device, as shown in Fig. 6.1c. The correction of each noisy quantum operation can be decomposed to the combination of experimental basis operations (which we give later) with quasi-probabilities as shown in Fig. 6.1d. Since some of the quasi-probabilities can be negative, we cannot physical implement the decomposition. However, the expectation of the decomposition can be estimated by sampling circuits with random basis operations according to the quasi-probabilities<sup>[17-18]</sup>. After running the random circuits with the corrections, the probability distribution of the output expectation value is shifted towards the ideal value at a cost of enlarged variance due to the presence of negative values in the quasi-probabilities<sup>[18]</sup>, as shown in Fig. 6.1c. The variance can be reduced by increasing the repetition number, which is the number of random-circuit instances.



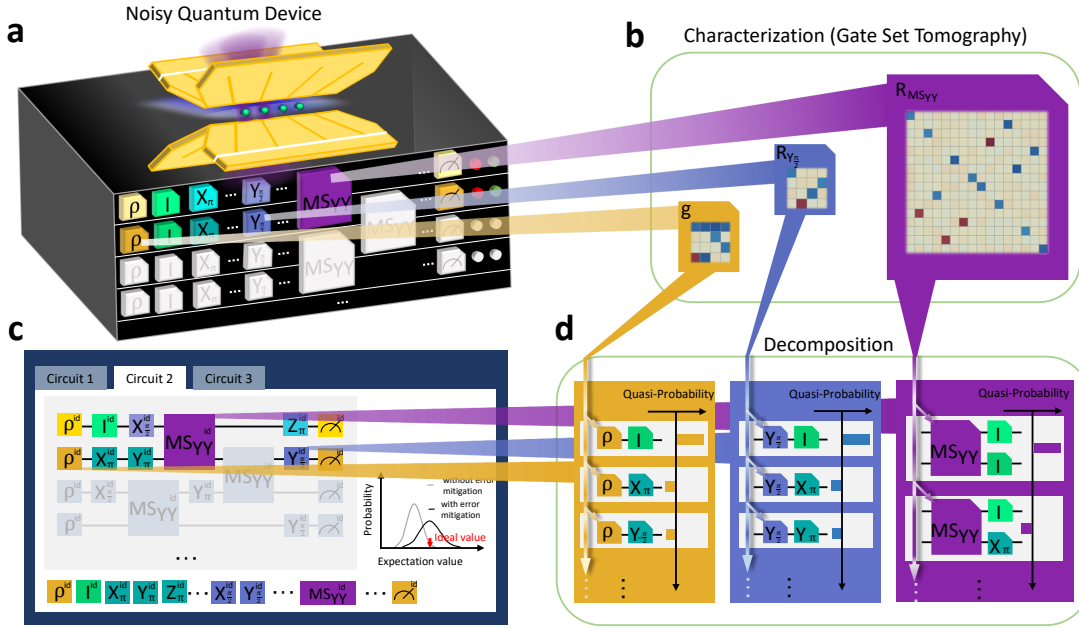


**Figure 6.1 Paradigm of error-mitigated quantum computation.** **a.** Quantum black box based on a trapped  $^{171}\text{Yb}^+$ -ion system. Each button on the surface corresponds to an operation exerted on the quantum system encapsulated, where the buttons with  $\rho$  and  $M$  are for initial-state preparation and computational-basis measurement, whose results are indicated by the lights. The other buttons are for single-qubit and two-qubit quantum operations on certain qubits. The operations are implemented by global (blue) and individual (purple) laser beams illuminating the ion qubits. **b.** Characterization of the quantum black box. The error-affected state preparation and measurement is characterized by the Gram matrix  $g$ , and the effect of each operation  $G$ , like  $Y_{\frac{\pi}{2}}$  and  $MS_{YY}$ , is described by a Pauli transfer matrix  $R_G$  in the superoperator formalism, which is obtained by gate set tomography. **c.** Construction of unbiased estimator of an expectation value specified by a quantum circuit, with building blocks including initial state preparation, different single-qubit and two-qubit gates, and final measurement. With error-mitigation, the distribution of the output expectation value is shifted towards the ideal value at a cost of enlarged variance. **d.** Quasi-probability decomposition for the ideal initial state and exemplary single-qubit and two-qubit gates. Since the errors in state preparation and those in measurement are indistinguishable, we ascribe both of the errors to state preparation and decompose the ideal initial state with a set of experimental basis states, prepared by state initialization followed by a random fiducial gate. The PTM of an ideal quantum gate can be expanded as a quasi-probability distribution over random gate sequences consisting of the experimental gate and one of the experimental basis operations, Pauli operations in the experiment. The error-mitigated estimation of the expectation value is then obtained by the Monte-Carlo method(which we show later).

Here, we provide an illustrative example of applying the probabilistic error cancellation technique to a simple quantum circuit, Suppose an experimenter plans to apply an ideal gate  $G^{id} \equiv [e^{-iY\frac{\pi}{4}}]$  on an ideal initial state  $\rho^{id} \equiv |0\rangle\langle 0|$ , and get the ideal expectation value of observable  $\langle X \rangle^{id} \equiv \text{Tr}[XG^{id}(\rho^{id})] = 1$ . However, as a example of a noisy quantum device, the actual initial state could be  $\rho = 90\% |0\rangle\langle 0| + 10\% \frac{I}{2}$ ,

and the actual gate could be  $G = 80\%G^{id} + 20\%D$ , where  $D(\rho) = \frac{I}{2}$ . Then, the actual result is  $\langle X \rangle = Tr[XG(\rho)] = 72\%$ . With the error-cancellation procedure, the ideal initial state is decomposed as  $\rho^{id} = (\rho - 10\%\frac{I}{2})/90\%$ , and the ideal gate is decomposed as  $G^{id} = (G - 20\%D)/80\%$ . Then, the ideal expectation value can be obtained by  $\langle X \rangle^{id} = Tr[XG(\rho)] \times (1/72\%) - Tr[XG(\frac{I}{2})] \times (10\%/72\%) - Tr[XD(\rho)] \times (20\%/72\%) - Tr[XD(\frac{I}{2})] \times (2\%/72\%)$ , where the four terms can be obtained by running the noisy quantum device. By computing each term on the noisy quantum device and substituting results into the formula, we can obtain the ideal expectation value.

For a computation with multiple gates, the state preparation, measurement and each gate can be treated in a similar way. Then, the formula of the ideal expectation value, i.e. a weighted summation of noisy computations has exponential terms with respect to the gate number. Therefore, instead of evaluating each term, we compute the summation using the Monte-Carlo method.

In this example, we consider the depolarizing error model. The decomposition can be applied to general error models without correlations. The decomposition formula is obtained by inverting the noise. For the gate  $G$ , the noise is  $N = 80\%[I] + 20\%D$ , and  $G = NG^{id}$ . The inverse of the noise is  $N^{-1} = ([I] - 20\%D)/80\%$ . Then, the ideal gate  $G^{id} = N^{-1}G = (G - 20\%D)/80\%$ .

## 6.2 Experimental realization

In our experimental realization, the quantum hardware encapsulated in the black box is a trapped-ion system, where  $^{171}Yb^+$  ions are trapped into a linear crystal and individually manipulated by global and individual laser beams, as shown in Fig. 6.1a. To encode quantum information, a pair of clock states in the ground-state manifold  $^2S_{1/2}$ , i.e.  $|F = 0, m_F = 0\rangle$  and  $|F = 1, m_F = 0\rangle$ , are denoted as the computational basis  $\{|0\rangle, |1\rangle\}$  of a qubit. At the beginning of executing a quantum circuit, each ion qubit is initialized to  $|0\rangle$  by optical pumping. We implement single-qubit operations by Raman laser beams with beatnote frequency about the hyperfine splitting  $\omega_0 = 2\pi \times 12.642821 \text{ GHz}$ . And the two-qubit operation, i.e. the Mølmer-Sørensen  $YY$ -gate ( $MS_{YY}$ ) is realized by driving transverse motional modes<sup>[71,73]</sup>, with frequencies in the  $x$ -direction  $\{\nu_1, \nu_2\} = \{1.954, 2.048\}$  MHz. We apply amplitude-shaped<sup>[93]</sup> bichromatic Raman beams with beatnote frequencies  $\omega_0 \pm \mu$ , where  $\mu$  is set to be the middle frequency of the two motional modes, and achieve the  $MS_{YY}$  gate for  $25 \mu\text{s}$ . We also realize the Mølmer-Sørensen  $ZZ$ -gate

( $MS_{ZZ}$ ) by adding single-qubit rotations before and after the  $MS_{YY}$  gate<sup>[94]</sup>(see Supplementary Fig. 4b). At the end of the execution, internal states of qubits are measured by state-dependent fluorescence detection<sup>[95]</sup>. Note that to collect fluorescence photons, we use a photomultiplier tube (PMT) in the single-qubit case and an electron-multiplying charge-coupled device (EMCCD) in the two-qubit case.

## 6.3 Characterization of noisy quantum gates

### 6.3.1 PTM representation

We introduce the PTM representation for the mathematical description of an  $n$ -qubit noisy quantum device, where density operators  $\rho$  and physical observable  $E$  are represented by  $2^n$ -entry column vectors  $|\rho\rangle\rangle$  and row vectors  $\langle\langle E|$ , and quantum gates  $G$  are represented by  $2^{2n} \times 2^{2n}$  PTMs  $R_G$ . Here, the expectation value of the observable  $\hat{E}$  after operating  $G_s$  on the initial state  $\hat{\rho}$  is represented by  $\langle\langle E|R_G|\rho\rangle\rangle$ . PTMs can be determined by gate set tomography, which requires informationally complete data obtained from experiments with initial states from a basis set  $S_n \equiv \{|0\rangle, |1\rangle, |1\rangle_X, |1\rangle_Y\}^{\otimes n}$  and measurement of the observables from the  $n$ -qubit Pauli basis  $\mathcal{P}_n = \{I, X, Y, Z\}^{\otimes n}$ , where  $|1\rangle_X$  and  $|1\rangle_Y$  are the eigenstates of Pauli operators  $X$  and  $Y$ . Compared to quantum process tomography, gate set tomography is featured by appropriately taking consideration of SPAM errors, which is of great importance in quantum computations with high accuracy. In gate set tomography, the states in  $S_n$  and the measurement of observables in  $\mathcal{P}_n$  are realized by using a set of fiducial gates  $\mathcal{F}_n \equiv \left\{ I, X_{\pi}, Y_{-\frac{\pi}{2}}, X_{\frac{\pi}{2}} \right\}^{\otimes n}$  consisting of the identity operation and the  $X$  or  $Y$  axis rotations on each qubit, which are to be characterized together with the rest of the quantum operations. The single-qubit SPAM errors are reflected in the Gram matrix<sup>[92]</sup>, as shown in Fig. 6.2, which is obtained by preparing the qubit in one of the states  $S_1$ ,  $|\rho_i\rangle\rangle = R_{F_i}|\rho_0\rangle\rangle$ , and measuring the expectation values of the operators in the single-qubit Pauli basis  $\mathcal{P}_1$ ,  $\langle\langle E_i| = \langle\langle E_0|R_{F_i}$ , where  $\rho_0$  and  $E_0$  are ideally associated with  $|0\rangle\langle 0|$  and  $Z$ , respectively.

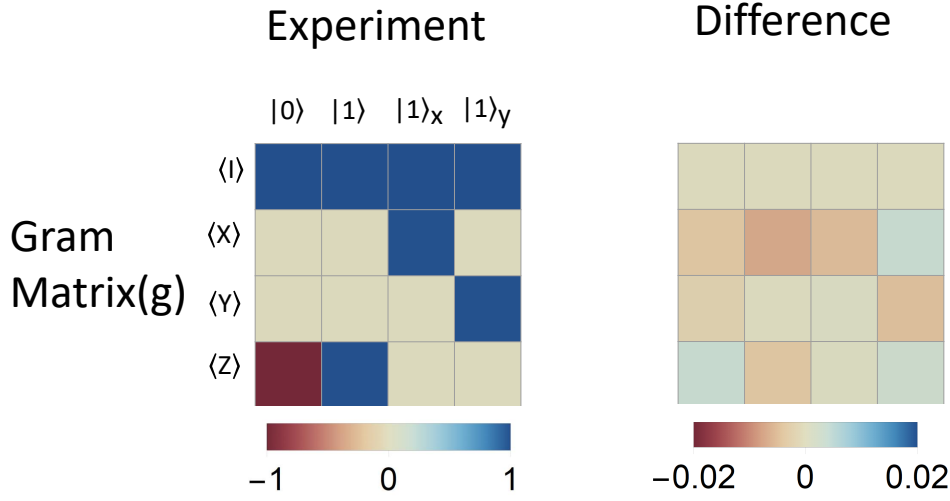


Figure 6.2 Gram matrix. The single-qubit experiments are implemented with a single trapped ion. The Gram matrix characterizes the SPAM error, which is obtained by preparing states in  $\mathcal{S}_1$  and measuring expectation values of operators in  $\mathcal{P}_1$ . The left column shows the experimentally-obtained matrices and the right column shows the difference between the experimental and the ideal matrices.

### 6.3.2 Maximum-likelihood gate set tomography

For single-qubit randomized benchmarking<sup>[25]</sup>, we design pulse sequences for implementing major-axis  $\pi$  pulses  $\{X_{\pm\pi}, Y_{\pm\pi}, Z_{\pm\pi}\}$  and  $\frac{\pi}{2}$  pulses  $\{X_{\pm\frac{\pi}{2}}, Y_{\pm\frac{\pi}{2}}\}$ . Thus the gate set for the single-qubit case is  $\mathcal{G}_1 = \{I, X_{\pm\pi}, Y_{\pm\pi}, Z_{\pm\pi}, X_{\pm\frac{\pi}{2}}, Y_{\pm\frac{\pi}{2}}\}$ , where  $I$  is the identity operation. The gate set for implementing two-qubit random circuits are  $\mathcal{G}_2 = \mathcal{G}_1^{\otimes 2} \cup \{MS_{YY}, MS_{ZZ}\}$ . We experimentally obtain the PTMs of all the gates in the gate set by maximizing a likelihood function with the assumption that Pauli errors are dominant in our devices.

To obtain the PTMs of all the gates in the gate set, we experimentally measure informationally complete data consisting of the average  $\bar{m}_{ijk}$  and variance  $\Delta_{ijk}$  of the expectation value  $\langle\langle E_i | R_{G_j} | \rho_k \rangle\rangle$ , which are obtained by repeating the corresponding experimental settings enough number of times. We assume Pauli errors are dominant in our device, where each of the noisy quantum gate  $G_j \in \mathcal{G}_n$  is modeled with the ideal gate  $G_j^{id}$  followed by a Pauli error channel. We use maximum likelihood estimation for the reconstruction of PTMs of all the gates in the gate set, parameterized as ansatz  $R_{G_j} = N_j R_{G_j}^{id}$ , where  $N_j = \sum_l p_{j,l} R_{P_l}$ , with variational parameters being gate-specific Pauli error rates  $p_{j,l}$ .

With the ansatz for each gate, we calculate the ansatz prediction for the expectation value of each experimental setting, denoted as  $m_{ijk}$ . We then define the following likelihood function<sup>[92]</sup>,

$$\mathcal{L} = \prod_{i,j,k} \exp \left[ -(m_{ijk} - \bar{m}_{ijk})^2 / \Delta_{ijk}^2 \right], \quad (6-1)$$

which takes its maximum value when the experimental average values  $\bar{m}_{ijk}$  and the ansatz expectations  $m_{ijk}$  coincide with each other. Thus, the gate-specific Pauli error rates can be determined by maximizing the likelihood function, with which we construct the PTMs of the imperfect gates that are implementable in the quantum device.

### 6.3.3 PTMs for single- and two-qubit gate set

We use gate set tomography to characterize the single-qubit operations. In the superoperator formalism, each experimental single-qubit operation  $R_{G_s}$  can be describe as an ideal 4 by 4 PTM followed by a PTM of noise operation  $N_s$ . With Pauli error assumption, each  $N_s$  can be written as  $N_s = p_{s,0}R_I^{id} + p_{s,1}R_X^{id} + p_{s,2}R_Y^{id} + p_{s,3}R_Z^{id}$ , where  $p_{s,j}$  are the Pauli error rates and  $\sum_j p_{s,j} = 1$  for trace preserving condition. Since there are 11 gate in  $\mathcal{G}_1$ ,  $\mathcal{F}_1 \subset \mathcal{G}_1$  and the experimental initial state  $\rho_0$  can be characterized by 3 parameters, we need to obtain the values for  $11 \times 3 + 3 = 36$  parameters. We run  $3 \times 11 \times 4$  different experimental settings specified by  $\langle\langle E_0 | R_{F_k} R_{G_j} R_{F_i} | \rho_0 \rangle\rangle$  with repetitions of 10000 per setting to collect experimental data  $\bar{m}_{ijk}$ , where  $i = 1, \dots, 4$  for state preparation,  $j = 1, \dots, 11$ , and  $k = 1, 2, 3$  for different measurement settings. The ansatz prediction  $m_{ijk} = \langle\langle E_0 | N_{F_k} R_{F_k}^{id} N_{G_j} R_{G_j}^{id} N_{F_i} R_{F_i}^{id} | \rho_0 \rangle\rangle$  contain Pauli error rates as variational parameters, which we numerically optimize to maximize the likelihood function. The reconstructed PTMs of  $X_{\pm\frac{\pi}{2}}, Y_{\pm\frac{\pi}{2}}, X_{\pm\pi}, Y_{\pm\pi}, I$  and  $Z_{\pm\pi}$  for the single-qubit case are shown in Fig. 6.3.

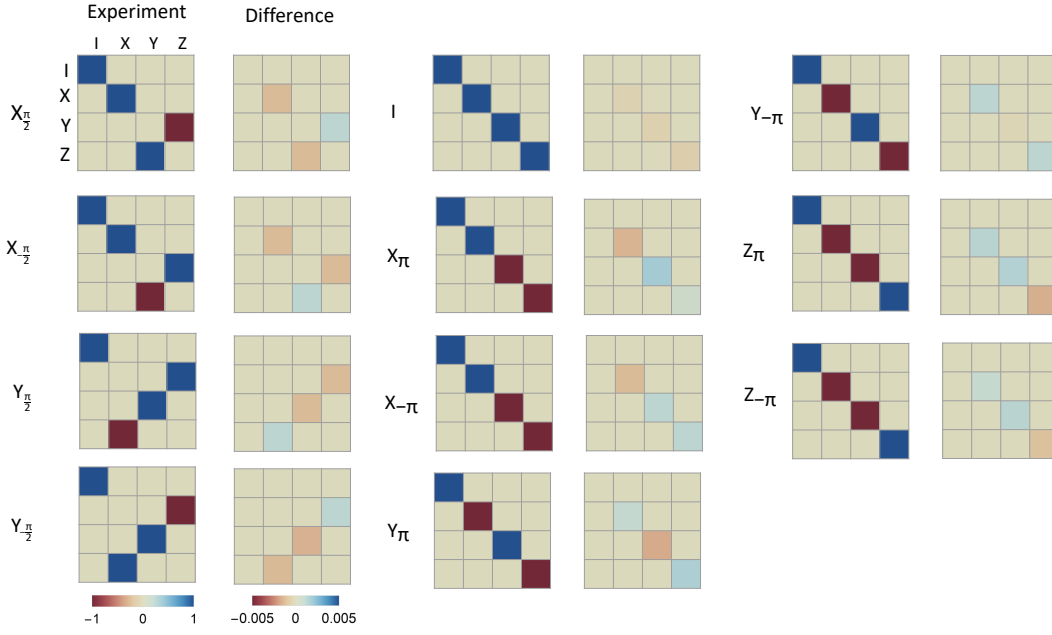


Figure 6.3 PTMs of single-qubit gates for the single-qubit case. The single-qubit experiments are implemented with a single trapped ion. Here we show the PTMs of experimental gates  $X_{\pm\frac{\pi}{2}}$  and  $Y_{\pm\frac{\pi}{2}}$ , the so-called computational gates in randomized benchmarking. And single-qubit randomized benchmarking needs not only the computational gate set, but also the identity and  $\pi$  pulses<sup>[25]</sup>. In order to implement error-mitigation for single-qubit randomized benchmarking, these gates should be characterized. In each subfigure, the left column shows the experimentally-obtained matrices and the right column shows the difference between the experimental and the ideal matrices, i.e.  $R_G - R_G^{id}$  with  $G$  being one of the quantum operations being characterized.

For the gate set tomography of two qubits, we apply a two-step parameter estimation, since the infidelities for the single-qubit gates are about an order lower than those of the two-qubit gates. We first determine the Pauli error rates for all the single-qubit gates in  $\mathcal{G}_1^{\otimes 2}$  as described above, and then characterize the two-qubit gate  $MS_{YY}$  based on the knowledge of the characterized single-qubit gates. The  $MS_{ZZ}$  gate is derived from those results.

The two-qubit gate set, i.e.  $\mathcal{G}_2$ , includes single-qubit operations in  $\mathcal{G}_1^{\otimes 2}$  and two-qubit operations  $\{MS_{YY}, MS_{ZZ}\}$ . Since infidelities for the single-qubit gates are about an order lower than those of the two-qubit gates, it is reasonable to divide the maximum likelihood estimation into two steps.

First, we treat each qubit in the two-qubit system as a single-qubit system and characterize the single-qubit gate set  $\mathcal{G}_1$  by gate set tomography, obtaining single-qubit PTMs. The two-qubit PTMs of the single-qubit operations in  $\mathcal{G}_1^{\otimes 2}$  is then obtained by direct product of the single-qubit PTMs on both qubits. Since the fiducial set  $\mathcal{F}_2 \in \mathcal{G}_1^{\otimes 2}$ , the PTMs of the fiducial operations are determined at this step.

Second, we characterize the native two-qubit  $MS_{YY}$  gate. Under the Pauli-error assumption, the PTM of the experimental  $MS_{YY}$  gate is decomposed as  $R_{MS_{YY}} = N_{MS_{YY}} R_{MS_{YY}}^{id}$ , where  $N_{MS_{YY}}$  is the PTM of the Pauli-error channel containing 16 two-qubit Pauli components. After considering the trace-preserving constraint,  $N_{MS_{YY}}$  has 15 parameters, which are determined by linear equations connecting the ansatz prediction  $\langle\langle E_0^{\otimes 2} | R_{F_k} N_{MS_{YY}} R_{MS_{YY}}^{id} R_{F_i} | \rho_0^{(1)} \otimes \rho_0^{(2)} \rangle\rangle$  and corresponding experimental results. In order to minimize the projection error, we choose 15 linearly independent equations out of  $16 \times 9$  different settings, with most of the measured probabilities close to 0 or 1. Fig. 6.4 shows the corresponding circuits for the experimental settings.

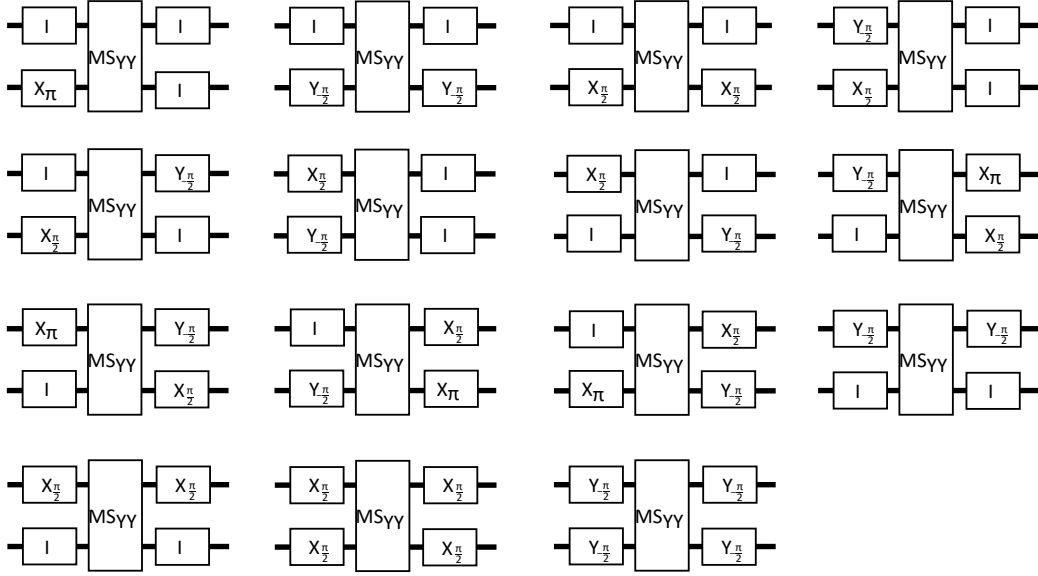


Figure 6.4 **Experimental circuits for the characterization of the  $MS_{YY}$  gate.** The two-qubit system is first prepared in the initial  $|00\rangle$  state by optical pumping. After implementing one of the quantum circuit, a projective measurement of  $Z^{\otimes 2}$  is carried out. The above sequence is repeated 3000 times for each circuit to estimate the probability of the dark  $|00\rangle$  state, which, together with the corresponding ansatz prediction, determines one of the Pauli-error rate for the experimental  $MS_{YY}$  gate.

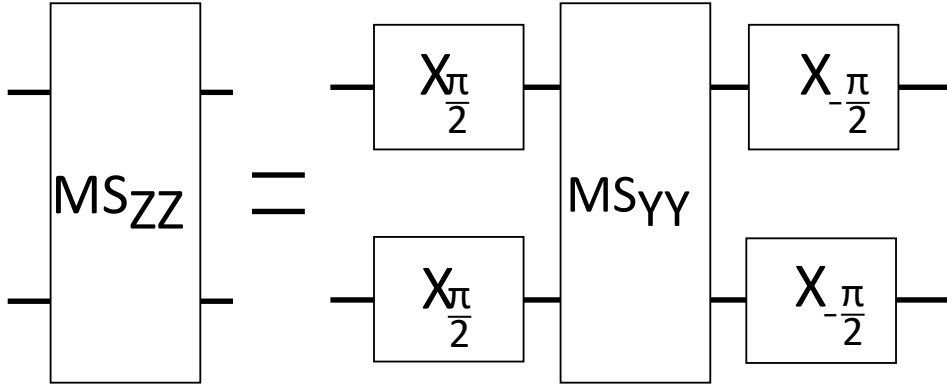


Figure 6.5 The  $MS_{ZZ}$  gate is realized by adding single-qubit rotations before and after the  $MS_{YY}$  gate.

Since the  $MS_{ZZ}$  is implemented by a  $MS_{YY}$  gate sandwiched by proper single-qubit gates, the PTM of the experimental  $MS_{ZZ}$  gate is obtained by multiplying the PTMs of the corresponding experimental operations, i.e.  $R_{MS_{ZZ}} = R_{X_{-\frac{\pi}{2}} \otimes X_{-\frac{\pi}{2}}} R_{MS_{YY}} R_{X_{\frac{\pi}{2}} \otimes X_{\frac{\pi}{2}}}$ , as shown in Fig. 6.5. The reconstructed PTMs of  $MS_{YY}$  and  $MS_{ZZ}$  gates for the two-qubit case are shown in Fig. 6.6.

Using these reconstructed PTMs, we numerically simulate the single-qubit randomized benchmarking and two-qubit random circuits on a classical computer. The comparisons between the numerically-reconstructed and experimental data clearly validate the Pauli error assumption within both error-bars, as shown in Fig. 6.7.



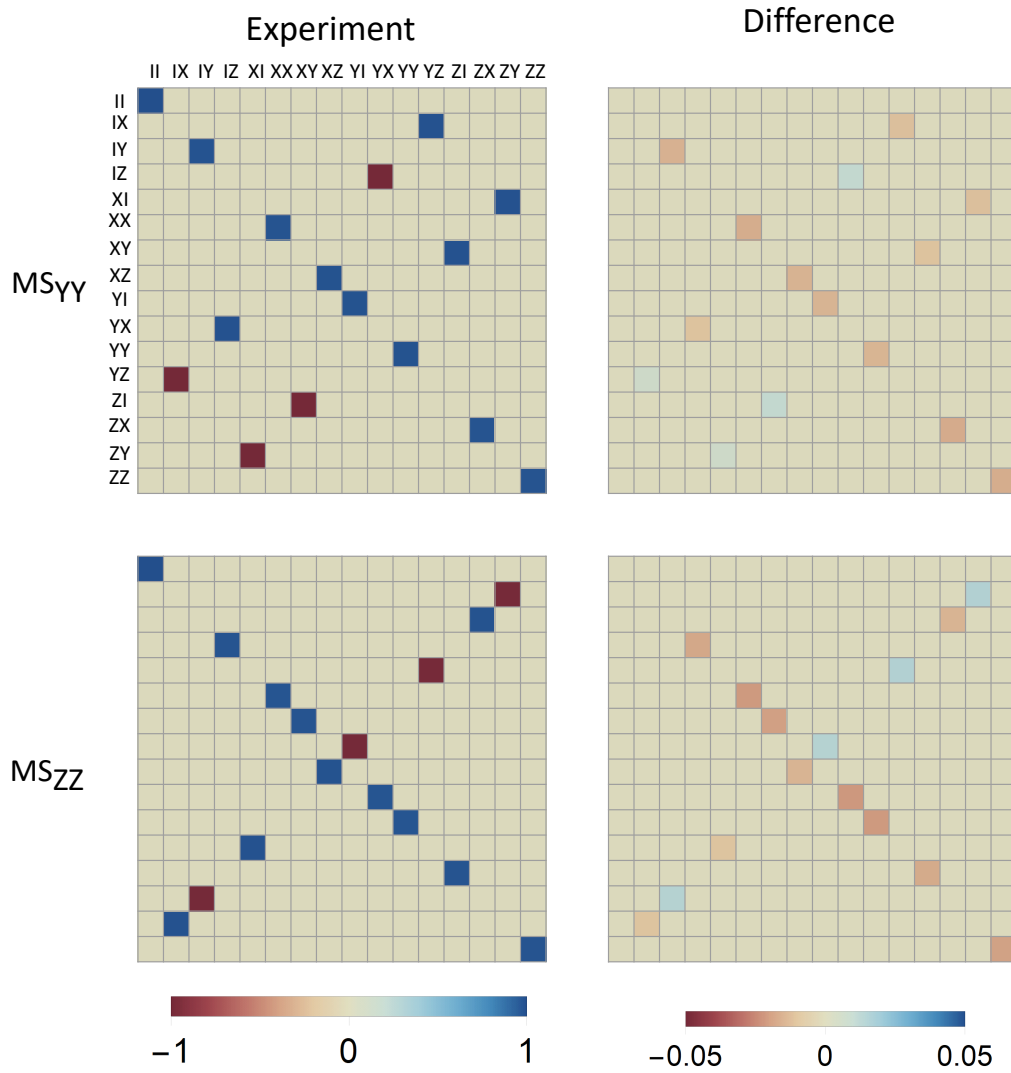


Figure 6.6 Pauli transfer matrices of the experimental gates  $MS_{YY}$  and  $MS_{ZZ}$  in the two-qubit case. Note that we calibrate the SPAM errors as proposed in Ref. <sup>[96]</sup>, and the PTMs of single-qubit gates on both qubits (not shown) are not noticeably different to those for the single-qubit case. In each subfigure, the left column shows the experimentally-obtained matrices and the right column shows the difference between the experimental and the ideal matrices, i.e.  $R_G - R_G^{id}$  with  $G$  being one of the quantum operations being characterized.

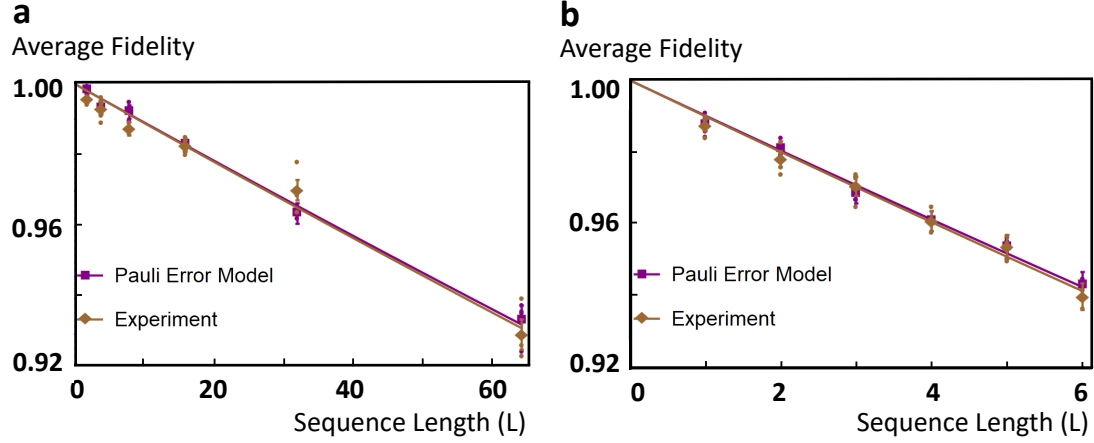


Figure 6.7 **Verification of the Pauli-error assumption.** **a.** The average fidelity of the numerical (purple dots) and experimental (yellow dots) single-qubit random sequences as functions of the sequence length  $L$ . The numerical data are obtained by simulating the quantum dynamics with the experimental PTMs with the Pauli-error assumption. The curves are obtained by fitting an exponential decaying model to the data. The numerical and experimental error rates, being  $(1.09 \pm 0.06) \times 10^{-3}$  and  $(1.10 \pm 0.12) \times 10^{-3}$  respectively, are consistent within fitting errors. **b.** The same as **a.** for random two-qubit sequences. The numerical and experimental error rates are  $(0.97 \pm 0.05) \times 10^{-2}$  and  $(0.99 \pm 0.06) \times 10^{-2}$ . Thus the comparison in **a.** and **b.** validate the Pauli-error assumption in our system.

## 6.4 Decomposition of noise operations

The initial state, quantum gates and measurement are deviated from the ideal ones, as experimentally characterized by Gram matrix and PTMs. Mathematically, We can reconstruct the ideal ones by weighted combination of experimental operations<sup>[17-18]</sup>. Since we cannot distinguish errors in state preparation from those in measurement, we ascribe all of the SPAM errors to state preparation and decompose the initial state  $|\rho_0^{id}\rangle\rangle = \sum_i q_{0,i} |\rho_i\rangle\rangle$ . The quasi-probabilities  $q_{0,i}$  for the decomposition of the ideal single-qubit initial state is shown in Fig. 6.8a. Note that for the two-qubit case, the SPAM errors are much more serious because of the EMCCD, and we calibrate the results to remove the SPAM errors as proposed in Ref.<sup>[96]</sup>. We prepare the system in the states  $|00\rangle$  and  $|11\rangle$ , and measure the state fidelities of  $|0\rangle$  and  $|1\rangle$  for both qubits. The infidelities of these states give the SPAM error probability associated with each measurement outcome, which can then be used to remove the SPAM errors by data processing.

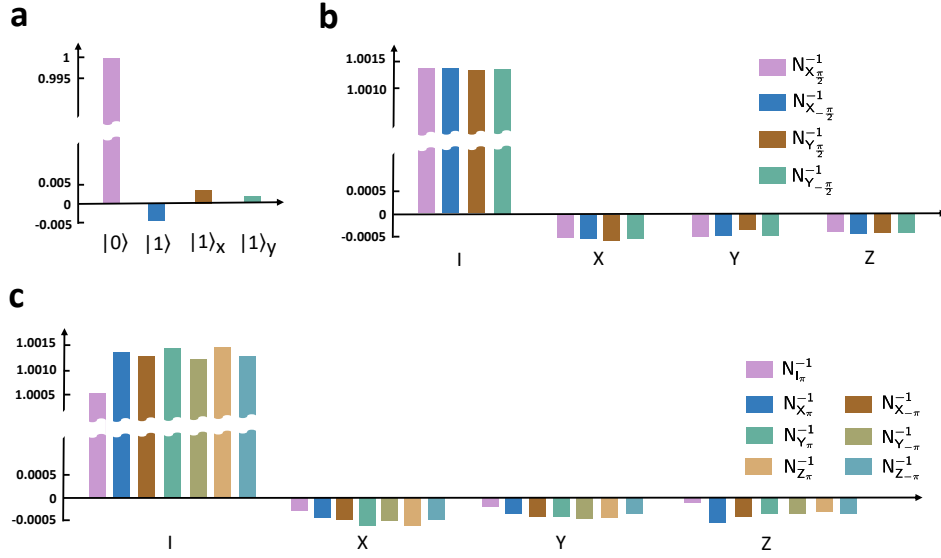


Figure 6.8 **Quasi-probability decomposition.** **a.** Quasi-probabilities in the decomposition of the ideal single-qubit initial state with experimental initial states in  $\mathcal{S}_1$ . **b.** Quasi-probabilities in the decomposition of the inverse noise operations of the four experimental single-qubit gates  $\{X_{\pm\pi/2}, Y_{\pm\pi/2}\}$ . **c.** The same as **b.** for the experimental single-qubit gates  $\{I, X_{\pm\pi}, Y_{\pm\pi}, Z_{\pm\pi}\}$ .

An ideal quantum gate  $G_s^{id}$  can be written as the experimental one followed by the inverse of noise operation, i.e.  $R_{G_s}^{id} = N_s^{-1}R_{G_s}$ , where the noise operation  $N_s$  introduces errors in the experimental gate  $R_{G_s} = N_s R_{G_s}^{id}$ . The inverse of the noise operation  $N_s^{-1}$  is then decomposed by the experimental operations associated with the  $n$ -qubit Pauli group,  $N_s^{-1} = \sum_j q_{s,j} R_{P_j}$  with Pauli error assumption, where the quasi-probabilities  $q_{s,j}$  are determined by a set of linear equations. We show decompositions of the inverse error operations for single-qubit gates  $\{X_{\pm\pi/2}, Y_{\pm\pi/2}\}$  in Fig. 6.8b, for single-qubit gates  $\{I, X_{\pm\pi}, Y_{\pm\pi}, Z_{\pm\pi}\}$  in Fig. 6.7c and for two-qubit gates  $\{MS_{YY}, MS_{ZZ}\}$  in Fig. 6.9.

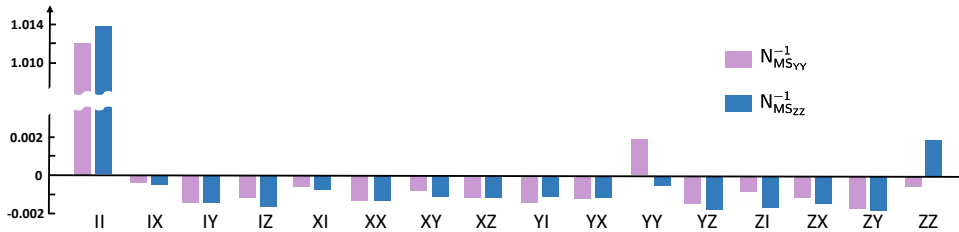


Figure 6.9 Quasi-probabilities in the decomposition of the inverse noise operations for the experimental two-qubit gates  $\{MS_{YY}, MS_{ZZ}\}$ .

## 6.5 Benchmarking of the quantum error mitigation protocol

We benchmark the performance of the quantum error mitigation using a set of random computations, in the spirit of randomized benchmarking. Each specific computation starts with fully polarized initial states,  $|0\rangle$  in the single-qubit case and  $|00\rangle$  in the two-qubit case, and ends with measuring  $Z$  on each qubit. Between the state preparation and measurement, there is a sequence of randomly-selected quantum gates. We note that the randomness in selecting the gate sequence is for the purpose of benchmarking the performance rather than correcting errors. For each specific computation, i.e. gate sequence, we apply the error mitigation and modify the gate sequence with random basis operations to correct errors. We remark that, for each specific computation, we observe the improvement on the computation accuracy by using the error mitigation.

### 6.5.1 Single-qubit gate randomized benchmarking

For the single-qubit case, benchmarking computations are selected according to the standard randomized benchmarking, i.e. a gate sequence of length  $L$  contains  $L$  computational gates and  $L + 1$  interleaving identity or Pauli operations, uniformly drawn from the set  $\{X_{\pm\frac{\pi}{2}}, Y_{\pm\frac{\pi}{2}}\}$  and  $\{I, X_{\pm\pi}, Y_{\pm\pi}, Z_{\pm\pi}\}$ , respectively. For each sequence length  $L$ , we choose 4 sequences whose ideal final states are the eigenstates of the Pauli  $Z$  operator. We then repeatedly implement each of the sequences with a trapped-ion system consisting of a single trapped ion, and measure the state fidelity between the ideal and experimentally prepared final states. In Fig. 6.7a, we show the dependence of the average fidelity without error mitigation, obtained by averaging the state fidelities over sequences of the same length, on the sequence length. We numerically fit the average fidelity with an exponential function and obtain the error rate per single-qubit gate as  $(1.10 \pm 0.12) \times 10^{-3}$ .

In order to obtain unbiased estimator of the expectation value, both the initial state and  $2L + 1$  gates in the selected sequence need to be decomposed and resampled, where the initial state is replaced probabilistically by one of the states in  $\mathcal{S}_1$ , and each experimental gate is followed by a random Pauli or identity operation drawn from  $\mathcal{P}_1$ . Thus, for a specific computation with  $(2L + 1)$  gates, there are  $4^{2L+2}$  possible experimental settings. Since the number of settings grows exponentially with the length of the random sequence, we use the Monte-Carlo method to compute the result by sampling random experimental settings, which are specified by an index  $i$  for the initial state  $|\rho_i\rangle\rangle$  and two  $(2L + 1)$ -entry index vectors  $\mathbf{a} \equiv (a_1, \dots, a_{2L+1})$

and  $\mathbf{b} \equiv (b_1, \dots, b_{2L+1})$  specifying the computation and the choices of the error-compensating operations. We note that for a specific computation,  $\mathbf{a}$  is determined, but  $\mathbf{b}$  is random. The probability of an experimental setting  $\langle\langle E_0 | \prod_{l=1}^{2L+1} R_{P_{b_l}} R_{G_{a_l}} | \rho_i \rangle\rangle$ , where  $G_{a_l} \in \mathcal{G}_1$  and  $P_{b_l} \in \mathcal{P}_1$ , is  $C^{-1} \left| q_{0,i} \left( \prod_{l=1}^{2L+1} q_{a_l, b_l} \right) \right|$ . Here, the rescaling factor  $C = \sum_{i, \dots, (a_l, b_l), \dots} \left| q_{0,i} \left( \prod_{l=1}^{2L+1} q_{a_l, b_l} \right) \right| \geq 1$  characterizes the cost to mitigate the errors. Note that the signs of the coefficients, i.e.,  $\text{sgn} \left[ q_{0,i} \left( \prod_{l=1}^{2L+1} q_{a_l, b_l} \right) \right]$ , are integrated into the measurement results of the random experiments.

The concrete procedure of applying the probabilistic error-cancellation to a given quantum computation task consists of the so-called characterization and calculation phases. The characterization phase is described above. In the calculation phase, we estimate expectation values of quantum circuits with the characterized imperfect quantum device. We first write down the unbiased estimator of the expectation value of a specific quantum circuit as  $\langle\langle E_0^{id} | R_{G_{a_L}}^{id} \dots R_{G_{a_1}}^{id} | \rho_0^{id} \rangle\rangle$ , which can be expanded with the quasi-probability distributions obtained in the characterization phase as follows,

$$\begin{aligned} \langle\langle E_0^{id} | R_{G_{a_L}}^{id} \dots R_{G_{a_1}}^{id} | \rho_0^{id} \rangle\rangle &= \sum_i \sum_{b_1, \dots, b_L} q_{0,i} q_{a_1, b_1} \dots q_{a_L, b_L} \\ &\langle\langle E_0^{id} | R_{P_{b_L}} R_{G_{a_L}} \dots R_{P_{b_1}} R_{G_{a_1}} | \rho_i \rangle\rangle, \end{aligned} \quad (6-2)$$

where the expectation value of  $\langle\langle E_0^{id} | R_{P_{b_L}} R_{G_{a_L}} \dots R_{P_{b_1}} R_{G_{a_1}} | \rho_i \rangle\rangle$  can be obtained by repeating the specific experimental setting and averaging the measurement results. The straightforward way to evaluate the unbiased estimator is summing over all possible settings. However, this is impractical because the number of settings grows exponentially with the circuit depth. To alleviate the exponential growth, we rewritten the above expansion as a probability distribution as follows,

$$\begin{aligned} \langle\langle E_0^{id} | R_{G_{a_L}}^{id} \dots R_{G_{a_1}}^{id} | \rho_0^{id} \rangle\rangle &= C_{\mathbf{a}} \sum_{i, \mathbf{b}} P_{\mathbf{a}}(i, \mathbf{b}) g(i, \mathbf{a}, \mathbf{b}) \\ &\langle\langle E_0^{id} | R_{P_{b_L}} R_{G_{a_L}} \dots R_{P_{b_1}} R_{G_{a_1}} | \rho_i \rangle\rangle, \end{aligned} \quad (6-3)$$

with the short-hand notations  $\mathbf{a} \equiv (a_1, \dots, a_L)$  and  $\mathbf{b} \equiv (b_1, \dots, b_L)$ , where  $C_{\mathbf{a}} \equiv \sum_{i, \mathbf{b}} |q_{0,i}| \prod_l |q_{a_l, b_l}|$  is the rescaling factor,  $P_{\mathbf{a}}(i, \mathbf{b}) = |q_{0,i}| \prod_l |q_{a_l, b_l}| / C$  is the probability distribution, and  $g(i, \mathbf{a}, \mathbf{b}) = \text{sgn} \left( q_{0,i} \prod_l q_{a_l, b_l} \right)$  is the sign of the setting. Then, we use important sampling to generate  $M$  experimental settings, specified by  $(i_m, \mathbf{b}_m)$  with  $m = 1, \dots, M$ , according to the probability distribution  $P_{\mathbf{a}}(i, \mathbf{b})$ , and calculate the expectation value as follows,

$$\langle\langle E_0^{id} | R_{G_{a_L}}^{id} \dots R_{G_{a_1}}^{id} | \rho_0^{id} \rangle\rangle = \frac{C_{\mathbf{a}}}{M} \sum_{m=1}^M g(i_m, \mathbf{a}, \mathbf{b}_m) O(i_m, \mathbf{a}, \mathbf{b}_m), \quad (6-4)$$

where  $O(i_m, \mathbf{a}, \mathbf{b}_m)$  is the result of the projective measurement of the  $m$ -th setting, being either 0 or 1 in our experiment.

In Fig. 6.10, we represent the error-mitigated single-qubit randomized benchmarking with length  $L$  up to 64, and show that the single-qubit gate error rate is effectively suppressed to  $(1.44 \pm 5.28) \times 10^{-5}$ .

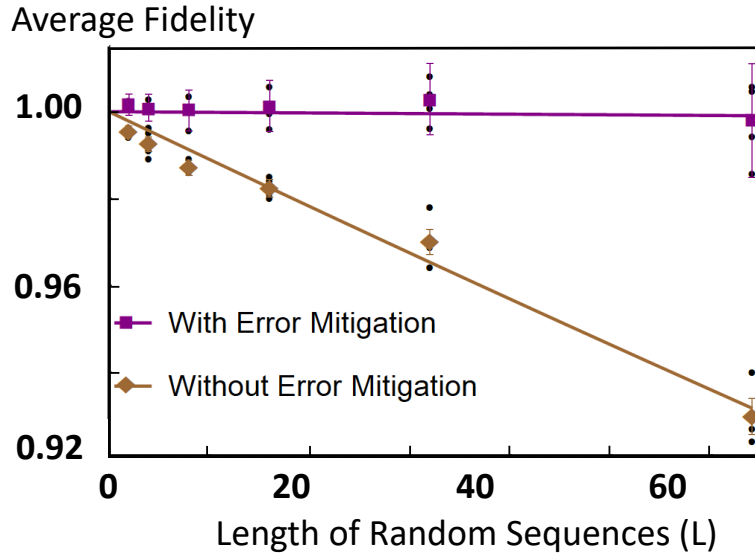


Figure 6.10 The single-qubit randomized benchmarking. The data points with (purple square) and without (yellow diamond) error mitigation are obtained from averaging the final-state fidelity over different random sequences of the same length (black dots). The error bars are the standard deviation of the average fidelities computed using the formula of uncertainty propagation. The solid lines, obtained by fitting, show the exponential decrease of the average fidelities, indicating the physical and effective average errors per gate being  $(1.10 \pm 0.12) \times 10^{-3}$  and  $(1.44 \pm 5.28) \times 10^{-5}$ , respectively. Please note that some of the fidelities with error mitigation are larger than 1 because of the rescaling factor  $C > 1$  (see Main Text and Methods) and the limited sampling for data points. Although the current protocol does not guarantee a physical outcome, the error mitigation procedure shifts the distribution of the computation result towards the true value with large enough sampling.

### 6.5.2 Two-qubit gate randomized benchmarking

For the two-qubit case, we select four gate sequences as benchmarking computations for each length  $L$ . Each sequence contains  $L$  two-qubit gates uniformly drawn from

the set  $\{MS_{YY}, MS_{ZZ}\}$  with interleaving single-qubit gates<sup>[97]</sup>. The sequence is selected under the restriction that the ideal final state is an eigenstate of  $Z^{\otimes 2}$ . Similar to the single-qubit case described above, we apply error mitigation to each of the two-qubit gate sequences with length  $L$  up to 6, and represent the error-mitigated results in Fig. 6.11, where the two-qubit gate error rate is effectively suppressed from  $(0.99 \pm 0.06) \times 10^{-2}$  to  $(0.96 \pm 0.10) \times 10^{-3}$ .

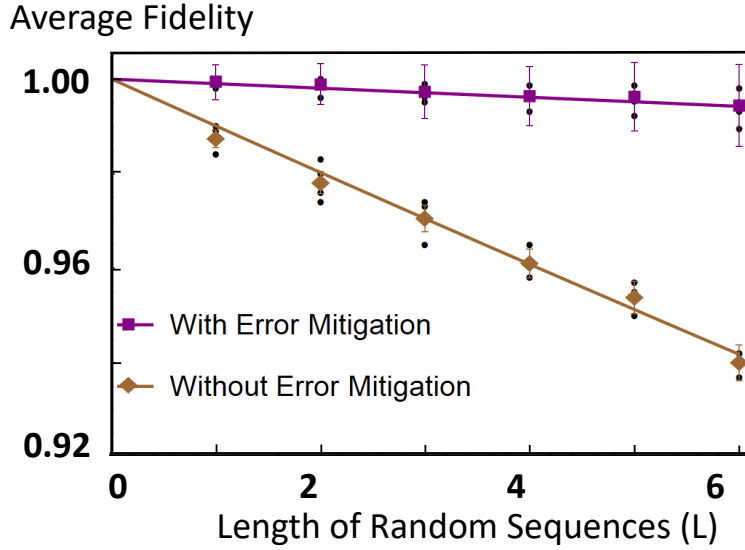


Figure 6.11 The two-qubit random-circuit computation. Decay rates indicated by the average fidelity curves without and with error mitigation are  $(0.99 \pm 0.06) \times 10^{-2}$  and  $(0.96 \pm 0.10) \times 10^{-3}$ , respectively.

## 6.6 Analysis on residual errors

Theoretically, the error mitigation technique, combining probabilistic error cancellation and gate set tomography, is capable of completely rectifying the effect of errors in the estimation of expectation values. However, in our experiment, the effective error rates after error mitigation are  $(1.44 \pm 5.28) \times 10^{-5}$  and  $(0.96 \pm 0.10) \times 10^{-3}$  in the single-qubit and two-qubit cases, respectively. Generally speaking, the reasons for the residual errors include the Pauli-error assumption, time-correlated systematic drift, and crosstalk errors between qubits.

In the single-qubit case, the residual errors mainly come from the introduction of the Pauli-error model. To quantify the non-Pauli error rate, we simulate the dynamics of the same random sequences as those used in the experiment with the characterized experi-

mental PTMs, which are obtained under the Pauli-error assumption. The experimental and simulated data of average fidelity are shown in Fig. 6.7a, which are then numerically fitted to extract the error rates. The difference between the simulated and experimental error rates for single-qubit gates is  $1.41 \times 10^{-5}$ , which are of the same order of the residual error rate in the single-qubit case. Meanwhile, the data shows that the time-correlated systematic drift has negligible effect and cannot be faithfully quantified within experimental and fitting errors.

In our experiment, we implement two different two-qubit gates, i.e.  $MS_{YY}$  and  $MS_{ZZ}$  gates. To quantify the residual errors from the Pauli-error assumption, we compare the dynamics of the simulated and experimental random two-qubit sequence, where the simulation is based on the characterized PTMs with the Pauli-error assumption. The difference between the simulated and experimental error rates gives the estimation of the non-Pauli residual error rate, which is about  $0.20 \times 10^{-3}$ . As to the crosstalk errors, the situations for  $MS_{YY}$  and  $MS_{ZZ}$  gates are quite different because of different implementation schemes. Specifically, a  $MS_{ZZ}$  gate is implemented by a  $MS_{YY}$  gate sandwiched by proper single-qubit gates, which introduce qubit-crosstalk errors. We model the crosstalk effect by measuring an effective Rabi frequency  $\Omega_{eff}$  on the neighboring ion induced by leakage laser intensities when a single-qubit gate is being implemented by lasers focused on one of the ions. The ratio  $\Omega_{eff}/\Omega$ , with  $\Omega$  being the Rabi frequency of the target ion, thus quantifies the severity of crosstalk errors. As shown in Supplementary Fig. 6.12, we numerically simulate the state fidelities of the original and error-mitigated  $MS_{YY}$  and  $MS_{ZZ}$  gates. As expected, the numerical results show that  $MS_{YY}$  gates, either original or error-mitigated ones, are insensitive to the crosstalk errors, while the fidelities of  $MS_{ZZ}$  gates degrade as the severity of crosstalk errors increases. According to the numerical results, the crosstalk residual error rate is about  $0.68 \times 10^{-3}$  at the experimental level of qubit crosstalk. Finally, the remaining part of the residual error rate,  $0.08 \times 10^{-3}$ , is attributed to the time-correlated systematic drift.



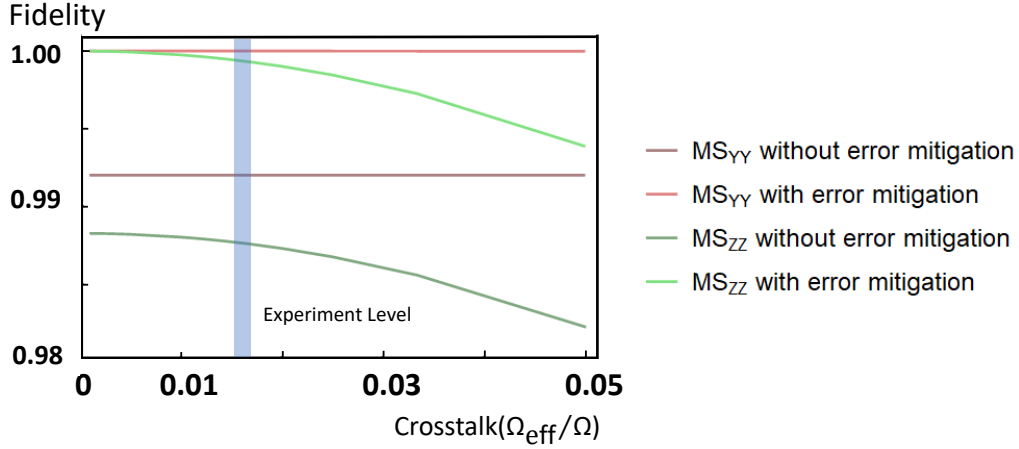


Figure 6.12 Analysis of the qubit crosstalk effect. We numerically simulate the final-state fidelity of the original and error-mitigated  $MS_{YY}$  and  $MS_{ZZ}$  gates as functions of the qubit crosstalk strength, which is modeled by the ratio  $\Omega_{eff}/\Omega$ , with  $\Omega$  and  $\Omega_{eff}$  being the Rabi frequencies experienced by the target and the neighboring ions when a single-qubit gate is being implemented. The experimental level of the qubit crosstalk strength is shaded with blue, which given an estimation of  $0.68 \times 10^{-3}$  for the residual error rate induced by the qubit crosstalk effect.

## 6.7 Discussion

Our work shows that for the estimation of expectation values, the error mitigation technique, i.e. probabilistic error cancellation<sup>[17-18,21]</sup>, surely have the capacity of surpassing the break-even point, where the effective gates are superior to their physical building blocks, at an affordable cost with respect to near-future quantum techniques. We note that error mitigation techniques are developed for the intermediate scale quantum computation. The cost of the error mitigation increases with the circuit depth, therefore, techniques like quantum error correction are still needed for large-scale fault-tolerant quantum computation. The effective infidelity after error mitigation comes from the Pauli error assumption, time-dependent systematic drifting<sup>[98]</sup> for both single-qubit and two-qubit cases and cross-talk error of single-qubit addressing operations for the two-qubit case. Thus further improvement requires both calibrating and stabilizing the quantum device. There are two methods to suppress the cross-talk error: the composite sequences<sup>[99]</sup> and the spatial refocusing technique<sup>[100]</sup>. The first method works well for localized beams to produce narrowband sequences of improving total pulse area. The latter can use broad

beams to reconstruct a focused beam by spectrally decomposing the desired amplitude profile. With technologies to tackle the cross-talk error, the probabilistic error cancellation method of quantum error mitigation can be straightforwardly applied to systems with more qubits for realizing high-fidelity quantum computation. Our demonstration opens up the possibility of implementing high-fidelity computations on a near-term noisy quantum device.

## Chapter 7 Error-mitigated Hubbard model simulation

### 7.1 Overview of Hubbard model

The fermionic Hubbard model is first proposed to describe the electrons in the solid-state system, which is the simplest model to describe many-body interactions like the transition between insulating and conducting systems<sup>[101]</sup>. It mainly contains two terms in the Hamiltonian: the tunneling between sites within the lattice and the on-site interaction, which can be written as<sup>[102]</sup>

$$H = -J \sum_i (b_i^\dagger b_{i+1} + b_{i+1}^\dagger b_i) + U \sum_{i=1}^N n_{i\uparrow} n_{i\downarrow}, \quad (7-1)$$

where  $b_i^\dagger$  and  $b_i$  are the creation and the annihilation operators for the fermionic mode on the  $i$ -th site. The first term is the hopping between sites and the second term is the on-site repulsion. Note that the fermionic operators satisfy the following canonical anticommutation relations,

$$\begin{aligned} \{b_i, b_j\} &= \{b_i^\dagger, b_j^\dagger\} = 0 \\ \{b_i, b_j^\dagger\} &= \delta_{ij}. \end{aligned} \quad (7-2)$$

Fermionic operators can be mapped to spin operators by the Jordan-Wigner transformation, which is

$$b_i = \prod_j^{i-1} \sigma_{j,z} \sigma_{i,-}, \quad (7-3)$$

where  $\{\sigma_{i,x}, \sigma_{i,y}, \sigma_{i,z}\}$  are the Pauli matrices on the  $i$ -th site and  $\sigma_{i,\pm} = (\sigma_{i,x} \pm i\sigma_{i,y})/2$ .

After the Jordan-Wigner transformation, the Hamiltonian in Eq.( 7-1) becomes

$$H = \frac{J}{2} \sum_i (\sigma_{i,x} \sigma_{i+1,x} + \sigma_{i,y} \sigma_{i+1,y}) + \frac{U}{4} \sum_i (\sigma_{i,z} \sigma_{i+1,z} + \sigma_{i,z} + \sigma_{i+1,z}), \quad (7-4)$$

which is hard to directly apply on trapped ion systems with the analog scheme, and can be realized through Suzuki-Trotter expansion with the digital scheme. We can divide the

Hamiltonian into three parts,  $H = H_1 + H_2 + H_3$ , with

$$\begin{aligned} H_1 &= \frac{J}{2} \sum_i (\sigma_{i,x} \sigma_{i+1,x}), \\ H_2 &= \frac{J}{2} \sum_i (\sigma_{i,y} \sigma_{i+1,y}), \\ H_3 &= \frac{U}{4} \sum_i (\sigma_{i,z} \sigma_{i+1,z} + \sigma_{i,z} + \sigma_{i+1,z}). \end{aligned} \quad (7-5)$$

Then the exact evolution operator can be decomposed as follows,

$$e^{-iHt} = (e^{-iH_1\Delta t} e^{-iH_2\Delta t} e^{-iH_3\Delta t})^n + O(n\Delta t^2), \quad (7-6)$$

with  $\Delta t = t/n$  and  $n$  is the Trotter step, which can be implemented by the combination of two-qubit gates or global entangling gates and single-qubit rotations.

The main error source contains two parts: the Trotter expansion error in theory and the error of quantum gates in experiment. The first part can be reduced by increasing the Trotter steps or using higher-order Suzuki-Trotter expansion. For example, the second order Trotter expansion can suppress the error by one order of magnitude as

$$e^{-iHt} = (e^{-iH_1\Delta t/2} e^{-iH_2\Delta t/2} e^{-iH_3\Delta t} e^{-iH_2\Delta t/2} e^{-iH_1\Delta t/2})^n + O(n\Delta t^3). \quad (7-7)$$

We don't pay much attention on this part for now. The second part can be improved by optimizing the stability of the system and using pulse shaping methods in the physical level, or through the probabilistic error cancellation scheme we discussed in chapter 6 in the classical programming level. Here, we present the numerical study of error mitigation for Fermi-Hubbard model dynamics. The simulating results of two and three fermionic modes show the powerful capability of quantum error mitigation scheme for the general quantum simulation.

## 7.2 Simulation of two fermionic modes

The Hamiltonian of Hubbard model with two modes is

$$H = \frac{J}{2} (\sigma_{1,x} \sigma_{2,x} + \sigma_{1,y} \sigma_{2,y}) + \frac{U}{4} (\sigma_{1,z} \sigma_{2,z} + \sigma_{1,z} + \sigma_{2,z}), \quad (7-8)$$

which can be easily realized with Trotter expansion in experiment. The Trotter step is shown in fig. 7.1. Note that the native two-qubit entangling gate in our trapped ion system

is  $U(\theta) = \exp[-i\theta\sigma_y\sigma_y]$ , we can realize the two-qubit gates on the  $\sigma_x$  and  $\sigma_z$  basis by adding single-qubit rotations.

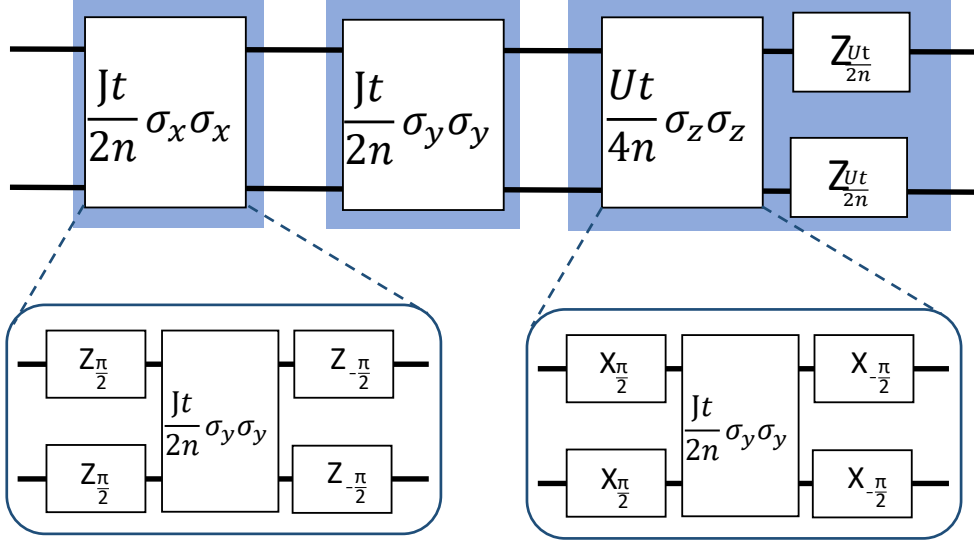


Figure 7.1 The Trotter step of two fermionic modes.

We numerically simulate the Fermi-Hubbard model dynamics with two modes in the digital way and find the Trotter expansion error can be ignored due to the commutation relations among each step. We set the hopping strength  $J = 1$ , the repulsion strength  $U = 2$ ,  $t = 2\pi$ , and Trotter step  $n = 4$ . Then the basic two-qubit gate in each step would be  $U(\frac{\pi}{4}) = \exp[-i\frac{\pi}{4}\sigma_y\sigma_y]$ , which is just the maximum entangling gate  $MS_{YY}$  we showed in chapter 6. In order to apply quantum error mitigation, the basic quantum gate in the circuit needs to be characterized first. Here, we can use the experimental circuits in chapter 6 for the characterization of the basic two-qubit gate in the Trotter circuit.

We first set the initial fermionic state as  $|10\rangle$  and simulate the ideal dynamics in the analog way. We can only observe the hopping evolution with this two-site condition. In order to simulate the gate error in experiment, we apply a 2% Pauli error on each two-qubit gate in the numerical calculation. Then, we apply the probabilistic error cancellation scheme to the noisy gates and get the error-mitigated dynamical evolution, as shown in fig. 7.2. The detailed process of applying error mitigation on the Trotter steps is similar (even easier) to apply it on the RB circuits in chapter 6 (Please check the detail in chapter 6 if necessary). We can see the error-mitigated data points are almost same as the predicted occupation of the modes from Trotter expansion.

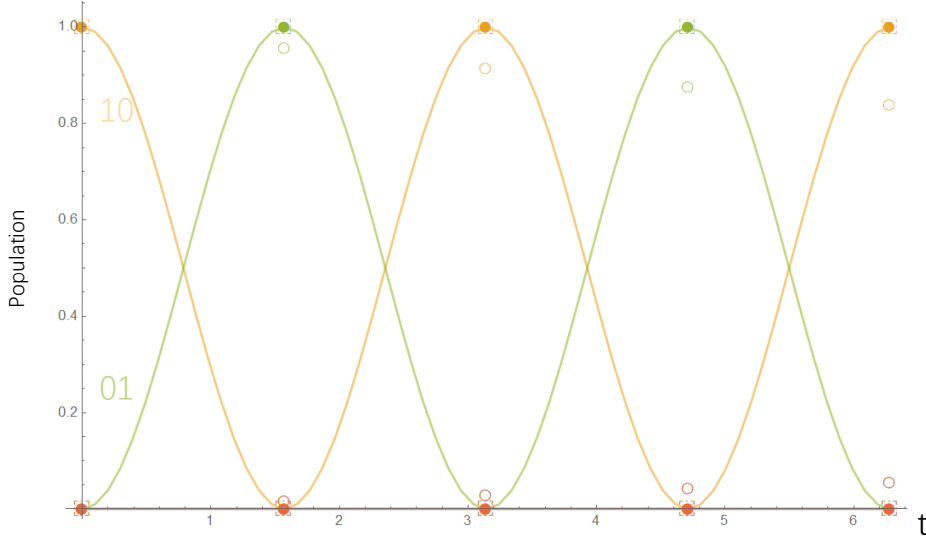


Figure 7.2 The dynamical evolution of fermionic Hubbard model with two modes. The solid line is the ideal evolution with analog simulation. The circle points are calculated with 2% Pauli error on each gate. The points with dotted square are the prediction of digital simulation with Trotter expansion. And the filled circle points are the simulating results with error mitigation.

### 7.3 Simulation of three fermionic modes

The Hamiltonian of Hubbard model with three modes is

$$H = \frac{J}{2}(\sigma_{1,x}\sigma_{2,x} + \sigma_{2,x}\sigma_{3,x} + \sigma_{1,y}\sigma_{2,y} + \sigma_{2,y}\sigma_{3,y}) + \frac{U}{4}(\sigma_{1,z}\sigma_{2,z} + \sigma_{2,z}\sigma_{3,z} + \sigma_{1,z} + 2\sigma_{2,z} + \sigma_{3,z}). \quad (7-9)$$

The Trotter step is shown in fig. 7.3. We also realize the two-qubit gates on the  $\sigma_x$  and  $\sigma_z$  basis by adding single-qubit rotations before and after the native entangling gate  $\exp[-i\theta\sigma_y\sigma_y]$ .

In chapter 5, we use a single global operation to generate a GHZ state with three and four qubits, where the coupling strength of all the two-body terms is  $\pi/4$ . Actually, we can achieve arbitrary coupling strength by determining the objective function with different constraint(see equation.( 5-7)), which provides us another implementation for the Trotter circuit through global entangling gates except for the combination of two-qubit gates.

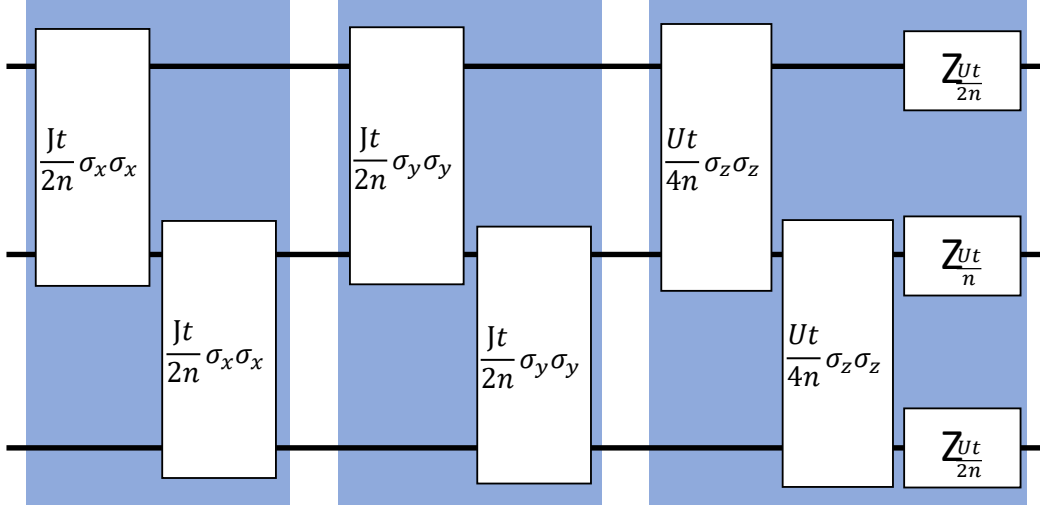


Figure 7.3 The Trotter step of three fermionic modes.

We numerically simulate the Fermi-Hubbard model dynamics with three modes in the digital way. We set the hopping strength  $J = 1$ , the repulsion strength  $U = 0$ , and  $t = \pi$ . In order to reduce the Trotter expansion error, we set the basic two-qubit gate in each step as  $U(\frac{\pi}{8}) = \exp[-i\frac{\pi}{8}\sigma_y\sigma_y]$  and Trotter step  $n = 4$ . Here, in order to apply quantum error mitigation, the basic quantum gate in the circuit can be chosen with two ways: the two-qubit gates  $\exp[-i\frac{\pi}{8}\sigma_{1,y}\sigma_{2,y}]$  and  $\exp[-i\frac{\pi}{8}\sigma_{2,y}\sigma_{3,y}]$  or the global entangling gate  $\exp[-i\frac{\pi}{8}(\sigma_{1,y}\sigma_{2,y} + \sigma_{2,y}\sigma_{3,y})]$ .

For the gate set tomography of two(three)-qubit gates, we can also apply a two-step parameter estimation, since the infidelities for the single-qubit gates are about an order lower than those of the two(three)-qubit gates. We first determine the Pauli error rates for all the single-qubit gates, and then characterize the two(three)-qubit gate  $\exp[-i\frac{\pi}{8}\sigma_{i,y}\sigma_{i+1,y}](\exp[-i\frac{\pi}{8}(\sigma_{1,y}\sigma_{2,y} + \sigma_{2,y}\sigma_{3,y})])$  based on the knowledge of the characterized single-qubit gates. The two(three)-qubit gates on  $\sigma_x$  and  $\sigma_z$  basis can be derived from those results.

For the first approach, we need to characterize 2 two-qubit gates and obtain two PTMs with dimension  $16 \times 16$ , which is similar with the case we discussed in chapter 6. It is easy to calculate the experimental circuits for two-qubit GST and the total measurements is  $15+15=30$ . For the second approach, we need to characterize the three-qubit gate and obtain the PTM with dimension  $64 \times 64$ , as shown in fig. 7.4. It takes a little bit more time to get the experimental setting for GST, and the total measurement would be 63 in

principle. We may compare the two approaches in experiment later.

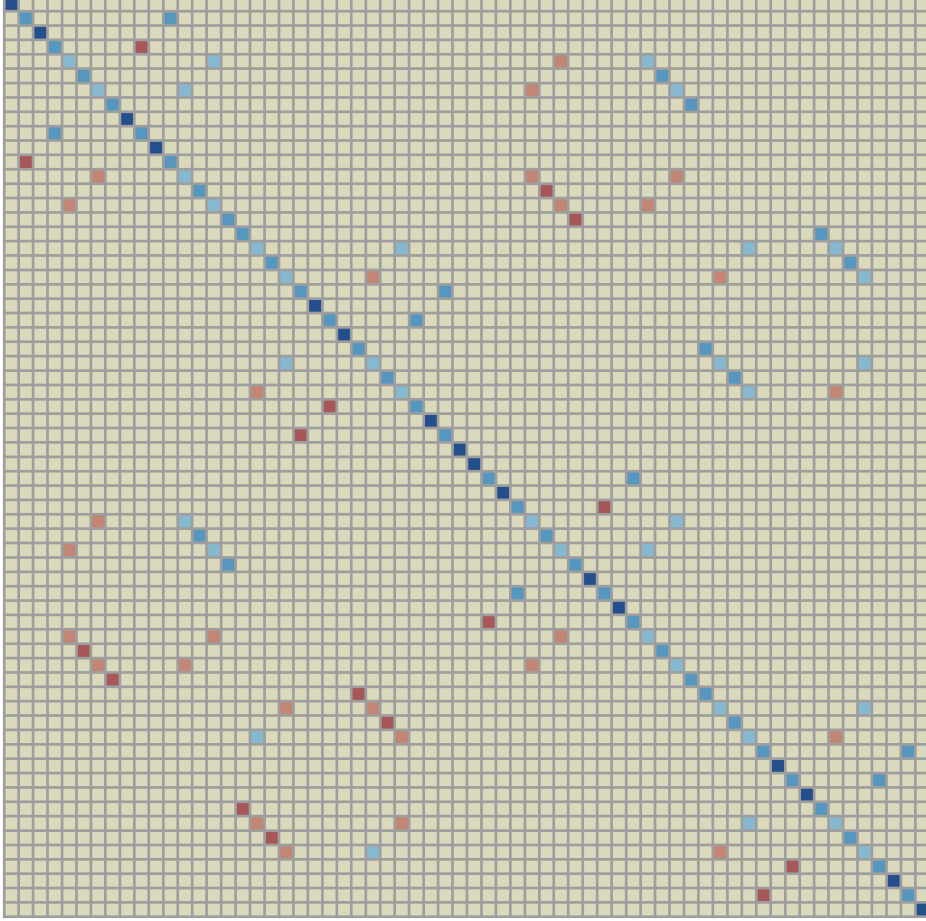


Figure 7.4 The PTM of three-qubit gate  $\exp[-i\frac{\pi}{8}(\sigma_{1,y}\sigma_{2,y} + \sigma_{2,y}\sigma_{3,y})]$ .

We first set the initial fermionic state as  $(|101\rangle + |110\rangle)/\sqrt{2}$  and simulate the ideal dynamics in the analog way. In order to simulate the gate error in experiment, we also apply a 2% Pauli error on each two-qubit gate in the numerical calculation. Then, we apply the probabilistic error cancellation scheme to the noisy gates and get the error-mitigated dynamical evolution, as shown in fig. 7.5. We can see the error-mitigated data points are almost same as the predicted occupation of the modes from Trotter expansion.



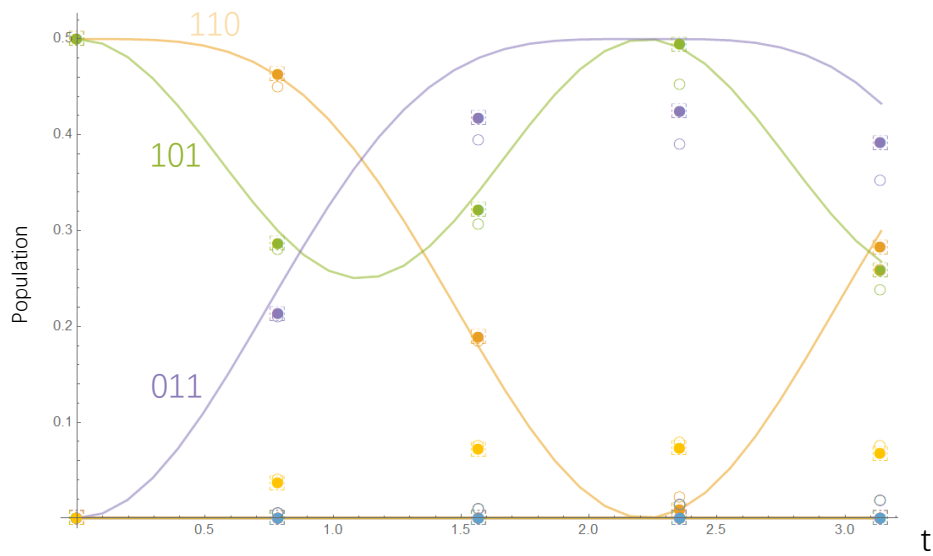


Figure 7.5 The dynamical evolution of fermionic Hubbard model with three modes. The solid line is the ideal evolution with analog simulation. The circle points are calculated with 2% Pauli error on each gate. The points with dotted square are the prediction of digital simulation with Trotter expansion. And the filled circle points are the simulating results with error mitigation.

## Chapter 8 Conclusion and Outlook

### Summary

In this thesis, we demonstrate the development of trapped ion system for quantum computation. Our trap is composed of four segmented blade RF trap with the capability of individual control on ion-qubits. To test the capability and stability of our general quantum simulator, we propose and implement a scalable scheme to realize the global entangling gates on multiple  $^{171}\text{Yb}^+$  ion qubits by coupling the laser field to multiple motional modes. The global gate fidelity is limited by the system imperfection. I analyze the system error-model and implement the probabilistic error-cancellation method to improve the estimation of expectation value, and investigate its universal validity in a general quantum computational context. Still, we have a long way to realize a fully functional quantum system. The following researches may be the next step to get close to our final goal from my perspective.

### Crosstalk-suppressed gate

The crosstalk-error, including quantum detection crosstalk and individual laser-addressed crosstalk, is always a significant contribution to the infidelity of quantum gates. The error from detection crosstalk can be removed in the classical programming level by detection error correction with characterization in advance<sup>[96]</sup>. It needs conditions of very small time-dependent systematic drifting or frequent characterization, which has been realized in our system. The other way is the fiber array solution together with a series of single-channel PMTs in the physical level. The fiber array can individually collect the fluorescence from each ion. And the separated single-channel PMTs can perfectly avoid the crosstalk from detection devices.

The error from laser-addressed crosstalk is difficult to be fully removed due to the small separation between neighboring ions and the inevitable imaging aberrations of laser beams, which the probabilistic error cancellation scheme cannot deal with in the programming level. We noticed that the crosstalk-error from two-qubit entangling gates is not significant due to the off-resonant motional coupling from the differential AC stark shift in the neighboring ions. There are two theoretical methods to suppress the crosstalk-

error from single-qubit gates: the composite sequences<sup>[99]</sup> and the spatial refocusing technique<sup>[100]</sup>. The first method works well for localized beams to produce narrowband sequences of improving total pulse area. The latter can be applied on broad beams to reconstruct a focused beam by spectrally decomposing the desired amplitude profile. This inspires us to implement them in experiment to achieve quantum gates with higher fidelity.

## Cryogenic trapped-ion system

The long lifetime of multi-ion qubits is the essential part to realize scalable quantum computers and quantum networks with trapped ion system. The instability of ions may come from the imperfect trapping potential in theoretical level, the RF noise on the DC electrodes from the RF field leakage in experiment and the molecular collision in the vacuum. The first part can be improved by increasing the frequency of the RF field to reach a smaller  $q$  factor<sup>[29]</sup>. The second part can be suppressed by adding a filter system on the DC blade electrodes. The last part can be reduced by improving the vacuum level, which has been explored a lot recently.

The current vacuum level in trapped ion systems is UHV, which is almost the pumping limit at the room temperature for now. Cryogenic trapped-ion systems may be an ideal choice for stably trapping tens to hundreds of ions in the next stage<sup>[103]</sup>. The segmented blade ion-trap is enclosed in a 4K cryostat, where all the molecules are liquefied to improve the vacuum level to extremely high vacuum(XHV). Therefore, the ion chain can be protected from the background collision to survive for several hours. This technique may help to implement complex quantum circuits and realize a stable and practicable quantum network and quantum cloud in the future.

## List of Figures

Figure 2.1	The general four-rod trap design and the electrodes connection .....	7
Figure 2.2	The blade trap design and the electrodes connection .....	8
Figure 2.3	The assembled blade trap picture .....	8
Figure 2.4	Ions figure .....	9
Figure 2.5	The stabilization of the RF power .....	10
Figure 2.6	Energy structure of $^{171}\text{Yb}^+$ .....	11
Figure 2.7	Optical system setup .....	12
Figure 2.8	Doppler cooling scheme .....	13
Figure 2.9	Detection scheme.....	14
Figure 3.1	The three resonances with Raman laser .....	18
Figure 3.2	The motional trajectory in phase space .....	19
Figure 3.3	Schematic diagram for parameterized time evolution. ....	21
Figure 3.4	The cyclic evolution in the projective and normal Hilbert space. ....	22
Figure 3.5	The trajectories of the four basis states in phase space. ....	24
Figure 3.6	Optical pumping scheme. ....	25
Figure 3.7	Sideband cooling scheme. ....	26
Figure 4.1	Blade trap system design. ....	28
Figure 4.2	The five-segment blade picture. ....	29
Figure 4.3	The attached capacitor picture. ....	30
Figure 4.4	The assembled trap picture. ....	31
Figure 4.5	The symmetry quality through microscope. ....	32
Figure 4.6	The 3D structure of blade trap through microscope. ....	32
Figure 4.7	The blade trap picture with vacuum system.....	33

List of Figures

---

Figure 4.8 The coupling efficiency vs time during curing. ....	36
Figure 4.9 High power test result. ....	37
Figure 4.10 The optical path for testing the EOD quality.....	38
Figure 4.11 The fake beam shape "tail" with beam profiler device. ....	39
Figure 4.12 The offset on the beam profiler vs the driven voltage on the EOD. ....	40
Figure 4.13 The optical path for testing the EOD responding speed. ....	41
Figure 4.14 The EOD responding speed testing figure with oscilloscope. ....	41
Figure 4.15 The schematic individual beam setup. ....	42
Figure 4.16 Setup for testing DOE.....	43
Figure 4.17 The measured image picture of five beams. ....	44
Figure 4.18 The setup to measure the intensity distribution of DOE output. ....	44
Figure 4.19 The intensity distribution through pin-hole measurement.....	45
Figure 4.20 The energy distribution histogram.....	45
Figure 4.21 The individual beams imaging on the EMCCD. ....	46
Figure 5.1 The experiment setup.....	49
Figure 5.2 The effective Raman laser detuning for single-mode approach. ....	49
Figure 5.3 The time evolution of three-qubit entangling gate and the parity oscillation.	51
Figure 5.4 The time evolution of two-qubit entangling gate and the parity oscillation within three-ion chain .....	52
Figure 5.5 The parity oscillation of two qubit entanglement.....	53
Figure 5.6 Experimental implementation of a global three-qubit entangling gate.....	55
Figure 5.7 The GHZ state of the global entangling gates in three-ion chain. ....	56
Figure 5.8 Experimental implementation of a global three-qubit entangling gate.....	57
Figure 5.9 The trajectory of motional modes.....	58
Figure 5.10 The GHZ state of the global entanglement-gates in four-ion chain.....	59

Figure 5.11 Comparison between gate durations of single- and multi-mode approaches. ....	60
Figure 6.1 Paradigm of error-mitigated quantum computation .....	62
Figure 6.2 Gram matrix .....	65
Figure 6.3 PTMs of single-qubit gates for the single-qubit case .....	67
Figure 6.4 Experimental circuits for the characterization of the $MS_{YY}$ gate .....	68
Figure 6.5 The realization of $MS_{ZZ}$ gate .....	69
Figure 6.6 Pauli transfer matrices of the experimental gates $MS_{YY}$ and $MS_{ZZ}$ in the two-qubit case .....	70
Figure 6.7 Verification of the Pauli-error assumption .....	71
Figure 6.8 Quasi-probability decomposition for single-qubit case .....	72
Figure 6.9 Quasi-probability decomposition for two-qubit case .....	72
Figure 6.10 The single-qubit randomized benchmarking .....	75
Figure 6.11 The two-qubit random-circuit computation.....	76
Figure 6.12 Analysis of the qubit crosstalk effect .....	78
Figure 7.1 The Trotter step of two fermionic modes.....	82
Figure 7.2 The dynamical evolution of fermionic Hubbard model with two modes ...	83
Figure 7.3 The Trotter step of three fermionic modes. ....	84
Figure 7.4 The PTM of three-qubit gate $\exp[-i\frac{\pi}{8}(\sigma_{1,y}\sigma_{2,y} + \sigma_{2,y}\sigma_{3,y})]$ . ....	85
Figure 7.5 The dynamical evolution of fermionic Hubbard model with three modes .	86

## List of Equations

Equation 2-1 .....	5
Equation 2-2 .....	5
Equation 2-3 .....	5
Equation 2-4 .....	6
Equation 3-1 .....	15
Equation 3-2 .....	15
Equation 3-3 .....	15
Equation 3-4 .....	16
Equation 3-5 .....	16
Equation 3-6 .....	16
Equation 3-7 .....	16
Equation 3-8 .....	17
Equation 3-9 .....	17
Equation 3-10 .....	17
Equation 3-11 .....	18
Equation 3-12 .....	18
Equation 3-13 .....	19
Equation 3-14 .....	20
Equation 3-15 .....	20
Equation 3-16 .....	20
Equation 3-17 .....	20
Equation 3-18 .....	20
Equation 3-19 .....	21

List of Equations

---

Equation 3-20 .....	21
Equation 3-21 .....	22
Equation 3-22 .....	22
Equation 3-23 .....	22
Equation 3-24 .....	22
Equation 3-25 .....	22
Equation 3-26 .....	23
Equation 3-27 .....	23
Equation 3-28 .....	23
Equation 3-29 .....	24
Equation 3-30 .....	24
Equation 5-1 .....	48
Equation 5-2 .....	48
Equation 5-3 .....	53
Equation 5-4 .....	53
Equation 5-5 .....	53
Equation 5-6 .....	53
Equation 5-7 .....	54
Equation 6-1 .....	66
Equation 6-2 .....	74
Equation 6-3 .....	74
Equation 6-4 .....	75
Equation 7-1 .....	80
Equation 7-2 .....	80
Equation 7-3 .....	80
Equation 7-4 .....	80



List of Equations

---

Equation 7-5 .....	81
Equation 7-6 .....	81
Equation 7-7 .....	81
Equation 7-8 .....	81
Equation 7-9 .....	83

---

## Bibliography

- [1] Feynman R P. Simulating physics with computers [J/OL]. *International Journal of Theoretical Physics*, 1982, 21(6):467-488. <https://doi.org/10.1007/BF02650179>.
- [2] Preskill J. Quantum computing in the nisq era and beyond. *Quantum*, 2018, 2:79.
- [3] McClean J R, Romero J, Babbush R, et al. The theory of variational hybrid quantum-classical algorithms. *New J. Phys.*, 2016, 18(2):023023.
- [4] Peruzzo A, McClean J, Shadbolt P, et al. A variational eigenvalue solver on a photonic quantum processor. *Nat. Commun.*, 2014, 5:4213.
- [5] Shen Y, Zhang X, Zhang S, et al. Quantum implementation of the unitary coupled cluster for simulating molecular electronic structure. *Phys. Rev. A*, 2017, 95(2):020501.
- [6] Kandala A, Mezzacapo A, Temme K, et al. Hardware-efficient variational quantum eigensolver for small molecules and quantum magnets. *Nature*, 2017, 549(7671):242.
- [7] Bauer B, Wecker D, Millis A J, et al. Hybrid quantum-classical approach to correlated materials [J/OL]. *Phys. Rev. X*, 2016, 6:031045. <https://link.aps.org/doi/10.1103/PhysRevX.6.031045>.
- [8] Kokail C, Maier C, van Bijnen R, et al. Self-verifying variational quantum simulation of the lattice schwinger model. *arXiv:1810.03421*, 2018.
- [9] Farhi E, Goldstone J, Gutmann S. A quantum approximate optimization algorithm. *arXiv preprint arXiv:1411.4028*, 2014.
- [10] Wecker D, Bauer B, Clark B K, et al. Gate-count estimates for performing quantum chemistry on small quantum computers. *Physical Review A*, 2014, 90(2):022305.
- [11] Reiher M, Wiebe N, Svore K M, et al. Elucidating reaction mechanisms on quantum computers. *Proc. Natl. Acad. Sci.*, 2017, 114(29):7555-7560.
- [12] McArdle S, Endo S, Aspuru-Guzik A, et al. Quantum computational chemistry. *arXiv:1808.10402v2*, 2019.
- [13] Shor P W. Scheme for reducing decoherence in quantum computer memory [J/OL]. *Phys. Rev. A*, 1995, 52:R2493-R2496. <https://link.aps.org/doi/10.1103/PhysRevA.52.R2493>.
- [14] Steane A M. Error correcting codes in quantum theory [J/OL]. *Phys. Rev. Lett.*, 1996, 77: 793-797. <https://link.aps.org/doi/10.1103/PhysRevLett.77.793>.
- [15] O’Gorman J, Campbell E T. Quantum computation with realistic magic-state factories. *Phys. Rev. A*, 2017, 95(3):032338.
- [16] Li Y, Benjamin S C. Efficient variational quantum simulator incorporating active error minimization [J/OL]. *Phys. Rev. X*, 2017, 7:021050. <https://link.aps.org/doi/10.1103/PhysRevX.7.021050>.
- [17] Temme K, Bravyi S, Gambetta J M. Error mitigation for short-depth quantum circuits [J/OL]. *Phys. Rev. Lett.*, 2017, 119:180509. <https://link.aps.org/doi/10.1103/PhysRevLett.119.180509>.
- [18] Endo S, Benjamin S C, Li Y. Practical quantum error mitigation for near-future applications [J/OL]. *Phys. Rev. X*, 2018, 8:031027. <https://link.aps.org/doi/10.1103/PhysRevX.8.031027>.

## Bibliography

---

- [19] Havlíček V, Córcoles A D, Temme K, et al. Supervised learning with quantum-enhanced feature spaces. *Nature*, 2019, 567(7747):209.
- [20] Kandala A, Temme K, Córcoles A D, et al. Error mitigation extends the computational reach of a noisy quantum processor. *Nature*, 2019, 567(7749):491.
- [21] Song C, Cui J, Wang H, et al. Quantum computation with universal error mitigation on superconducting quantum processor. *arXiv preprint arXiv:1812.10903*, 2018.
- [22] Wang Y, Um M, Zhang J, et al. Single-qubit quantum memory exceeding ten-minute coherence time. *Nature Photonics*, 2017, 11(10):646-650.
- [23] Ballance C J, Harty T P, Linke N M, et al. High-fidelity quantum logic gates using trapped-ion hyperfine qubits [J/OL]. *Phys. Rev. Lett.*, 2016, 117:060504. <https://link.aps.org/doi/10.1103/PhysRevLett.117.060504>.
- [24] Monz T, Schindler P, Barreiro J T, et al. 14-qubit entanglement: creation and coherence. *Phys. Rev. Lett.*, 2011, 106(13):130506.
- [25] Knill E, Leibfried D, Reichle R, et al. Randomized benchmarking of quantum gates [J/OL]. *Phys. Rev. A*, 2008, 77:012307. <https://link.aps.org/doi/10.1103/PhysRevA.77.012307>.
- [26] Griffiths B W G E. Introduction[m]/monetary targets. Springer., 1981, 1(12).
- [27] Paul W. Electromagnetic traps for charged and neutral particles [J/OL]. *Rev. Mod. Phys.*, 1990, 62:531-540. <https://link.aps.org/doi/10.1103/RevModPhys.62.531>.
- [28] Dehmelt H G. Radiofrequency Spectroscopy of Stored Ions I: Storage. *Advances in Atomic and Molecular Physics*, 1968, 3:53-72.
- [29] Leibfried D, Blatt R, Monroe C, et al. Quantum dynamics of single trapped ions [J/OL]. *Rev. Mod. Phys.*, 2003, 75:281-324. <https://link.aps.org/doi/10.1103/RevModPhys.75.281>.
- [30] Monroe C. Quantum information processing with atoms and photons [J/OL]. *Nature*, 2002, 416(6877):238-246. <https://doi.org/10.1038/416238a>.
- [31] Siverns J D, Simkins L R, Weidt S, et al. On the application of radio frequency voltages to ion traps via helical resonators [J/OL]. *Applied Physics B*, 2012, 107(4):921-934. <https://doi.org/10.1007/s00340-011-4837-0>.
- [32] Kim K, Chang M S, Korenblit S, et al. Quantum simulation of frustrated ising spins with trapped ions [J/OL]. *Nature*, 2010, 465(7298):590-593. <https://doi.org/10.1038/nature09071>.
- [33] Islam R, Senko C, Campbell W C, et al. Emergence and frustration of magnetism with variable-range interactions in a quantum simulator [J/OL]. *Science*, 2013, 340(6132):583. <http://science.sciencemag.org/content/340/6132/583.abstract>.
- [34] Richerme P, Gong Z X, Lee A, et al. Non-local propagation of correlations in quantum systems with long-range interactions [J/OL]. *Nature*, 2014, 511(7508):198-201. <https://doi.org/10.1038/nature13450>.
- [35] Senko C, Smith J, Richerme P, et al. Coherent imaging spectroscopy of a quantum many-body spin system. *Science (New York, N.Y.)*, 2014, 345.
- [36] Debnath S, Linke N M, Figgatt C, et al. Demonstration of a small programmable quantum computer with atomic qubits [J/OL]. *Nature*, 2016, 536(7614):63-6. <https://www.ncbi.nlm.nih.gov/pubmed/27488798>.

- [37] Olmschenk S, Younge K C, Moehring D L, et al. Manipulation and detection of a trapped  $\text{yb}^+$  hyperfine qubit [J/OL]. *Phys. Rev. A*, 2007, 76:052314. <https://link.aps.org/doi/10.1103/PhysRevA.76.052314>.
- [38] Balzer C, Braun A, Hannemann T, et al. Electrostatically trapped  $\text{yb}^+$  ions for quantum information processing [J/OL]. *Phys. Rev. A*, 2006, 73:041407. <https://link.aps.org/doi/10.1103/PhysRevA.73.041407>.
- [39] Olmschenk S, Matsukevich D N, Maunz P, et al. Quantum teleportation between distant matter qubits [J/OL]. *Science*, 2009, 323(5913):486. <http://science.sciencemag.org/content/323/5913/486.abstract>.
- [40] Hansch T W, Schawlow A L. Cooling of gases by laser radiation. *Optics Communications*, 1975, 13(1):68-69.
- [41] Huntemann N, Okhapkin M, Lipphardt B, et al. High-accuracy optical clock based on the octupole transition in  $^{171}\text{Yb}^+$  [J/OL]. *Phys. Rev. Lett.*, 2012, 108:090801. <https://link.aps.org/doi/10.1103/PhysRevLett.108.090801>.
- [42] Nagourney W, Sandberg J, Dehmelt H. Shelved optical electron amplifier: Observation of quantum jumps [J/OL]. *Phys. Rev. Lett.*, 1986, 56:2797-2799. <https://link.aps.org/doi/10.1103/PhysRevLett.56.2797>.
- [43] Noek R, Vrijsen G, Gaultney D, et al. High speed, high fidelity detection of an atomic hyperfine qubit. *Optics letters*, 2013, 38:4735-8.
- [44] Wong-Campos J D, Johnson K G, Neyenhuis B, et al. High-resolution adaptive imaging of a single atom [J/OL]. *Nature Photonics*, 2016, 10(9):606-610. <https://doi.org/10.1038/nphoton.2016.136>.
- [45] Haljan P C, Brickman K A, Deslauriers L, et al. Spin-dependent forces on trapped ions for phase-stable quantum gates and entangled states of spin and motion [J/OL]. *Phys. Rev. Lett.*, 2005, 94:153602. <https://link.aps.org/doi/10.1103/PhysRevLett.94.153602>.
- [46] Lee P J, Brickman K A, Deslauriers L, et al. Phase control of trapped ion quantum gates [J/OL]. *Journal of Optics B: Quantum and Semiclassical Optics*, 2005, 7(10):S371-S383. <http://dx.doi.org/10.1088/1464-4266/7/10/025>.
- [47] Cirac J I, Zoller P. Quantum computations with cold trapped ions [J/OL]. *Phys. Rev. Lett.*, 1995, 74:4091-4094. <https://link.aps.org/doi/10.1103/PhysRevLett.74.4091>.
- [48] Schmidt-Kaler F, Häffner H, Riebe M, et al. Realization of the cirac - zoller controlled-not quantum gate [J/OL]. *Nature*, 2003, 422(6930):408-411. <https://doi.org/10.1038/nature01494>.
- [49] Sørensen A, Mølmer K. Quantum computation with ions in thermal motion [J/OL]. *Phys. Rev. Lett.*, 1999, 82:1971-1974. <https://link.aps.org/doi/10.1103/PhysRevLett.82.1971>.
- [50] Durstberger K. Geometric phases in quantum theory. UNIVERSITÄT WIEN, 2002.
- [51] Berry M V. Quantal phase factors accompanying adiabatic changes. *Proc. R. Soc. Lond*, 1984, A(392):45-57.
- [52] Aharonov Y, Anandan J. Phase change during a cyclic quantum evolution [J/OL]. *Phys. Rev. Lett.*, 1987, 58:1593-1596. <https://link.aps.org/doi/10.1103/PhysRevLett.58.1593>.
- [53] Haljan P C, Lee P J, Brickman K A, et al. Entanglement of trapped-ion clock states [J/OL]. *Phys. Rev. A*, 2005, 72:062316. <https://link.aps.org/doi/10.1103/PhysRevA.72.062316>.

## Bibliography

---

- [54] Colombe Y, Slichter D H, Wilson A C, et al. Single-mode optical fiber for high-power, low-loss uv transmission [J/OL]. *Optics Express*, 2014, 22(16):19783-19793. <http://www.opticsexpress.org/abstract.cfm?URI=oe-22-16-19783>.
- [55] Karlitschek P, Hillrichs G, Klein K F. Influence of hydrogen on the colour center formation in optical fibers induced by pulsed uv-laser radiation. part 1: all silica fibers with high-oh undoped core [J/OL]. *Optics Communications*, 1998, 155(4):376-385. <http://www.sciencedirect.com/science/article/pii/S003040189800409X>.
- [56] Marciniak C, Ball H, Hung A, et al. Towards fully commercial, uv-compatible fiber patch cords. *Optics Express*, 2017, 25.
- [57] Shor P W. Polynomial-time algorithms for prime factorization and discrete logarithms on a quantum computer. *SIAM J. Comput.*, 1997, 26(5):1484-1509.
- [58] Peruzzo A, McClean J, Shadbolt P, et al. A variational eigenvalue solver on a photonic quantum processor. *Nat. Commun.*, 2014, 5(4213):4213-4213.
- [59] Monz T, Nigg D, Martinez E A, et al. Realization of a scalable shor algorithm. *Science*, 2016, 351(6277):1068-1070.
- [60] Lloyd S. Universal quantum simulators. *Science*, 1996, 273(5278):1073-1078.
- [61] Blatt R, Roos C F. Quantum simulations with trapped ions. *Nat. Phys.*, 2012, 8(4):277-284.
- [62] Nielsen M A, Chuang I L. *Quantum computation and quantum information: 10th anniversary edition*. Cambridge University Press, 2010.
- [63] Ivanov S S, Ivanov P A, Vitanov N V. Efficient construction of three- and four-qubit quantum gates by global entangling gates [J/OL]. *Phys. Rev. A*, 2015, 91:032311. <https://link.aps.org/doi/10.1103/PhysRevA.91.032311>.
- [64] Martinez E A, Monz T, Nigg D, et al. Compiling quantum algorithms for architectures with multi-qubit gates. *New J. Phys.*, 2016, 18(6):063029.
- [65] Maslov D, Nam Y. Use of global interactions in efficient quantum circuit constructions. *New J. Phys.*, 2018, 20(3):033018.
- [66] Casanova J, Mezzacapo A, Lamata L, et al. Quantum simulation of interacting fermion lattice models in trapped ions [J/OL]. *Phys. Rev. Lett.*, 2012, 108:190502. <https://link.aps.org/doi/10.1103/PhysRevLett.108.190502>.
- [67] Yung M H, Casanova J, Mezzacapo A, et al. From transistor to trapped-ion computers for quantum chemistry. *Sci. Rep.*, 2015, 4(1):3589.
- [68] García-Álvarez L, Egusquiza I n L, Lamata L, et al. Digital quantum simulation of minimal ads/cft. *Phys. Rev. Lett.*, 2017, 119(4):040501.
- [69] Hempel C, Maier C, Romero J, et al. Quantum chemistry calculations on a trapped-ion quantum simulator. *Phys. Rev. X*, 2018, 8:031022.
- [70] Mølmer K, Sørensen A. Multiparticle entanglement of hot trapped ions. *Phys. Rev. Lett.*, 1999, 82(9):1835-1838.
- [71] Sørensen A, Mølmer K. Quantum computation with ions in thermal motion. *Phys. Rev. Lett.*, 1999, 82(9):1971.
- [72] Solano E, de Matos Filho R L, Zagury N. Deterministic bell states and measurement of the motional state of two trapped ions. *Phys. Rev. A*, 1999, 59(4):029903.

## Bibliography

---

- [73] Kim K, Chang M S, Islam R, et al. Entanglement and tunable spin-spin couplings between trapped ions using multiple transverse modes. *Phys. Rev. Lett.*, 2009, 103(12):120502.
- [74] Korenblit S, Kafri D, Campbell W C, et al. Quantum simulation of spin models on an arbitrary lattice with trapped ions. *New J. Phys.*, 2012, 14(9):095024-095024.
- [75] Linke N M, Maslov D, Roetteler M, et al. Experimental comparison of two quantum computing architectures. *Proc. Natl. Acad. Sci. U. S. A.*, 2017, 114(13):3305-3310.
- [76] Lanyon B P, Hempel C, Nigg D, et al. Universal digital quantum simulation with trapped ions. *Science*, 2011, 334(6052):57-61.
- [77] Barreiro J T, Müller M, Schindler P, et al. An open-system quantum simulator with trapped ions. *Nature*, 2011, 470(7335):486-491.
- [78] Zhu S L, Monroe C, Duan L M. Arbitrary-speed quantum gates within large ion crystals through minimum control of laser beams. *Europhys. Lett.*, 2006, 73(4):485-491.
- [79] Zhu S L, Monroe C, Duan L M. Trapped ion quantum computation with transverse phonon modes. *Phys. Rev. Lett.*, 2006, 97(5):050505.
- [80] Steane A M, Imreh G, Home J P, et al. Pulsed force sequences for fast phase-insensitive quantum gates in trapped ions. *New J. Phys.*, 2014, 16(5):053049.
- [81] Green T J, Biercuk M J. Phase-modulated decoupling and error suppression in qubit-oscillator systems. *Phys. Rev. Lett.*, 2014, 114(12):120502.
- [82] Leung P H, Landsman K A, Figgatt C, et al. Robust 2-qubit gates in a linear ion crystal using a frequency-modulated driving force. *Phys. Rev. Lett.*, 2018, 120(2):020501.
- [83] Choi T, Debnath S, Manning A T, et al. Optimal quantum control of multimode couplings between trapped ion qubits for scalable entanglement. *Phys. Rev. Lett.*, 2014, 112(19):190502.
- [84] Milne A R, Edmunds C L, Hempel C, et al. Phase-modulated entangling gates robust against static and time-varying errors [J/OL]. *arXiv:1808.10462*, 2018. [arxiv.org/abs/1808.10462](https://arxiv.org/abs/1808.10462).
- [85] Kaufmann H, Ruster T, Schmiegelow C T, et al. Scalable creation of long-lived multipartite entanglement. *Phys. Rev. Lett.*, 2017, 119(15):150503.
- [86] Webb A E, Webster S C, Collingbourne S, et al. Resilient entangling gates for trapped ions [J/OL]. *Phys. Rev. Lett.*, 2018, 121:180501. <https://link.aps.org/doi/10.1103/PhysRevLett.121.180501>.
- [87] Shapira Y, Shaniv R, Manovitz T, et al. Robust entanglement gates for trapped-ion qubits [J/OL]. *Phys. Rev. Lett.*, 2018, 121:180502. <https://link.aps.org/doi/10.1103/PhysRevLett.121.180502>.
- [88] Lu Y. Fully controllable quantum computing system based on trapped-ion platform. Ph.D thesis, 2020.
- [89] Sackett C A, Kielpinski D, King B E, et al. Experimental entanglement of four particles. *Nature*, 2000, 404(6775):256-259.
- [90] Merkel S T, Gambetta J M, Smolin J A, et al. Self-consistent quantum process tomography. *Phys. Rev. A*, 2013, 87(6):062119.
- [91] Blume-Kohout R, Gamble J K, Nielsen E, et al. Demonstration of qubit operations below a rigorous fault tolerance threshold with gate set tomography. *Nat. Commun.*, 2017, 8:14485.
- [92] Greenbaum D. Introduction to quantum gate set tomography. *arXiv preprint arXiv:1509.02921*, 2015.

## Bibliography

---

- [93] Schindler P. Frequency synthesis and pulse shaping for quantum information processing with trapped ions. Diploma thesis, Innsbruck University, 2008.
- [94] Tan T R, Gaebler J P, Lin Y, et al. Multi-element logic gates for trapped-ion qubits. *Nature*, 2015, 528(7582):380.
- [95] Olmschenk S, Younge K C, Moehring D L, et al. Manipulation and detection of a trapped  $\text{yb}^+$  hyperfine qubit [J/OL]. *Phys. Rev. A*, 2007, 76:052314. <https://link.aps.org/doi/10.1103/PhysRevA.76.052314>.
- [96] Shen C, Duan L M. Correcting detection errors in quantum state engineering through data processing. *New J. Phys.*, 2012, 14(5):053053.
- [97] Gaebler J P, Meier A M, Tan T R, et al. Randomized benchmarking of multiqubit gates [J/OL]. *Phys. Rev. Lett.*, 2012, 108:260503. <https://link.aps.org/doi/10.1103/PhysRevLett.108.260503>.
- [98] Mavadia S, Edmunds C, Hempel C, et al. Experimental quantum verification in the presence of temporally correlated noise. *npj Quantum Inf.*, 2018, 4(1):7.
- [99] Merrill J T, Doret S C, Vittorini G, et al. Transformed composite sequences for improved qubit addressing [J/OL]. *Phys. Rev. A*, 2014, 90:040301. <https://link.aps.org/doi/10.1103/PhysRevA.90.040301>.
- [100] Shen C, Gong Z X, Duan L M. Individual addressing in quantum computation through spatial refocusing [J/OL]. *Phys. Rev. A*, 2013, 88:052325. <https://link.aps.org/doi/10.1103/PhysRevA.88.052325>.
- [101] Jordens R, Strohmaier N, Gunter K, et al. A mott insulator of fermionic atoms in an optical lattice [J/OL]. *Nature*, 2008, 455(7210):204-7. <https://www.ncbi.nlm.nih.gov/pubmed/18784720><https://www.nature.com/articles/nature07244>.
- [102] Barends R, Lamata L, Kelly J, et al. Digital quantum simulation of fermionic models with a superconducting circuit [J/OL]. *Nature Communications*, 2015, 6(1):7654. <https://doi.org/10.1038/ncomms8654>.
- [103] Pagano G, Hess P W, Kaplan H B, et al. Cryogenic trapped-ion system for large scale quantum simulation [J/OL]. *Quantum Science and Technology*, 2018, 4(1):014004. <http://dx.doi.org/10.1088/2058-9565/aae0fe>.
- [104] 薛瑞尼. ThuThesis: 清华大学学位论文模板 [EB/OL]. 2017[2019-04-27]. <https://github.com/xueruini/thuthesis>.

## Acknowledgements

I would like to express my heartfelt thanks to my advisor Prof. kihwan Kim. His extensive professional knowledge and rigorous academic attitude have benefited me greatly in my Ph.D career, which not only helped me lay a solid theoretical research foundation, but also guided me to accumulate rich scientific research experience and cultivate good scientific research habits. The six-year experience will definitely benefit me for a life.

I want to sincerely thank my theoretical collaborators Jingning Zhang and Ying Li. Their solid theoretical foundation not only helped me successfully complete each experimental project, but also inspired my enthusiasm for scientific research and broadened my horizons.

Surely, I am also grateful to everyone in our group. It is an honor to study, work and progress together with them. I have benefited a lot from their valuable suggestions in scientific research, and the friendship with them will last a lifetime. Thanks to Yangchao Shen, Xiang Zhang, and Kuan Zhang. Their theoretical and experimental guidance has improved my ability to solve problems and software programming skills when I first join the group. Thanks to Shuoming An and Ye Wang for their patient guidance when I start to assemble trap. Thanks to Yao Lu for working with me to complete the construction of our experimental platform and to collaborate on multiple experiments. In addition, Dahyun Yum, Dingshun Lv and Junhua Zhang give me a lot of encouragement and help. I am also very happy to spend precious time with the fresh blood, Pengfei Wang, Wentao Chen, Mu Qiao, Chunyang Luan, Zhengyang Cai, and Jialiang Zhang.

I would also like to thank the undergraduates who have worked in our group, Guan-hao Huang, Naijun Jin, Tian Xie, and Botao Du for providing me a lot of help in life.

Finally, I want to thank my parents to raise me, educate me, support me, and give me all they can give. I will keep moving on with their love.

Thank L<sup>A</sup>T<sub>E</sub>X 和 ThuThesis<sup>[104]</sup> for helping me to finish my thesis.



## 声 明

本人郑重声明：所呈交的学位论文，是本人在导师指导下，独立进行研究工作所取得的成果。尽我所知，除文中已经注明引用的内容外，本学位论文的研究成果不包含任何他人享有著作权的内容。对本论文所涉及的研究工作做出贡献的其他个人和集体，均已在文中以明确方式标明。

签 名：\_\_\_\_\_ 日 期：\_\_\_\_\_

## Resume, Publications and Research Achievements

### 个人简历

1991年3月1日出生于河南省滑县。

2010年9月考入北京大学天文系天体物理专业，2014年7月本科毕业并获得理学学士学位和计算机软件（双）学位。

2014年9月免试进入清华大学交叉信息研究院直接攻读博士学位至今。

### 发表的学术论文

- [1] Shuaining Zhang, Yao Lu, Kuan Zhang, Wentao Chen, Ying Li, Jing-Ning Zhang, Kihwan Kim. "Error-mitigated quantum gates exceeding physical fidelities in a trapped-ion system". *Nature Commun.* 11,587(2020)..
- [2] Yao Lu, Shuaining Zhang (co-author), Kuan Zhang (co-author), Wentao Chen, Yangchao Shen, Jialiang Zhang, Jing-Ning Zhang, Kihwan Kim. "Global entangling gates on arbitrary ion qubits". *Nature* 572, 363-367(2019).
- [3] Xiang Zhang, Kuan Zhang, Yangchao Shen, Shuaining Zhang, Jingning Zhang, Man-Hong Yung, Jorge Casanova, Julen S. Pedernales, Lucas Lamata, Enrique Solano, Kihwan Kim. "Experimental quantum simulation of fermion-antifermion scattering via boson exchange in a trapped ion". *Nature Commun.* 9, 195 (2018).
- [4] Yangchao Shen, Yao Lu, Kuan Zhang, Junhua Zhang, Shuaining Zhang, Joon-suk Huh, Kihwan Kim. "Quantum optical emulation of molecular vibronic spectroscopy using a trapped-ion device". *Chemical Science* 9, 836 (2018).
- [5] Yangchao Shen, Xiang Zhang, Shuaining Zhang, Jing-Ning Zhang, Man-Hong Yung, and Kihwan Kim. "Quantum implementation of the unitary coupled cluster for simulating molecular electronic structure". *Phys. Rev. A* 95, 020501(R) (2017).
- [6] Jiyong Park, Yao Lu, Jaehak Lee, Yangchao Shen, Kuan Zhang, Shuaining Zhang, Muhammad Suhail Zubairy, Kihwan Kim, and Hyunchul Nha. "Revealing non-classicality beyond Gaussian states via a single marginal distribution". *Proc. Natl. Acad. Sci.* doi:10.1073/pnas.1617621114 (2017).